creative commons
COMMONS DEED

저작자표시-비영리-변경금지 2.0 대한민국

이용자는 아래의 조건을 따르는 경우에 한하여 자유롭게

- 이 저작물을 복제, 배포, 전송, 전시, 공연 및 방송할 수 있습니다.

다음과 같은 조건을 따라야 합니다:

저작자표시. 귀하는 원저작자를 표시하여야 합니다.

비영리. 귀하는 이 저작물을 영리 목적으로 이용할 수 없습니다.

변경금지. 귀하는 이 저작물을 개작, 변형 또는 가공할 수 없습니다.

- 귀하는, 이 저작물의 재이용이나 배포의 경우, 이 저작물에 적용된 이용허락조건을 명확하게 나타내어야 합니다.
- 저작권자로부터 별도의 허가를 받으면 이러한 조건들은 적용되지 않습니다.

저작권법에 따른 이용자의 권리는 위의 내용에 의하여 영향을 받지 않습니다.

이것은 이용허락규약(Legal Code)을 이해하기 쉽게 요약한 것입니다.

Disclaimer

dCollection

공 학 박 사 학 위 논 문

Characteristics of Carbon Nanotube Membrane for Water Treatment and Its Biofouling Properties

수처리용 탄소나노튜브 막의 성능 및 바이오파울링 특성 평가

2015년 2월

서울대학교 대학원

화학생물공학부

백 영 빈

Characteristics of Carbon Nanotube Membrane for Water Treatment and Its Biofouling Properties

by

Youngbin Baek

under the supervision of

Professor Jeyong Yoon, Ph. D.

A dissertation submitted in partial fulfillment of the requirements for the Degree of
Doctor of Philosophy

FEBURARY 2015

SCHOOL OF CHEMICAL AND BIOLOGICAL ENGINEERING
SEOUL NATIONAL UNIVERSITY

Characteristics of Carbon Nanotube Membrane for Water Treatment and Its Biofouling Property

수처리용 탄소나노튜브 막의 성능 및
바이오파울링 특성 평가

지도교수 윤 제 용

이 논문을 공학박사 학위논문으로 제출함

2014년 12월

서울대학교 대학원
공과대학 화학생물공학부
백 영 빈

백영빈의 공학박사 학위논문을 인준함

2015년 1월

위 원 장 이 정우 (인)

부 위 원 장 윤 제용 (인)

위 원 김 용 철 (인)

위 원 이 종 찬 (인)

위 원 김 승 환 (인)

Abstract

Carbon nanotube (CNT) membrane has been highlighted for water treatment as a future membrane to solve water shortage problem. Due to the fast transport of water molecules through CNTs and antimicrobial property of CNT, CNT membranes are expected to make a high performance membrane and biofouling-resistant membrane. Here we evaluated three types of CNT membranes such as open-ended vertically aligned (VA) CNT membrane, dense-array outer-wall CNT membrane and mixed (matrix) CNT membranes and compared to the commercial membranes in terms of their permeability, rejection property and biofouling tendency.

Firstly, the feasibility of an open-ended VA CNT membrane for water treatment was investigated. The open-ended VA CNT membrane appeared to have approximately three times higher (about 1,100 LMH/bar) water permeability than the commercial UF membrane. This higher permeability was peculiarly observed in water, the most hydrophilic solvent, while other solvents showed that the permeabilities decreased with higher viscosity. The rejection property of the open-ended VA CNT membrane was similar to the commercial UF membrane, which examined by the MWCO measurement. Additionally, the open-ended VA CNT membrane showed better biofouling

resistance with approximately 15% less permeate flux reduction and 2 log less bacterial attachment than the UF membrane.

Secondly, dense-array outer-wall CNT membrane for water treatment was investigated as a novel UF membrane. It was exploited the characteristics and corresponding attributes in devising an UF membrane millimeter thick that can deliver a water permeability of close to 30,000 liters per square meter per hour (LMH) at 1 bar, which compares with the best water permeability of CNT membranes reported at 2,400 LMH/bar. The membrane consists only of vertically aligned CNT walls that provide 6 nm wide inner pores of CNTs, and also 7 nm wide outer pores that form between CNT walls when CNTs are densified. Experimental results obtained in the process of fabricating the dense-array outer-wall CNT membrane reveal that the water permeability increases as the CNTs are more densified or the pore size is decreased. It is also discovered that the dense-array outer-wall CNT membrane impedes bacteria adhesion and resist biofilm formation.

Finally, two types of mixed CNT RO membranes were investigated. PA-CNT-PVA membrane was fabricated by interfacial polymerization followed by the deposition of oxidized CNTs and the coating of PVA on the surface. It showed much improved mechanical properties and durability compared with the polyamide membrane without CNTs (PA membrane). The PA–CNT–PVA

membrane also exhibited better antifouling properties than the PA membrane and the commercial RO membrane. CNT embedded RO membrane, previously known to have ~30% higher flux than polyamide RO membrane, was fabricated by interfacial polymerization with CNTs in MPD solution and evaluated in terms of energy efficiency and fouling tendency compared to the polyamide RO membrane. CNT embedded RO membrane showed better energy efficiency than polyamide RO membrane because of the favorable surface properties and mechanical properties. It also showed less fouling potential for 138 h of artificial sea salt test and better flux recovery for the cleaning process. The results of three CNT membrane's performance indicate that CNT membranes can be applicable for high performance membrane and fouling-resistant membrane.

Keywords: Carbon nanotube membrane; water permeability; rejection property; biofouling; water treatment

Student number: 2009-20996

Tables of Contents

List of Figures

List of Tables

1. Introduction

1.1. Research Backgrounds

Water scarcity has emerged as one of the most serious global challenges which threatens over one-third of the world's population [1]. Membrane technology used for water treatment has been consistently developed to alleviate the water scarcity problem [2]. However, this membrane technology has some drawbacks such as high energy consumption and membrane fouling [3]. Although energy consumption has been decreased over the past decade, the membrane based water treatment is still an energy-intensive technology. For example, although reverse osmosis (RO) membrane energy consumption for desalination has decreased from 8.0 kWh/m^3 to 3.4 kWh/m^3, it is still higher than the theoretical limit of 1.06 kWh/m^3 (assuming 35,000 mg/L of seawater with the typical 50% recovery) [2, 3]. Advanced energy recovery devices are expected to be available soon, and the specific energy consumption (SEC) will be diminished to < 2.5 kWh/m^3 [4]. Nevertheless, this consumption is still higher than the theoretically limited value for seawater desalination; 1.06 kWh/m^3 (assuming 35,000 mg/L of salt in seawater and a typical recovery of 50%) [5]. Additionally, membrane fouling such as crystalline fouling, organic fouling, colloid fouling, and biofouling result in low efficiency of membrane performance, eventually leading to high operating and maintenance costs [6-9].

Various approaches to reduce energy consumption and prevent membrane fouling have been researched. An approach to develop the high performance membrane is limited to using conventional polymer membranes due to the ‘trade-off’ phenomenon between permeability and selectivity [9, 10]. Another approach is to make an antifouling membrane where surface is modified to be more hydrophilic, smoother, and more negatively (or neutrally) charged [11]. In addition, the act of embedding antibiotics in the active layer of membranes has been studied [12, 13]. To satisfy both approaches, a novel membrane that converges nanotechnology and membrane technology has been suggested [14, 15]. Among various nano-materials, carbon nanotubes (CNTs) have been utilized due to its fast water transport and antimicrobial properties. These properties are in order to make a high performance membrane with antifouling property [16-18]. However, the feasibility of CNT membranes has not fully investigated since they are still in the laboratory stage of development and not yet commercially available. Fabrication of CNT membranes, which have controlled geometry, porosity, and pore shapes, is also challenging [19].

1.2. Objectives

Three types of CNT membranes such as open-ended vertically aligned (VA) CNT membrane, dense-array outer-wall CNT membrane and mixed (matrix) CNT membranes were evaluated and compared with commercial membranes in terms of their permeability, rejection property and biofouling tendency. For this purpose, the extensive studies of following topics were conducted.

1) To evaluate the performances of open-ended VA CNT membranes in terms of water flux and rejection compared to commercial UF membrane with similar pore size:

   For this purpose, characteristics of the fabricated open-ended VA CNT membranes such as pore size, pore density, hydrophilicity, and surface roughness are measured by TEM images, SEM images, contact angle analyzer, and atomic force microscopy, respectively. The flux and rejection of VA CNT membranes are evaluated by utilizing various solvents and polyethylene glycol polymer, respectively. Furthermore, the biofouling tendency of the open-ended VA CNT membrane is performed in a lab-scale cross-flow membrane system.

2) To develop dense-array outer-wall CNT membranes with much improved water flux and anti-biofouling property

For this purpose, pore size of dense-array outer-wall CNT membranes were determined by pore-flow solute transport model with dextran. Water permeability was measured by a modified dead-end filtration system. Additionally, bacteria adhesion test was performed to evaluate the anti-biofouling property.

3) To evaluate the performances of mixed CNT membranes compared to commercial RO membrane:

For this purpose, the performance of mixed CNT membrane was compared to the commercial RO membrane in terms of water permeability, salt rejection, fouling tendency and energy consumption. Additionally, new fabrication method of mixed CNT membrane was suggested to enhance anti-biofouling property.

2. Literature Review

2.1. Carbon Nanotube Membrane for Water Treatment

2.1.1. Basic information of CNT

Carbon nanotube is defined as an allotrope of carbon with a cylindrical nanostructure. Since carbon nanotube (CNT) was successfully synthesized [20], various applications of CNTs have been investigated including their use in medical devices, chemical sensors, and environmental technologies [21-23]. A variety of techniques have been explored for the production of CNTs, including arc discharge [24] and laser deposition [25]. Typically, the growth of CNTs on a metal catalyst such as iron (Fe), nickel (Ni), or cobalt (Co), is employed during a chemical vapor deposition (CVD) process [26]. The cylindrical shape of a single walled nanotubes (SWNT) can be imagined virtually by wrapping a layer of graphite called graphene [27]. The way graphene winds can be described by a pair of indices (*n*, *m*). The indices *n* and *m* are integers indicating the number of unit vectors along 2 directions of graphene (Figure 2-1) [28]. The inner diameter of a nanotube can be calculated from the 'rolled up' vector as follows [29].

$$d_{in} = \left(\frac{a}{\pi}\right)\sqrt{\left(n^2 + m^2 + nm\right) - 2r_c} \qquad \text{(Eq. 2-1)}$$

(d_{in} = inner diameter of nanotubes, a = lattice parameter of graphene (=2.46 Å), and r_c = van der Waal's radius of a carbon atom (1.7 Å))

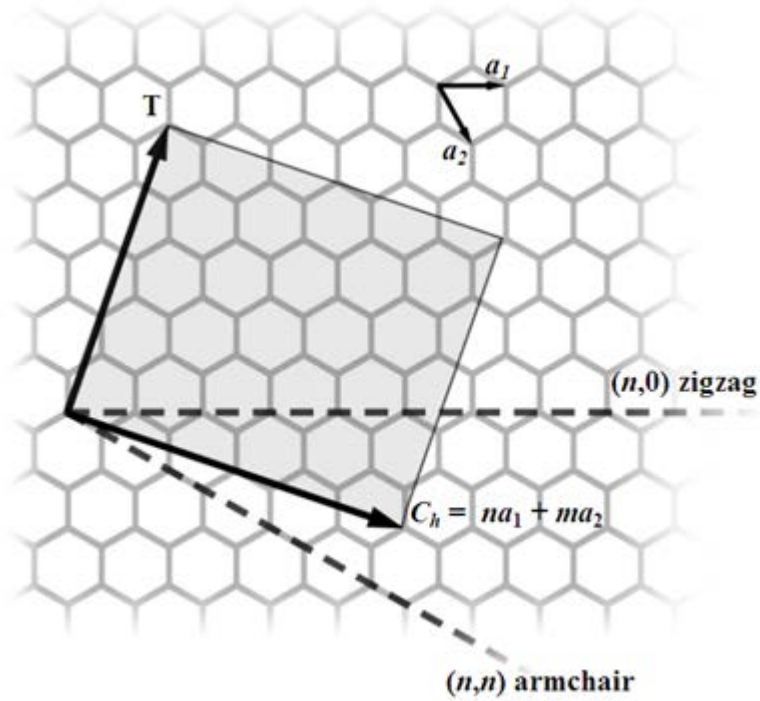

Figure 2-1. Letters (n, m) indicate the number of unit vectors in an infinite graphene sheet and C_h is a ‘rolled up’ vector. T denotes the tube axis, and a_1 and a_2 are the unit vectors of graphene. If m = 0, the CNTs are called ‘zigzag’. If n = m, the CNTs are called ‘armchair’. In other cases, the CNTs are ‘chiral’ [17].

2.1.2. Nanofluidics of CNT membranes

The inner walls of CNTs are smooth and hydrophobic. Movement of water molecules that pass through a nanotube's interior can be explained by the ballistic motion of water chains (1D wire) due to strong hydrogen bonding between water molecules and minimal interaction with the CNT inner wall [30-32] (Figure 2-2).

The mass movement of water molecules through CNTs does not follow conventional fluid mechanics [33]. Thus, it is necessary to introduce a plausible transport phenomenon called 'nanofluidics.' In this novel theory, it is assumed that the fluid flowing through a nano-channel has a slip length with no friction [34]. Adopting the slip-flow condition, the Hagen-Poiseuille equation can be adapted as follows [33].

$$Q_{Slip} = \frac{\pi\left(d/2\right)^4 + 4\left(d/2\right)^3 \cdot L_S(d)}{8\mu} \cdot \frac{\Delta P}{L} \qquad \text{(Eq. 2-2)}$$

(Q_{Slip} = water flux depending on slip length, d = diameter of the nano-channel, ΔP = pressure difference between both ends of the nano-channel, μ = the viscosity of water, and L = the length of nano-channel)

The slip length ($L_s(d)$) can be computed as follows:

$$L_S(d) = L_{S,\infty} + \frac{C}{d^3} \qquad \text{(Eq. 2-3)}$$

($L_{S,\infty}$ = slip length of the graphene surface (assumed to be 30 nm), and C is a fitting parameter. In addition, the diffusion coefficient of water molecules is estimated at D_{H2O} = 0.9423 $\times 10^{-9}$ m^2/s for a nanotube of 2.1 nm diameter [35])

In this manner, the CNT membrane can be defined as a membrane that uses the inner and/or outer surface of nanotubes as nano-channels for transporting fluid. With this configuration, applications for the CNT membrane may not be limited to desalination processes. Additionally, it may be feasible to extend the use of CNT membranes to include separation technologies used for oil and gases [36-38].

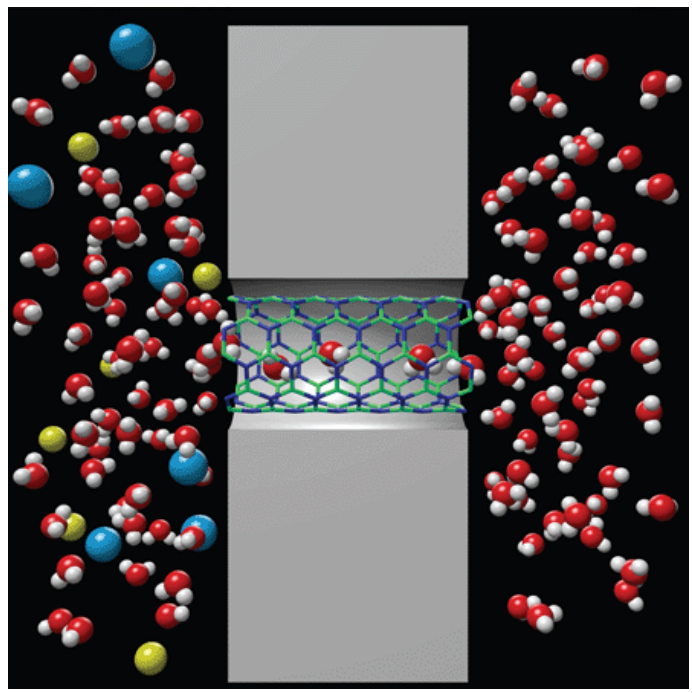

Figure 2-2. Movement of water molecules through a SWNT [25].

2.1.3. Types of CNT membranes

CNT membranes can be classified into four categories according to fabrication methods; (1) open-ended vertically aligned (VA) CNT membrane, (2) dense-array outer-wall CNT membrane, (3) mixed (composite) CNT membrane and (4) Template synthesized CNT membrane [18] (Figure 2-3).

For open-ended VA CNT membrane, CNTs are arranged straight up and perpendicular to the membrane surface. In this configuration, CNTs are bound to each other by an organic or inorganic filler material. The first prototype for an open-ended VA CNT membrane was introduced by the Hinds research group [39]. After being grown on an iron catalyst using the CVD process, MWNTs were embedded in polymeric filler composed of polystyrene (PS). In addition, Holt, et al. developed a micro-electro mechanical system (MEMS)–compatible fabrication process for another type of open-ended VA CNT membrane [40]. Inorganic filler (silicon nitride, Si_3N_4) was employed to ensure that water flowed only through the nano-channels and did not permeate the nanotube-filler matrix.

Dense-array outer-wall CNT membrane is defined as a membrane based on the interstice between CNTs in VA CNTs. Srivastava and coworkers firstly introduced this CNT membrane as hollow cylinders of aligned MWCNTs (few centimeters of height) along with the walls of a tubular quartz reactor. This hollow type cylinder, composed of radially oriented MWCNTs (300 – 500 μm length), was used for liquid and gas filtration [41].Due to the difficulty of the

fabrication of dense-array outer-wall CNT membrane, it has been barely reported.

Mixed CNT membranes have a structure similar to that of the conventional polymer membranes, where CNTs are embedded into the polymer layer (i.e. polyamide and polysulfone). An earlier model of a mixed CNT membrane was mainly designed to upgrade UF membrane with CNTs. MWNTs (up to 5% by weight volume) were blended with polysulfone (PSf) and water fluxes were measured under an operating pressure of 1 – 4 bars [42]. Intriguingly, the MWNT/PSf membrane showed 2 pieces of conflicting data according to the molecular weight (M.W.) of solute. For an aqueous solution of poly-ethyleneoxide (PEO) 100,000, the solute rejection efficiency was high (> 95%) and the water flux was measured at 14 – 17 L m^{-2} h^{-1} (LMH). On the contrary, for aqueous solution of poly-vinylpyrrolidone (PVP) 55,000, the solute rejection efficiency was reduced by 20 – 60%, whereas the water flux was increased to > 40 LMH.

Template-synthesized CNT membrane is fabricated by the adsorption of carbon materials on the inorganic membrane mostly (i.e. ceramic and anodized aluminum oxide (AAO) membranes). For example, AAO membrane has about 20 – 200 nm of pore size and its tortuosity is close to 1. By using chemical vapor deposition (CVD) method, carbon atom can adsorb on the pore walls of AAO membrane. Then, pore walls are coated with carbon atoms whose shape is similar to carbon nanotube.

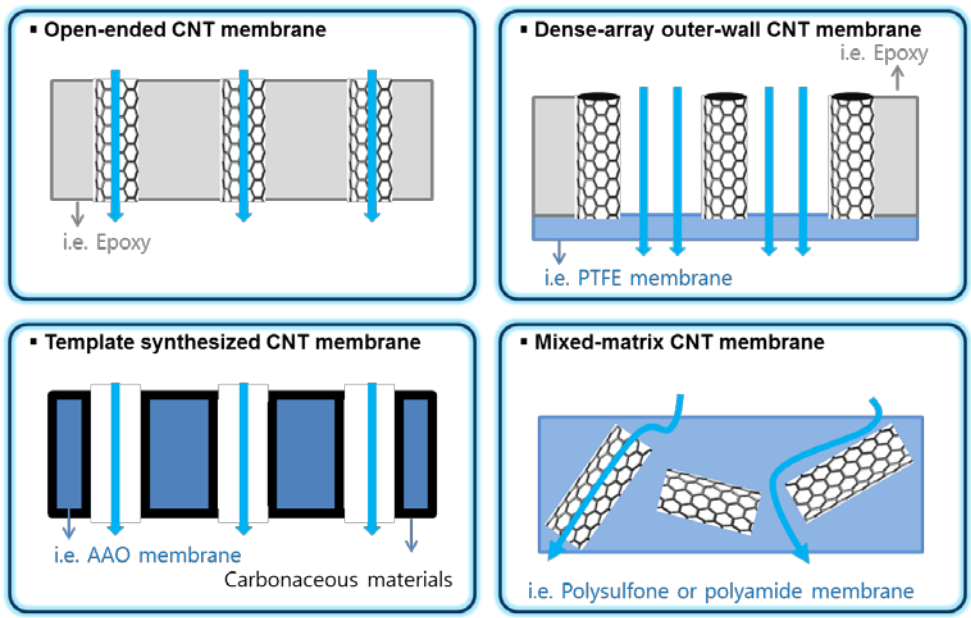

Figure 2-3. Types of CNT membranes according to fabrication methods.

2.2. Properties of Carbon Nanotube Membrane

Carbon nanotube has several advantages as a novel material such as fast water transport, antimicrobial property, ballistic charge carrier transport, high mechanical property, high thermal conductivity, high chemical resistance, large surface area and high aspect raio [43]. Especially, in terms of membrane fabrication with CNT for water treatment, fast water transport and antimicrobial property are useful for making a high performance membrane and an anti-fouling membrane, respectively (Figure 2-4).

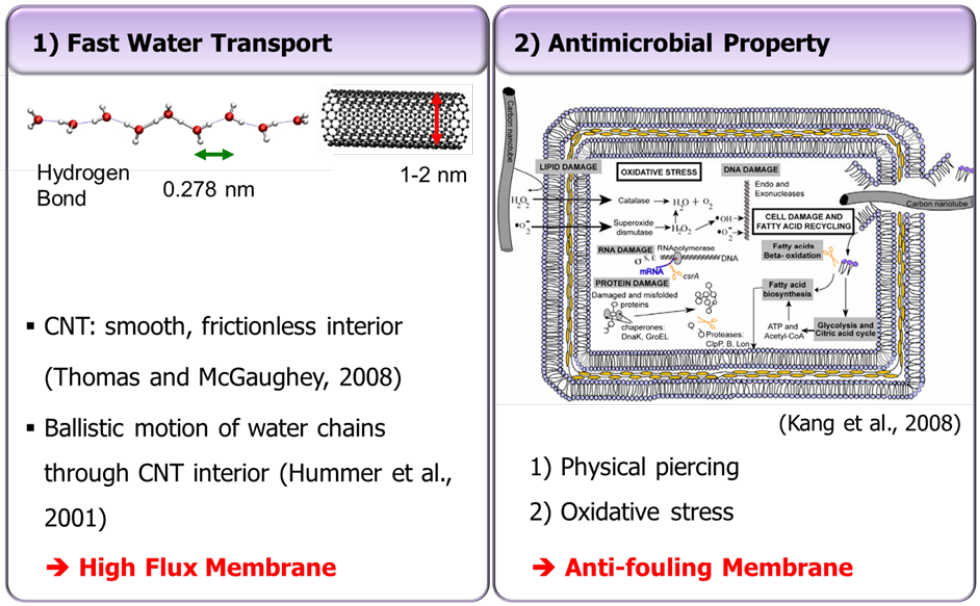

Figure 2-4. Fast water transport and antimicrobial property of CNT.

2.2.1. Fast transport of water molecules through CNTs

CNT membranes for water treatment have been mostly focused on the fabrication of high performance membrane by using fast transport of water molecules through CNTs. This fast transport through CNTs has been explained by surface chemistry, fluid dynamics and thermal dynamics [44]. Classical continuum hydrodynamics governed by Navier-Stokes Eq. successfully describes the dynamic of fluid flow on the macroscopic scale. However, it is independent of the nature of the molecular structure and configuration [45]. Because classical continuum hydrodynamics has a limitation to explain the dynamic of fluid flow on the nano-scale, nanofluidics has been developed with the advance of nano-technology.

Several researches of fast water flux on the CNT membrane were reported with open-ended VA CNT membranes. Previous studies of the VA CNT membrane investigated analysis flow properties [46-48] or evaluated the feasibility for desalination technology by molecular dynamics (MD) simulation [29, 49]. Pore diameters of open-ended VA CNT membrane reported in previous studies were much larger than 1 nm (hydrated radius of Na^+ ion: 0.716 nm, Cl^- ion: 0.664 nm [50-52]). Since it is obviously difficult to remove salt ions due to their size, previous studies focused on the high water flux through CNTs. For example, Hinds and coworkers performed a series of supplementary pressure driven flow experiments with the MWNT/PS membrane, and found that water

flow rates were increased 4-to 5-fold over those of a conventional fluid flow, which was estimated from the Hagen-Poiseuille (HP) equation [47]. Originally, the Hinds research group developed the open-ended CNT membrane as a chemically selective gate keeper, which could separate different sized enzymes [53]. Thus, they did not report ion selectivity, which is strongly related to desalination potential in the desalination process. In addition, Holt, et al. developed open-ended VA CNT membrane [40] which employed nanotubes with an inner diameter < 2 nm (average I.D. = 1.6 ± 0.4 nm) to enhance the nanofluidic effect. Holt and his collaborators reported water fluxes that were > 3-fold greater than the non-slip hydrodynamic flow as calculated from the Hagen-Poiseuille equation [40].

Mixed CNT membrane also showed higher water flux than commercial polymer membrane. For example, Choi and his coworkers presumed that plugging effect between both size of nano-pores and solute molecule might contribute to differences in the solute rejection efficiencies [42]. Thus, it seemed to be a dilemma accomplishing higher permeability and rejection rate at the same time with the mixed CNT membrane. In addition, functionalized MWNTs blended with PSf were prepared for UF membranes [54]. MWNTs were modified by attaching isocyanate and isophthaloyl chloride (ICIC) functional groups, and the adsorption of protein on the membrane surface was suppressed. Thus, it was anticipated that a functionalized MWNT/PSf membrane would

alleviate membrane biofouling. Also, a mixed CNT membrane for RO membrane was reported that its water flux was 4.05 LMH/bar [55]. Compared to a commercialized brackish water (BW) RO membrane whose water flux ranged from 2.5 – 3.0 LMH/bar, the mixed CNT membrane demonstrated ~1.5-fold higher water flux.

Fluid flow through CNTs has drawn much interest because of frictionless or near frictionless flow [47, 48, 56-58] in CNTs. Nevertheless, the water permeance through CNT membranes [46, 48, 59] was initially not that much different from that attainable with a commercial polysulfone membrane [60], which is around several hundred liters per square meter per hour (LMH)/bar. Only recently did the permeance reached 2,400 LMH/bar [60]. This flux is not much larger than the flux attainable with non-CNT membranes. Yet, the observed flow rate in a carbon nanotube is several orders of magnitude greater than that predicted by conventional fluid flow theory [47]. This fact suggests that the permeance through CNT membrane should and could be made much larger than that reported so far.

In addition, desalination potential of CNT membranes were studied by molecular dynamics (MD) simulation, which is a major tool to research the dynamics of small molecules through nano-structured pore [29, 49]. It helps to understand the phenomenon of water or single ion flow through nano-pore. Generally, the mechanism of ion rejection on the membrane can be explained by

steric effect and Donnan equilibrium theory. Steric effect is the phenomenon that the hydrated ions are sieved by smaller pores. Corry et al. reported that 0.49 nm of inner wall diameter for CNT showed 100% of ion rejection and larger diameters such as 0.58 nm and 0.75 nm showed a decreased ion rejections like 95% and 58%, respectively [29]. On the other hand, Donnan equilibrium theory is the repulsion forces between surface charge and the charge of either co-ion or counter-ion. For example, introducing the functional groups on the CNTs increased the ion rejection of CNT membranes due to enhanced repulsion forces between surface of CNT membrane and ions. However, in this case, water transport was decreased because the attraction force between water molecules and the surface of CNT at the end was increased [49].

2.2.2. Antimicrobial properties

Figure 2-5 shows the schematic of *E. coli* K12 gene expression stress responses under exposure to CNTs [61]. As shown in Figure 2-5, major mechanisms for microorganism inactivation by CNTs can be explained by physical piercing and oxidative stress. It shows that CNTs not only produce mechanical damage and subsequent cell disruption in bacteria, but may also generate oxidative stress, as previously described in the literature [62]. Liu et al. showed the both gram-negative bacteria (i.e. *E. coli* and *P. aeruginosa*) and gram-positive bacteria (i.e. *S. aureus* and *B. subtillis*) were inactivated by that SWNTs physically pierced

cell wall of bacteria through SEM and AFM images [63, 64]. On the other hand, other studies insisted that residual catalysis (i.e. Fe) whose can be remained after CNT growth can generate reactive oxygen species such as superoxide [65] and hydrogen peroxide [66] for microorganism inactivation [67, 68].

Table 2-1 summarized the effects of characteristics of CNT and experimental conditions for microorganism inactivation. Although the antimicrobial property of CNT has been studied for a long time, the results of each literature were controversial due to the different characteristics of CNTs by manufacturing processes and dispersion processes. Nevertheless, characteristics of CNT and experimental conditions described in Table 2-1 were reported with consistency relatively. It appears that smaller (or SWNT), shorter, more purified, more dispersed, higher concentration, longer treatment time, faster mixed speed, deposited form and metallic structured CNT has a stronger antimicrobial property. Metallic CNTs could inactivate more bacteria by acting as a conductive bridge over the insulating lipid bilayer, releasing cellular energy into the external environment. On the other hand, the controversial issue was arisen from the effect of CNT for gram-negative bacteria and gram-positive bacteria. While Liu et al. [63] suggested that gram-negative bacteria were more resistant to CNTs due to the complex outer membrane [69], Kang et al. [70] stated that CNTs were less affected to gram-positive bacteria, resulting from that robust peptidoglycan layer enhanced structural rigidity and resistance of cell wall [71].

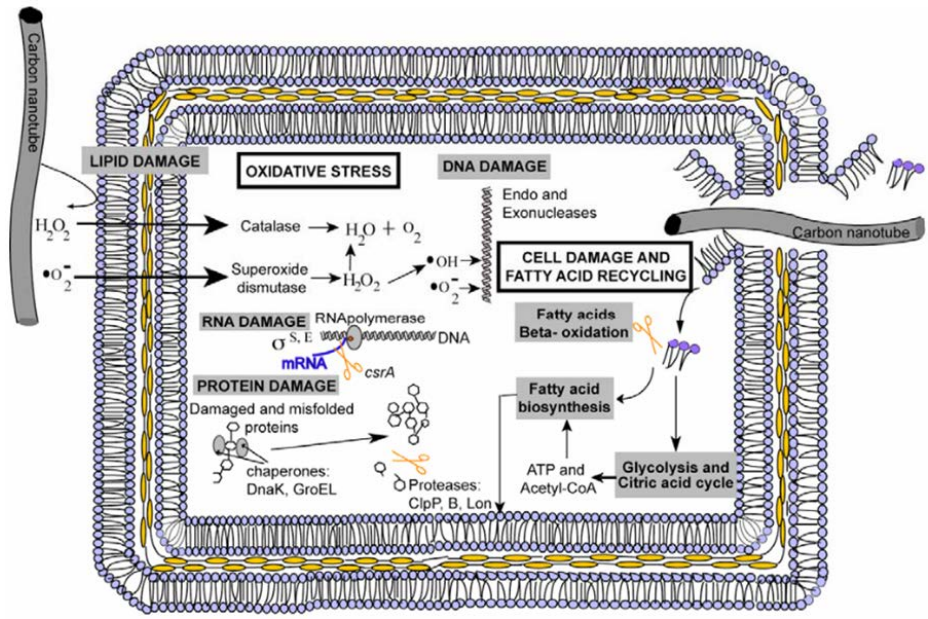

Figure 2-5. Schematic of mechanism of bacteria inactivation by CNTs [61].

Table 2-1. Effects of characteristics of CNT or experimental conditions for microorganism inactivation.

Characteristics of CNT / experimental conditions	Priorities for microorganism inactivation	Ref.
Size (or wall number)	SWNT > MWNT	[61]
Length	shorter	[72]
Purity	more purified	[73]
Dispersity	more dispersed	[63]
Concentration	higher	[63]
Treatment time	longer	[74]
Mixing speed	faster	[63]
Shape	deposited > suspended	[75]
Electrical structure	more metallic	[76]

3. Open-ended Carbon Nanotube Membrane

3.1. Materials & Methods

3.1.1. Materials

Si wafer (diameter: 4 inch, P-type, Boron dopant) was purchased from Dasom RMS (Republic of Korea) for CNT growth. Epoxy resin (Epon 828, Miller-stephenson Inc., CA) was used for filling agent to fabricate open-ended VA CNT membrane. Polysulfone UE4040 membrane (Woongjin Chemical, Republic of Korea) was used as a commercial UF membrane. Deionized water (Barnsted NANO Pure, USA), hexane, octane, decane, and dodecane (Sigma Aldrich, USA) were used for permeability measurements. Polyethylene oxide (PEO, molecular weight: 100 kDa) was used for the rejection test. For the biofouling occurrence, *Pseudomonas aeruginosa* PAO1 GFP (Center for Biofilm Engineering, Montana State University) was used as a model bacterial strain where the initial bacterial concentration was about 1×10^7 CFU/mL and the feed solution was composed of 10 mM NaCl, 10 mM sodium citrate, and 0.1% tryptic soy broth.

3.1.2. Synthesis of open-ended vertically-aligned (VA) CNT membrane

Vertically-aligned (VA) CNTs were synthesized onto a Si wafer from Fe catalyst using the water-assisted thermal chemical vapor deposition method [77, 78]. An

18 nm thick aluminum was used as a buffer layer between the Si wafer and Fe catalyst to prevent catalytic diffusion. The temperature of the furnace was ramped up 810°C in 1 min. High-purity acetylene and Ar gas were inserted in the furnace as the carbon precursor and carrier gas, respectively. During the VA CNTs growth process, a small and controlled amount of water vapor acts to promote and preserve catalytic activity [79]. The grown VA CNTs were analyzed by FE-SEM (field emission scanning electron microscope, S-48000, Hitachi, Japan).

Figure 3-1 shows the schematic of the open-ended VA CNT membrane manufacturing. Synthesized VA CNTs were transferred from a Si wafer to a tape (Figure 3-1(a)) and then are directly fixed onto the bottom of the cast. As shown in Figure 3-1(b), epoxy resin filled up the vacant areas of the VA CNTs under vacuum (about 0.1 bar). Epoxy was selected due to the simple structure that can penetrate VA CNTs vacancy. After the epoxy-VA CNTs matrix hardened, it was cut by microtome (HM 340 E, MICROM Lab., Germany) in 40°C under a halogen lamp to make a homogeneous open-ended VA CNT membrane (Figure 3-1(c)).

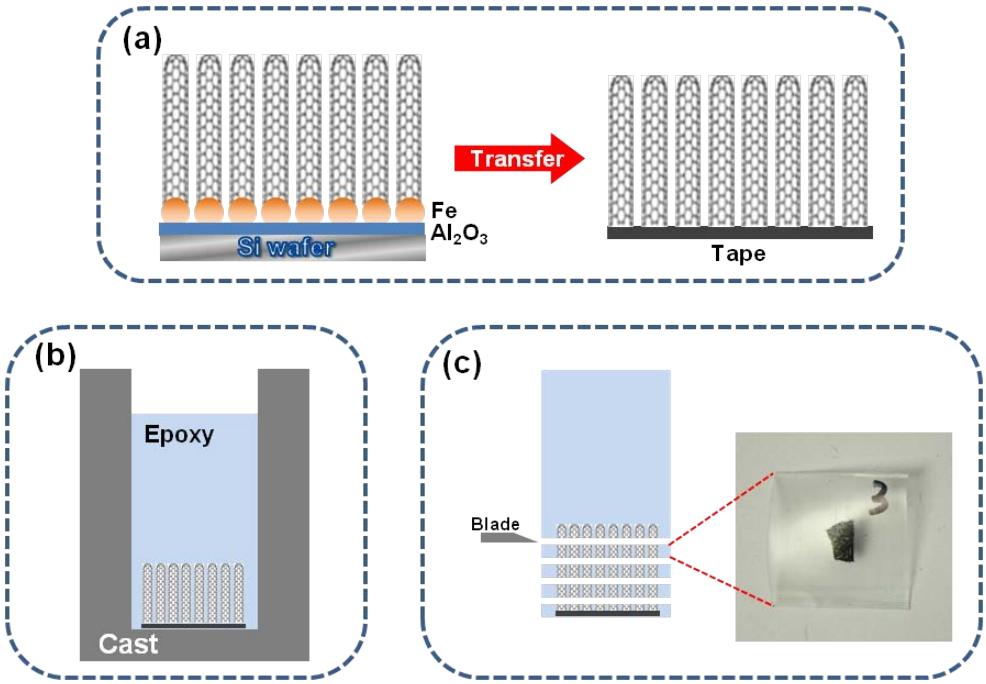

Figure 3-1. Schematic of the open-ended vertically-aligned carbon nanotube (VA CNT) membrane manufacturing; (a) transfer of VA CNTs to the tape, (b) infiltration of epoxy into the vacant areas of VA CNTs utilizing the cast, and (c) fabrication of the open-ended VA CNT membrane utilizing microtome.

3.1.3. Characterization

The manufactured open-ended VA CNT membrane was characterized by measuring the pore size, pore density and thickness as well as by analyzing the membrane surface properties (i.e. hydrophilicity and roughness). The pore size was determined using the average values of the synthesized VA CNTs' inner diameter. The inner diameter of the VA CNTs was measured by TEM (transmission electron microscopy, JEM-2100, JEOL, Japan) after dispersion into NMP (N-methylpyrrolidone), then dried onto the grid (HC200-Cu, Electron microscopy sciences, USA). Pore density and surface morphology were analyzed by TEM (LIBRA 120, Carl Zeiss, Germany) after making it about 20 nm of thickness by ultramicrotome (MTX, RMC, USA). The pore size and pore density were determined by measuring 100 CNTs from more than 50 TEM images. Thickness was measured by utilizing the electronic micrometer (Schut Geometrical Metrology, Groningen, Netherlands). The effective area of the open-ended VA CNT membrane was about 0.1 cm^2 as calculated by the image program (Dinocapture, Dino Lite, Taiwan). A commercial polysulfone UF membrane was selected to compare with the open-ended VA CNT membrane since both pore sizes are similar. The pore size, pore density and surface morphology of the commercial UF membrane were analyzed by FE-SEM.

Membrane surface properties such as hydrophilicity and roughness were measured by the contact angle analyzer (DSA 100, KRÜSS, Hamburg, Germany)

with the captive bubble method [80, 81] and scanning probe microscope (SPM; SPA-400, Seiko Instrument, Japan), respectively. At least five measurements were made for both the contact angle analysis and SPM measurement to examine reproducibility, where the average value with standard deviation was reported. Surface morphology of the open-ended VA CNT membrane was analyzed by FE-SEM. Additionally, mechanical strengths of both the open-ended VA CNT membrane and the UF membrane were measured by using a universal testing machine (Lloyd LR-10K). The dumbbell specimens were prepared using the ASTM standard D638 (Type V specimens dog-bone shaped samples). The gauge length and cross head speed were 15 mm and 10 mm min^{-1}, respectively.

3.1.4. Membrane performance test

Membrane performance experiments such as permeability measurement and rejection test were conducted in the dead-end membrane filtration system pressurized with N_2 gas (Figure 3-2). Prior to the performance evaluation of the open-ended VA CNT membrane, control experiments were carried out to examine whether a solvent penetrates through inside the CNTs on the open-ended VA CNT membrane. Two control samples were prepared as shown in Figure 3-3. One sample was made of only epoxy resin, which is the filler of the open-ended VA CNT membrane and whose shape was the same as the open-ended VA CNT membrane. The other was the one-side blocked open-ended VA CNT membrane made by cutting only the top part of the epoxy-VA CNTs matrix by microtome in the fabricating process of open-ended VA CNT membranes. In this case, one side of the open-ended VA CNT membrane was opened and the other side was presumed to be blocked with partially protruded capped VA CNTs and epoxy resin. SEM-EDS analysis was provided to elucidate whether CNT caps were protruded from the membrane surface. The ratios of C/O was VA CNT membrane sample (8.4), one-side opening sample (5.5), and epoxy resin sample (4.8) in decreasing order (Table 3-1). The larger C/O ratio of one-sided opening sample than that of epoxy resin sample indicates that capped nanotubes of one-side opening samples were partly protruded from the surface of the one-sided opening sample. Although capped nanotubes were partly protruded from the

surface, no permeate was observed under harsher condition (20 bar for 18 h) (cf. water permeability was measured under 2 bar for 5 min). In addition, SEM analysis was performed to examine if the gaps between CNTs are well filled in the open-ended VA CNT membrane, no gap between VA CNT and epoxy resin was observed in the open-ended VA CNT membrane (Figure 3-4). These results seem that solvent was dominantly flowed through the internal of CNTs on the open-ended VA CNT membrane.

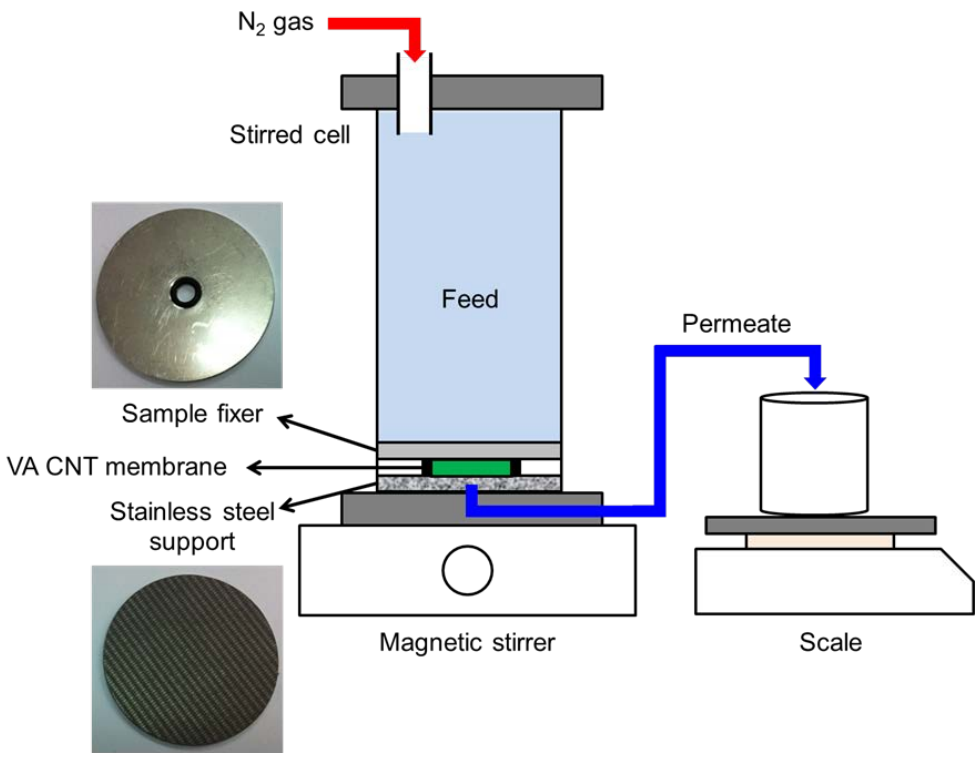

Figure 3-2. Schematic of the dead-end membrane filtration system in this study.

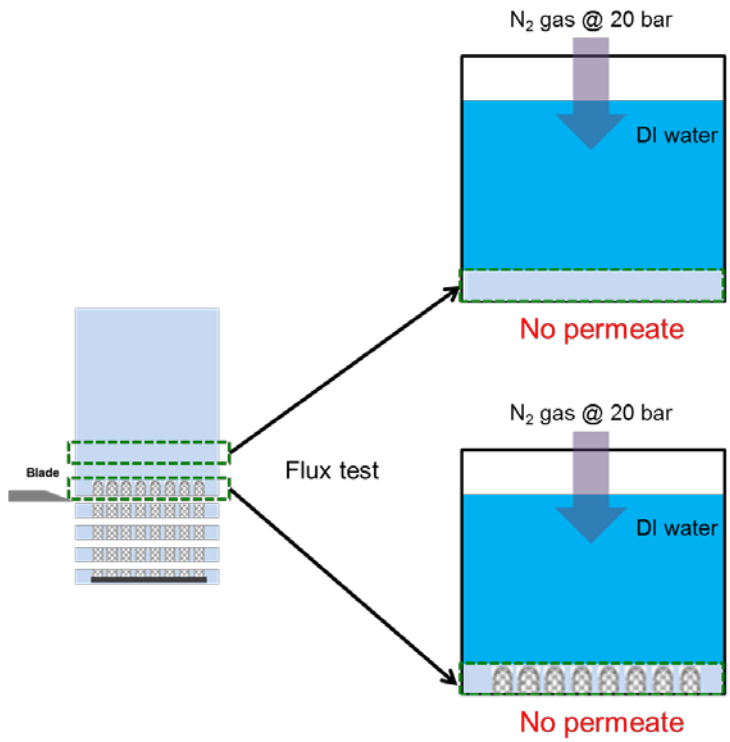

Figure 3-3. Schematic of control experiment for the integrity test of the open-ended VA CNT membrane.

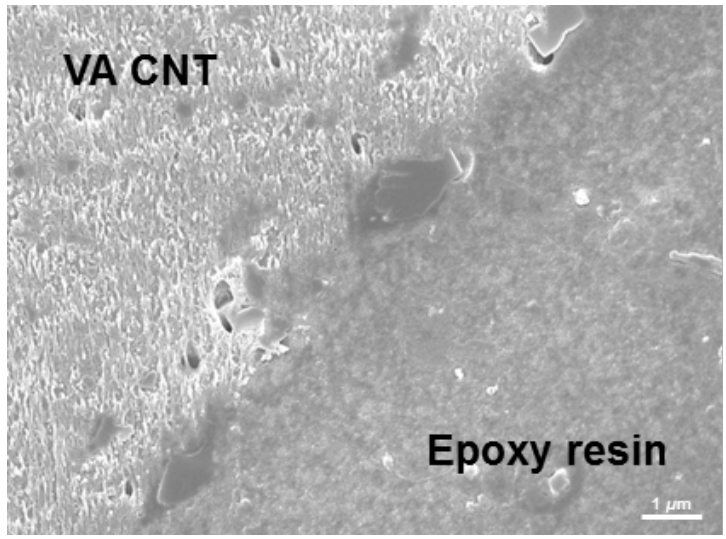

Figure 3-4. Top-view SEM image of the open-ended VA CNT membrane.

Table 3-1. Atomic % of the surface of open-ended VA CNT membrane samples, one-side opening samples, and epoxy resin samples analyzed by SEM-EDS.

	Atomic %		
	open-ended VA CNT membrane sample	One-side opening sample	Epoxy resin sample
C	89.2 ± 1.3 [a]	84.6 ± 0.5	82.7 ± 0.7
O	10.8 ± 1.3	15.4 ± 0.5	16.9 ± 0.7
C/O ratio	8.4 ± 1.1	5.5 ± 0.2	4.8 ± 0.2

[a]: performed triplicate for reproducibility.

Permeability of the open-ended VA CNT membrane was obtained by measuring the weight of the permeate for 5 min and compared to that of the UF membrane. Deionized water, hexane, octane, decane, and dodecane, chosen according to the hydrophilicity and viscosity of solvents, were used to evaluate the flow property. Table 3-2 summarizes the solubility parameter, viscosity and density of various solvents in this study. The solubility parameter is defined a numerical estimate of the degree of interaction between materials [82, 83]. In other words, the solubility parameter indicates the degree of affinity between solvents in this study. For example, the hydrophilic water has the high solubility parameter (45.9 $MPa^{0.5}$) while hexane has the low solubility parameter (14.9 $MPa^{0.5}$). It indicates that hexane has low affinity to water, meaning hexane is hydrophobic. Therefore, the solubility parameter can be used as a standard to determine the hydrophilicity of solvents as previously reported [84, 85]. The viscosities of the solvents were hexane (0.3 cP), octane (0.5 cP), decane (0.9 cP), water (1.0 cP) and dodecane (1.5 cP), in increasing order. The solvent density was used to convert the permeate flux into the permeate weight. The solvents that have lower solubility parameters than water, such as alcohol and methanol, were not considered due to the potential damage they could inflict on the open-ended VA CNT membrane.

Table 3-2. Density, kinematic viscosity and solubility parameter of various solvents used for permeability measurement.

Solvent	Solubility parameter ($MP^{0.5}$)[a]	Kinematic viscosity (cP)[b]	Density (g/cm^3)[b]
Water	45.9	1.0	1.0
Hexane	14.9	0.3	0.66
Octane	13.8	0.5	0.7
Decane	13.4	0.9	0.74
Dodecane	13.2	1.5	0.75

[a]: calculated by $\delta = \sqrt{\frac{\Delta H_v - RT}{V_m}}$ (ΔH_v: heat of vaporization, R: ideal gas constant, T: absolute temperature, V_m: molar volume) [83]

[b]: referred to [86]

The enhancement factor (ε, Eq. 3-1) was employed to express the measured flux in this study over the flux calculated by Hagen-Poiseuille equation, which indicates the flow under a no-slip condition (Eq. 3-2) [48]. This factor can assess the extent of the increased flux on the open-ended VA CNT membrane. Slip length (L_s, Eq. 3-3), expressing the increased flux on the open-ended VA CNT membrane as well, was calculated from the slip flow Hagen-Poiseuille equation (Eq. 3-4) [34] which is equivalent to the measured flux on the open-ended VA CNT membrane in this study.

$$\varepsilon = \frac{Q_{measured}}{Q_{no\text{-}slip\ HP}} \qquad \text{(Eq. 3-1)}$$

(ε: enhancement factor, $Q_{measured}$: measured flux, $Q_{no\text{-}slip\ HP}$: flux based on the no-slip condition of the Hagen-Poiseuille equation)

$$Q_{no\text{-}slip\ HP} = \frac{\pi(d/2)^4}{8\mu}\frac{\Delta P}{L} \qquad \text{(Eq. 3-2)}$$

(d: pore diameter (= CNT inner diameter), ΔP: pressure difference (applied pressure in this study), μ: viscosity of solvent, L: channel length (= membrane thickness))

$$L_s = \frac{d\left(\frac{Q_{measured}}{Q_{no\text{-}slip\ HP}} - 1\right)}{8} \qquad \text{(Eq. 3-3)}$$

(L_s: slip length)

$$Q_{slip\ HP} = \frac{\pi((d/2)^4 + 4L_s(d/2)^3)}{8\mu}\frac{\Delta P}{L} \qquad \text{(Eq. 3-4)}$$

($Q_{slip\ HP}$: flux based on the slip condition of the Hagen-Poiseuille equation (= $Q_{measured}$))

Water permeability under various applied pressures and various temperatures were measured to examine whether the open-ended VA CNT membrane followed the conventional membrane properties that water permeability increases by increasing either applied pressure or temperature [87] from 2 to 10 bar for pressure and from 10°C to 30°C for the temperature. Standard conditions for evaluating the membrane performance were 2 bar of applied pressure and 20°C, unless specific conditions were mentioned. All the permeability measurements were done at least three times with different membranes to examine reproducibility, and then the average value was reported.

200 mg/L of PEO solution was used in the dead-end membrane filtration

system under 10 bar with 600 rpm of stirring speed at 20°C. The concentration of PEO solution was measured in terms of total organic carbon (TOC) by using a TOC analyzer (Sievers 5310C, GE Analytical Instruments, USA). The rejection ratios using Eq. 3-5 were calculated from the concentration of both the feed and the permeate.

$$R(\%) = \frac{C_f - C_p}{C_f} \times 100 \qquad \text{(Eq. 3-5)}$$

(C_f: feed concentration, C_p: permeate concentration)

3.1.5. Analysis of membrane biofouling tendency

The biofouling tendency of the open-ended VA CNT membrane compared to the UF membrane was carried out in a lab-scale cross-flow membrane system [88, 89]. The initial water permeability was fixed at 700 LMH/bar due to the high permeability of the open-ended VA CNT membrane, and the cross-flow velocity was fixed at 100 mL/min. The control experiment was performed with only feed solution. Biofouling occurrence was induced after membrane conditioning with feed solution for 6 h. During the membrane conditioning, similar level of cake deposition on both the VA CNT membrane and the UF membrane was intended for fair comparison by adjusting the water permeabilities constantly. This similar cake layers were confirmed from the amounts of organic carbon deposited on

both membranes (as measured by TOC analyzer). TOC (total organic carbon) was measured after cake layers were detached by vortexing and sonication. After biofouling occurrence for 600 min, the water permeabilities of each membrane were observed and the bacterial concentration on each membrane surface were measured using the plate count method. Confocal laser scanning microscopy (CLSM; Eclipse 90i, Nikon, Japan) images were used to observe the bacterial attachment after staining with a BacLight Live/Dead bacterial viability kit (Molecular Probes, USA). More details are described in our previous studies [88, 89].

3.2. Results and Discussion

3.2.1. Characteristics of VA CNT and open-ended VA CNT membranes

The symmetric CNT property was observed in the VA CNT grown (Figure 3-5) by the water-assisted thermal chemical vapor deposition method, which is consistent with the previous study [77, 78]. Table 3-3 shows the characteristics of the open-ended VA CNT membrane in this study as compared to the commercial UF membrane. As shown in Table 3-3, the open-ended VA CNT membrane composed of CNTs-epoxy matrix had a slightly smaller pore diameter (4.8 ± 0.9 nm; Figure 3-6) and higher pore density (6.8×10^{10} #/cm^2; Figure 3-7) than the UF membranes (5.7 ± 2.5 nm, 8.8×10^{10} #/cm^2; Figure 3-8). The thickness of the open-ended VA CNT membrane (200 μm) was 2,000 times thicker than the thickness of the UF membrane (0.1 μm). In terms of membrane surface properties, the open-ended VA CNT membrane surface was more hydrophobic ($74.6 \pm 2.8° > 59.3 \pm 3.0°$) and rougher ($19.3 \pm 3.2$ nm > 5.8 ± 0.2 nm). The mechanical strength of the open-ended VA CNT membrane as observed from tensile strength and Young's modulus was weaker than the commercial UF membrane (Table 3-3). However, considering that maximum operating pressure of the commercial UF membrane is less than 2.78 MPa (provided by the manufacturer), the mechanical strength of the VA CNT membrane was good enough for the UF membrane process.

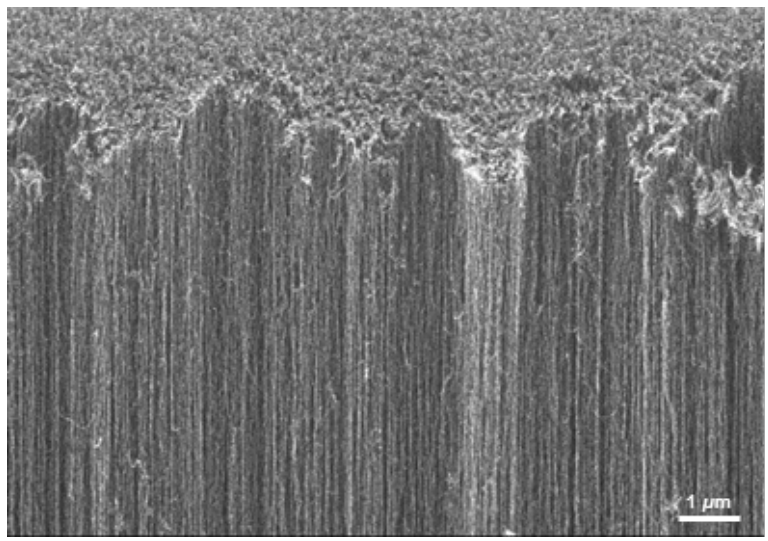

Figure 3-5. Cross-sectional SEM image of the VA CNT.

Table 3-3. The characteristics of the open-ended VA CNT membrane compared to the UF membrane.

	Open-ended VA CNT membrane	UF membrane [a]
Material	CNTs + epoxy	Polysulfone
Ave. pore diameter (nm)	4.8 ± 0.9 [b]	5.7 ± 2.5 [c]
Pore density (#/cm^2)	6.8×10^{10} [b]	8.8×10^{10} [c]
Thickness (μm)	~200	~0.1
Contact angle (°)	74.6 ± 2.8	59.3 ± 3.0
Surface roughness (nm)	19.3 ± 3.2	5.8 ± 0.2
Tensile strength (MPa)	13 [d]	93
Young's modulus (MPa)	500	830

[a]: UE4040 (Woongjin Chemical Co, Republic of Korea)

[b]: measured from TEM images in Figure 3-6 & 3-7

[c]: measured from SEM images in Figure 3-8

[d]: tensile strength of epoxy resin (Epon 828): 71 MPa (provided by the manufacturer)

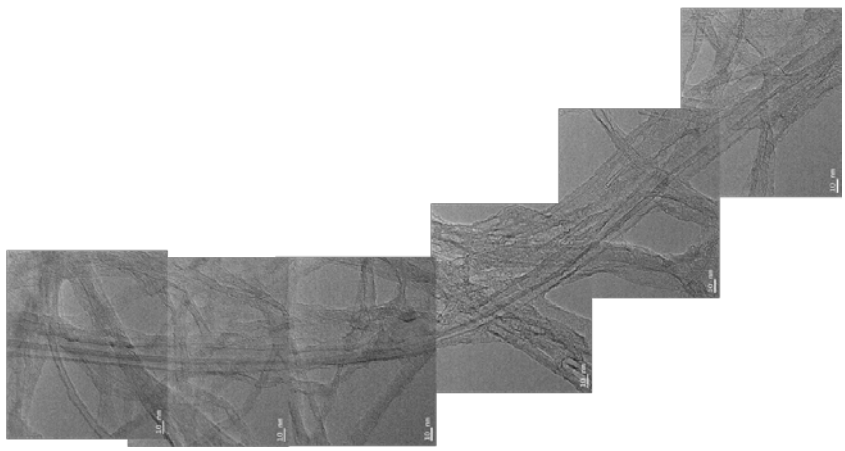

(a)

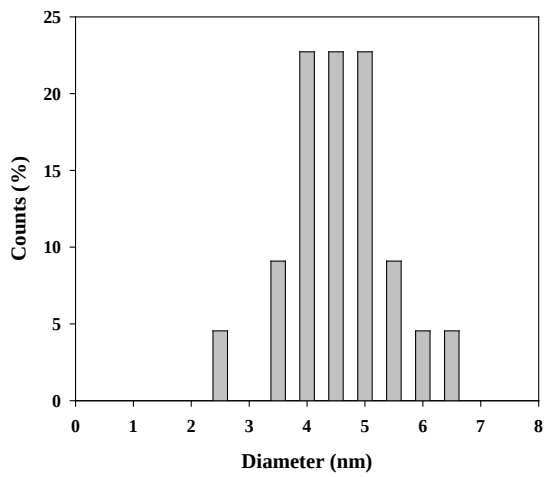

(b)

Figure 3-6. The characteristics of the VA CNT; (a) TEM images of VA CNTs and (b) diameter distribution of VA CNTs based on TEM images.

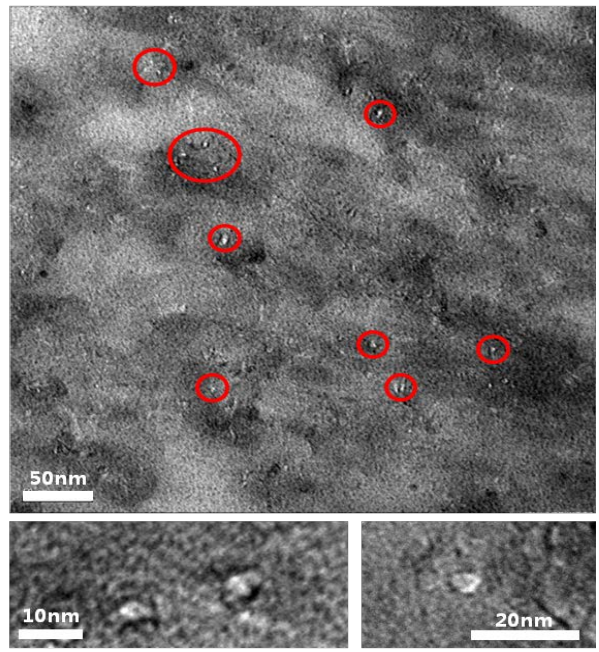

Figure 3-7. TEM images of the open-ended VA CNT membrane surface (red circle: cap-opened CNTs).

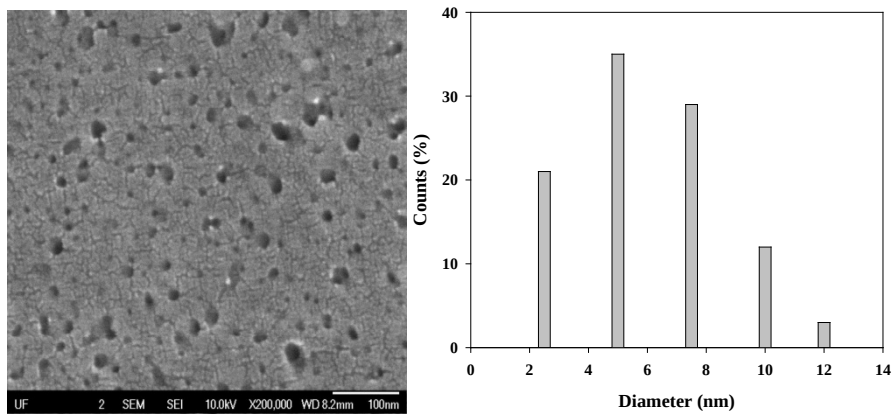

(a) (b)

Figure 3-8. The characteristics of the UF membrane; (a) SEM images of UF membrane surface and (b) pore diameter distribution based on SEM images.

3.2.2. Performances of open-ended VA CNT membrane

Figure 3-9(a) – (c) show the water permeability of the open-ended VA CNT membrane with its enhancement factor and water permeability changes under various applied pressure and temperature, respectively as compared to the commercial UF membrane. As shown in Figure 3-9(a), the open-ended VA CNT membrane showed water permeability that was about three times faster (1,100 ± 130 LMH/bar) than the commercial UF membrane (477 ± 60 LMH/bar) despite of its smaller pore diameter (4.8 nm < 5.7 nm), lower pore density (6.8×10^{10} #/cm^2 < 8.8×10^{10} #/cm^2), and thickness that was approximately 2,000 times larger. The enhancement factor (ε) of the open-ended VA CNT membrane shown in Figure 3-9(a) was significantly higher (69,039 ± 8,122) than that of the UF membrane (5.8 ± 0.4). Note that the enhancement factor (ε) indicates the ratio of increased water permeability compared to the water permeability in a conventional no-slip condition. This high enhancement factor on the open-ended VA CNT membrane is comparable with previous studies. For example, the enhancement factor of Holt group's VA CNT membrane is 3,007 ± 1,695, possibly due to the smaller pore size (1.6 nm) [48]. Moreover, Hinds group's VA CNT membrane had an enhancement factor of 61,403 ± 16,663 due to the slightly lower pore density (3.4×10^9 #/cm^2) [46, 47].

Interestingly, the thickness of the active layer on both membranes had an important role on the conventional no-slip flow as calculated by Eq. 3-2. For

example, the UF membrane showed a similar water permeability between the experimental result and theoretical calculation due to the UF membrane's significantly thin active layer (0.1 μm) used for calculating the no-slip Hagen-Poiseuille equation as usual. On the other hand, since the open-ended VA CNT membrane had no active layer, approximately 2,000 times larger thickness (200 μm) was used. This difference in the open-ended VA CNT membrane resulted in a water permeability approximately 70,000 times faster than the water permeability in a conventional no-slip condition.

Figure 3-9(b) shows the normalized flux with applied pressure. As shown in Figure 3-9(b), the slope of open-ended VA CNT membrane was slightly decreased exceeding 6 bar, while the slope of UF membrane remained linear. Figure 3-9(c) shows water flux with viscosity ($Q \cdot \varepsilon$) with temperature. The slope of open-ended VA CNT membrane was decreased with increasing temperature, while the slope of UF membrane remained relatively constant. These results indicate that the open-ended VA CNT membrane had different trend with applied pressure and temperature. Possible explanations are that increasing entropy of water molecules with increasing temperature might disrupt the transport through CNT or that the thermal expansion of the epoxy matrix might decrease the flux by partially covering the CNT pores.

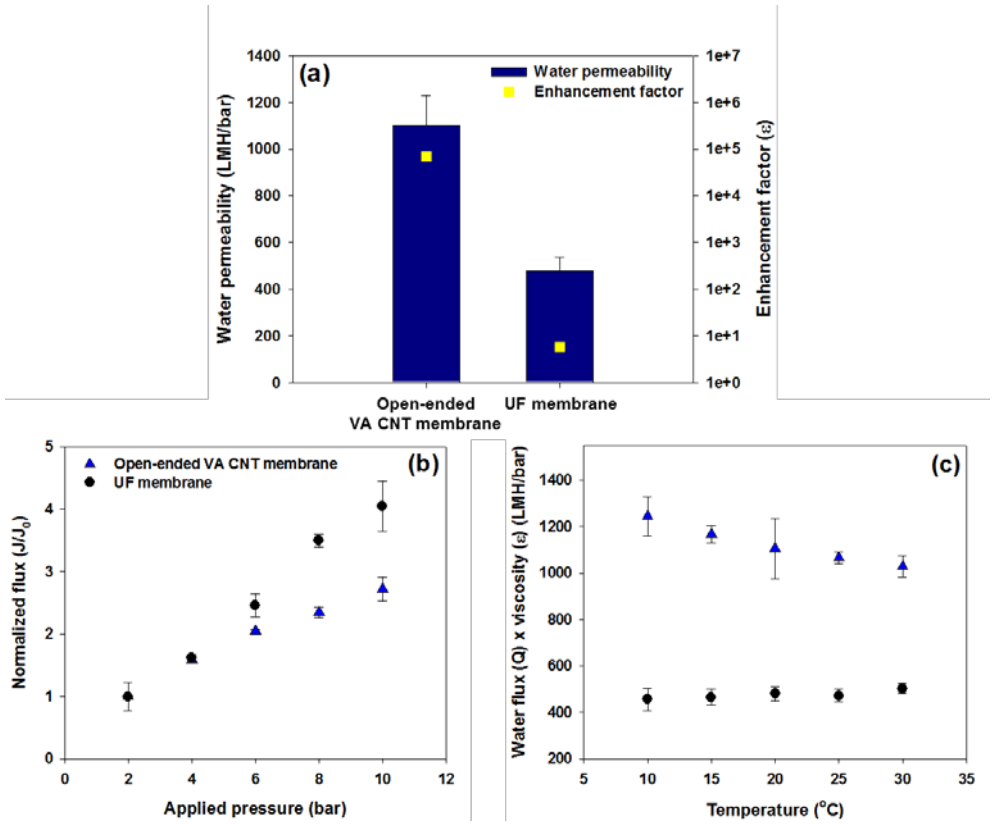

Figure 3-9. Water permeability properties of the open-ended VA CNT membrane compared to the UF membrane; (a) water permeability and enhancement factor (ε), (b) normalized water flux with applied pressure and (c) water flux with viscosity on various temperature.

Figure 3-10 illustrates the relationship between the enhancement factor of the open-ended VA CNT membrane and the solvent properties expressed as (a) solubility parameter and (b) viscosity. As shown in Figure 3-10(a), the enhancement factor of the open-ended VA CNT membrane increased with increasing solvent hydrophilicity, although not proportionally. Water, which has the highest solubility parameter (45.0 $MPa^{0.5}$), showed the highest enhancement factor (69,039) as well as the longest slip length (41.4 μm, not included in figure). Other solvents that had similar solubility parameter ranges (13.2 – 14.9 $MPa^{0.5}$) showed comparable enhancement factors where the slip length ranged 2.4 μm to 9.6 μm.

On the other hand, Figure 3-10(b) shows that except for water, the open-ended VA CNT membrane enhancement factor is inversely related to solvent viscosity. The decreasing tendency of the enhancement factors was observed (17,043 (hexane) > 15,460 (octane) > 12,004 (decane) > 4,303 (dodecane)) with increased viscosity of solvents (0.3 cP (hexane) < 0.5 cP (octane) < 0.9 cP (decane) < 1.5 cP (dodecane)). This observation is consistent with the conventional no-slip flow (Eq. 2). However, water did not follow this trend as it showed the highest enhancement factor regardless of its viscosity (1.0 cP). The results of Figure 3-10 demonstrate that solvent hydrophilicity acts as important role in permeability behavior on the open-ended VA CNT membrane.

Fast water permeability is explained by that hydrophilic water can quickly

pass through the hydrophobic CNT's inner wall due to the hydrophobic-hydrophobic interaction [90]. This phenomenon, nanofluidics on internal CNTs, was previously demonstrated by many researchers [44, 57, 91-93]. For example, low interfacial force between hydrophilic water molecules and smooth, hydrophobic CNT's inner walls contributes to fast water transport through the internal CNTs. Additional explanation is possible that water molecules spontaneously flow into the internal CNTs by forming a one-dimensional chain in hydrogen bonding due to its higher thermodynamical stability within CNTs [94, 95]. Likewise, high interfacial force between hydrophobic solvents (i.e. hexane, octane, decane and dodecane) and hydrophobic CNT's inner walls results in relatively slow flow in this study.

In addition, the PEO rejection of the open-ended VA CNT membrane as examined by MWCO measurement was 78% which was similar to that of the commercial UF membrane (82%). This result indicates that the open-ended VA CNT membrane with similar rejection rate showed about three times higher water flux than the UF membrane in virtue of fast water permeability through hydrophobic CNT's inner walls.

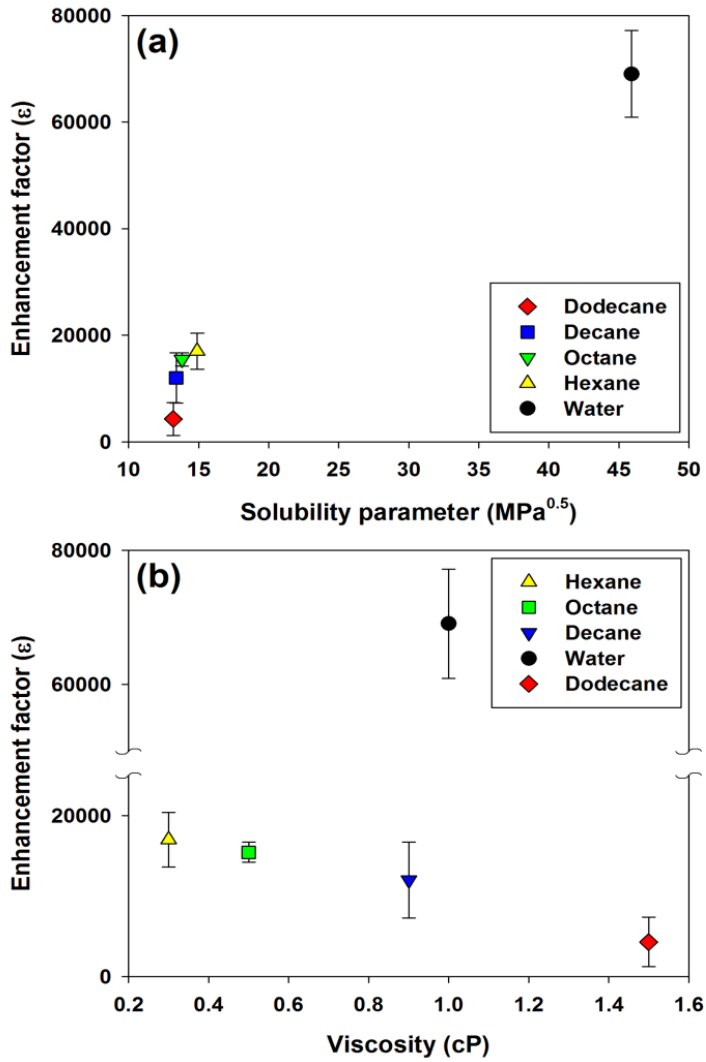

Figure 3-10. The relationship between enhancement factor (ε) of various solvents with (a) solubility parameter and (b) viscosity.

3.2.3. Membrane biofouling tendency

Figure 3-11 shows the permeate flux reduction of the open-ended VA CNT membrane on biofouling occurrence as it was operated for 600 min in a lab-scale cross-flow system under an identical permeate flux as the UF membrane. Note that no bacteria was observed in both permeates of the open-ended VA CNT membrane and the UF membrane. As shown in the control experiment in Figure 3-11, more flux decrease was observed on the open-ended VA CNT membrane (67%) than the UF membrane (55%). This result was expected, considering that the previous report showed that the more hydrophobic and rougher the membrane surface, the more membrane fouling [11]. Note that the open-ended VA CNT membrane appears to be more hydrophobic and rougher than the UF membrane (Table 3-3). However, in contrast to the results of the control experiment, the biofouling occurrence on the open-ended VA CNT membrane in Figure 3-11 did not follow this expectation. The decrease of permeate flux in the open-ended VA CNT membrane (74%) was less severe than that in the UF membrane (89%). In addition, 2 log less bacterial concentration was observed on the open-ended VA CNT membrane surface (4×10^5 CFU/mL) than the UF membrane surface (8×10^7 CFU/mL). One explanation for this phenomenon can be found in the antimicrobial property of CNTs. Accordingly, less biofouling tended to occur on the open-ended VA CNT membrane since bacteria might be inactivated by physical damage and/or oxidative stress from CNTs [74, 96, 97],

then detached from the open-ended VA CNT membrane surface.

Figure 3-12 describes CLSM images of the (a) open-ended VA CNT membrane surfaces and compared to that of the (b) UF membrane surface after biofouling occurrence for 600 min. As shown in Figure 3-12, it was clear that less bacteria were attached on the open-ended VA CNT membrane surface as compared to the UF membrane surface (green color: live cells, red color: dead cells), showing that biofilm thickness of both the VA CNT membrane and the UF membrane were 13 μm and 33 μm, respectively.

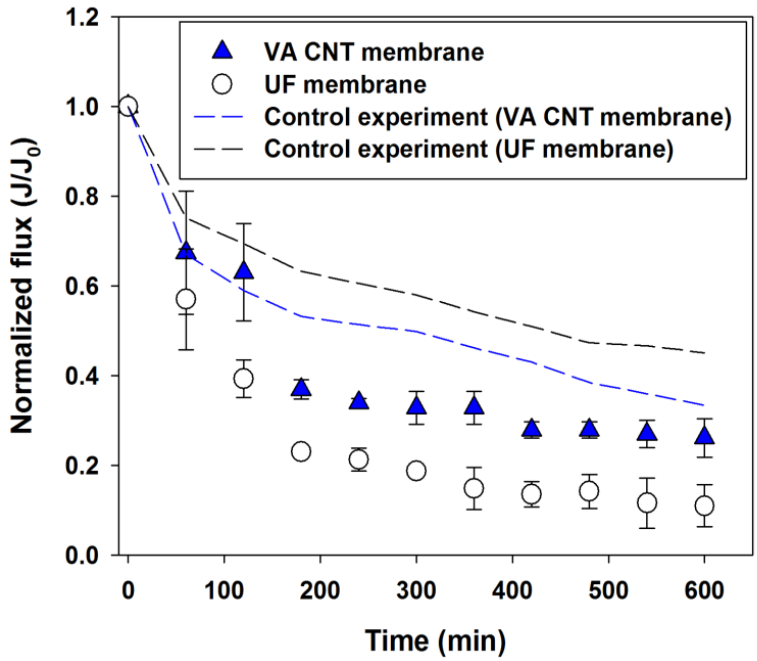

Figure 3-11. Normalized permeate flux reduction of the open-ended VA CNT membrane resulting from biofouling occurrence compared to that of the UF membrane as biofouling occurrence was carried out for 600 min in a lab-scale cross-flow system (feed solution: 10 mM NaCl, 10 mM sodium citrate, 0.1% tryptic soy broth and approximately 1×10^7 CFU/mL of initial *P. aeruginosa* PA01 GFP concentration, J_0: 700 LMH/bar, cross-flow velocity: 100 mL/min, effective membrane area: 0.8×0.8 cm^2, channel height: 0.1 cm, temperature: 25°C, control experiment was performed with only feed solution (no bacteria)).

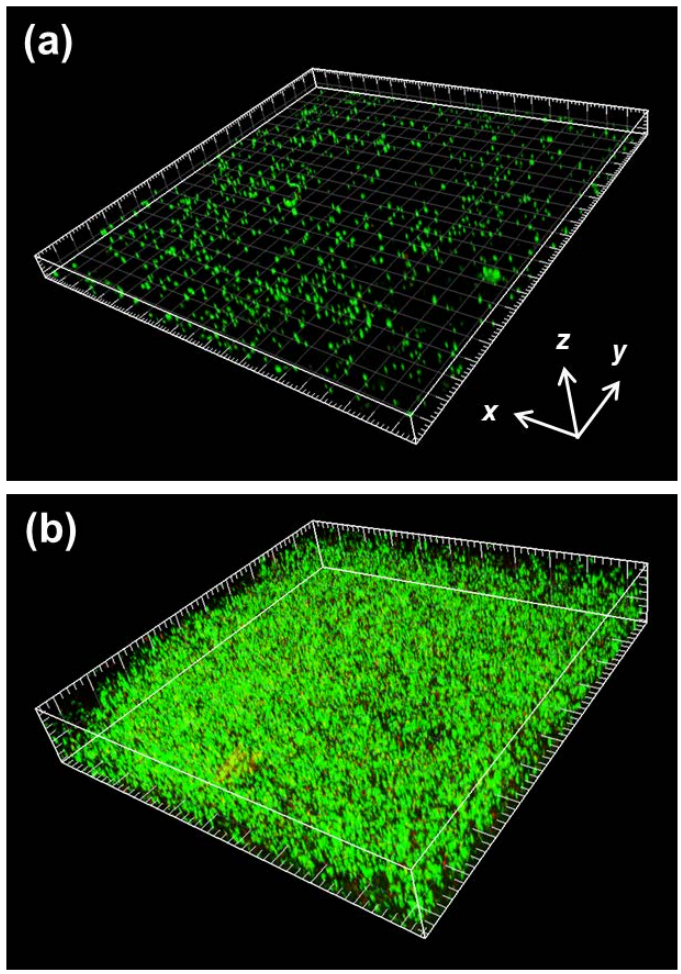

Figure 3-12. CLSM images after biofouling occurrence for 600 min on the (a) open-ended VA CNT membrane and (b) UF membrane (green: live cells, red: dead cells; *x* axis: 202 μm, *y* axis: 202 μm; *z* axis: (a) 13 μm, (b) 33 μm).

3.3. Conclusion

This study fabricated the open-ended VA CNT membrane and evaluated its performance to investigate an application for water purification. The open-ended VA CNT membrane showed better permeability performance, showing about three times higher than the commercial UF membrane. This flow behavior is approximately 70,000 times faster than the conventional flow under the no-slip condition. Also, the enhancement factor of the open-ended VA CNT membrane was increased with increasing solvent hydrophilicity, although not proportionally. The most hydrophilic solvent water has the highest enhancement factor among the solvents examined, while the enhancement factors are inversely related to solvent viscosity than the conventional flow excluding water. Moreover, the rejection property of the open-ended VA CNT membrane as examined by MWCO measurement was similar to the commercial UF membrane. Finally, open-ended VA CNT membrane showed a better biofouling resistance, represented by approximately 15% less permeate flux reduction and 2 log of less bacterial attachment than UF membrane. This study suggests that the open-ended VA CNT membrane with high performance and antifouling properties is feasible for water purification where UF membrane is required, although practical application of the open-ended VA CNT membrane is somewhat limited at present due to the cost of its fabrication, optimized filler, the enlargement of open-ended VA CNT membrane and its stability test.

4. Dense-array Outer-wall Carbon Nanotube Membrane

4.1. Materials & Methods

4.1.1. Materials

Si wafer for CNT growth, epoxy resin for the fabrication of VA CNT membranes, and polysulfone UE4040 membrane as a commercial UF membrane are used same as Chapter 3. Commercial PTFE membrane (Millipore Fluorepore TM membrane filter, average pore diameter: 3 μm) was used support layer for the dense-array outer-wall CNT membrane.

Deionized water (Barnsted NANO Pure, USA) was used for water permeability measurements. Seven kinds of dextran (molecular weight: 5 kDa – 670 kDa, Sigma Aldrich, U.S.A.) were used for the rejection test. For the biofouling occurrence, *Pseudomonas aeruginosa* PAO1 GFP (Center for Biofilm Engineering, Montana State University) was used as a model bacterial strain with the 0.1% tryptic soy broth (Bacto, Franklin Lakes, U.S.A) solution as a nutrient.

4.1.2. CNT synthesis and characterization

Vertically aligned CNT was synthesized by water assisted CVD in a horizontal quartz tube furnace with an inner diameter of 4 inch. Layers of 1 nm thick Fe and 20 nm thick Al were deposited on silicon (Si) substrate using e-beam evaporator and sputter. The substrate area (A_0) for the open-ended CNT membrane, and those for D_f of 1, 3, 6 and 10, respectively, were 0.5 × 0.5, 1 × 1, 1.8 × 1.8, 2.5 × 2.5 and 3.2 × 3.2 cm^2. The CNTs were grown in quartz tube at 810°C (at ramp rate of 810°C/min) for 16 min with C_2H_2 (210 sccm) as carbon source, Ar (480 sccm) as carrier gas and H_2O vapor generated by bubbling water at 60°C with Ar flow (222 sccm) as growth enhancer. All gases were simultaneously introduced into the tube at the beginning of the growth process.

The CNT separated from the substrate was weighed by satorious BT 224S balance. The microstructure of the CNT was characterized by scanning electron microscope (SEM) images, taken with a Carl Zeiss SUPRA 55VP FE-SEM at an acceleration voltage of 15 kV, tortuosity of the CNT was measured with SEM image magnified by a factor of 500,000. Inner structure, inner diameter and wall number of the CNT were statistically measured from transmission electron microscope (TEM) images by a JEOL JEM-3000F high-resolution transmission electron microscope at an acceleration voltage of 300 kV. For the CNT purity measurements, Raman spectra were obtained on a confocal laser micro Raman spectrometer with a 532 nm laser source (LabRam 300, JY-Horiba) and × 100

objective lens. The average pore size of the outer-wall CNT membrane was determined by the Barrett-Joyner-Halenda (BJH) method at 77K using micromeritics ASAP 2010. TGA measurements (thermogravimeteric analysis, setsys 16/18) were performed (20 – 800°C) with heating rate of 5°C/min. Functionalization at CNT tip was analyzed by deconvolution of C 1s spectrum obtained by XPS (PHI 5000 versaProbe II; Al Kα source)

The areal density of the CNT(#/cm^2) was calculated with the geometric shape taken into consideration [98]. It is assumed the mass of the CNT of unit length linearly increases according to wall number:

$$\rho_n = \frac{\rho_m}{m_u N} = \left(\frac{3\sqrt{3}a_{c-c}^2}{4\pi m_c N}\right) \cdot \left(\frac{\rho_m}{d_{outer}}\right) \quad \text{(Eq. 4-1)}$$

where ρ_n, ρ_m, m_u, N, $a_{c\text{-}c}$, m_c, and d_{outer} ,respectively, are the areal density(#/cm^2) of the CNT, the mass density (mg/cm^3) of the CNT, the mass of the CNT of unit length, the average wall number, the C-C bond length in a nanotube(1.44 Å), the mass of one carbon atom(1.993×10^{-26} kg), and the outer-wall diameter. Mass density of the CNT is defined in Eq. 4-2 as follows:

$$\rho_m = \frac{\Delta M}{SL} \quad \text{(Eq. 4-2)}$$

where ΔM, S, and L are the mass of the CNT (mg), the CNT growth area (cm^2), and the CNT height (cm), respectively.

4.1.3. Fabrication of dense-array outer-wall CNT membrane

Vertically aligned CNT was separated from the substrate. The CNTs were compressed by applying mechanical force in the direction perpendicular to the CNT axis (mechanical densification, refer to Figure 4-1 and Figure 4-2). The mechanically densified CNT was positioned on the commercial PTFE membrane treated with ethanol. The CNT array on the PTFE membrane was surrounded by semi-curing high-viscous epoxy to clamp the CNT array under high test pressure and prevent test fluids from leaking through the side of the CNT array. The CNT array surrounded by the epoxy was then cured at room temperature for 24 h. The gel-like high-viscosity epoxy was obtained by curing the low-viscosity epoxy at room temperature for 24 h. Therefore, the epoxy did not permeate into interstitial space between the CNTs (= effective pore of outer-wall CNT). Full curing of the epoxy took 48 h. The resultant membrane is the outer-wall CNT membrane used in experiment. After outer-wall CNT membrane was fabricated, the outer-wall membrane was dipped into water and then the outer-wall pores (interstitial space between CNTs) were filled with water in vacuum. Permeability of the water-absorbed outer-membrane was measured by dead-end filtration system as shown in Figure 4-3.

The outer-wall CNT membrane with thermal purification was cap-opened by RIE etcher (Oxford instrument, RIE 80 plus) equipped with radio-frequency (RF) power. RF power was set at 50 W. Work pressure was about 0.1Torr in the

chamber. During the RIE process, the flow rate of oxygen was set at 60 sccm and the duration of etching time was 20s.

The pore area (A_{pore}) in the membranes was calculated as follows:

$$A_{CNT} = \frac{\pi d_{outer}^2}{4} \times \rho_n \quad \text{(Eq. 4-3)}$$

$$A_{pore} = A_{total} - A_{CNT} \quad \text{(Eq. 4-4)}$$

where A_{CNT}, d_{outer}, ρ_n, A_{total} are the area occupied by CNTs in the membrane (cm^2), the outer diameter of CNT, the areal density of CNT (by Eq. (1)) (#/cm^2), and total area (cm^2) of the membrane that includes both CNT and pore area (cm^2), repectively.

The adsorption of nitrogen in mesopores has been interpreted in terms of the capillary condensation theory given by the Kelvin equation [99]. The Kelvin equation establishes a relationship between the cylindrical pore size and the condensation relative pressure as follows [99]:

$$\ln \frac{p}{p_0} = -\frac{2\sigma V_m}{RT} \frac{1}{(r-t)} \quad \text{(Eq. 4-5)}$$

where σ is the surface tension of liquid adsorbate, V_m is the molar volume of nitrogen at the measurement temperature and r is the pore radius and t is the film thickness of adsorbate, R and T are the gas constant and absolute temperature, respectively.

For the pore size measurement, 20 mg of as-grown or densified VA CNT arrays were used for adsorption in BJH instrument of ASAP 2010 (micromeritics, USA) system. Prior to each adsorption experiment, the sample was outgassed in vacuum at 473 K for about 2 h. Nitrogen adsorption/desorption measurements were performed at 77 K. The software in the instrument prints out information on average pore size, which is the pore size listed in the table, and pore volumes and pore areas corresponding to different pore sizes after the experiment is completed. Falconer et al.[100] and Futaba et al.[101] reported interstitial pore size between CNTs, BET surface area, mesopores surface area, pore volume and micropore volume etc. of VA CNT array with N_2 adsorption/desorption.

The slip length was calculated with indirect method [102]. The following equation was used:

$$\frac{Q(\lambda)}{Q_{NS}} = 1 + \frac{4\lambda}{a} \qquad \text{(Eq. 4-6)}$$

where $Q(\lambda)$ and Q_{NS} are the flow rates with slip and no-slip boundary condition, respectively, λ is the slip length, and a is the pore radius. $Q(\lambda)$ is matched with the experimentally observed flow rate in choosing the slip length. We used the pore radius determined by BJH method for the radius a. Q_{NS} is calculated by Hagen-Poiseuille equation [$Q_{HP}=(\pi d4\Delta p)/(128\eta L)$] from Stokes Eq.

Seven types of dextran were used for rejection test of CNT wall membrane. Dextrans, neutral slightly-branched polymers of D glucopytanose, were used as model compounds. 100 mg/L of dextran solution was prepared in 0.15 M NaCl

solution which had been prefiltered through 0.2 um AAO membrane (Anodisc, Whatman Co., USA). Dextran rejection tests were performed with a modified dead-end filtration system (Figure 4-3). To minimize concentration polarization on the CNT membranes, each CNT membranes were immersed in the dextran solutions for 6 h. The permeabilities of dextran solutions were describes in Table 4-1. Permeates were collected for gel permeation chromatography (GPC, Breeze system, Water, USA) analysis after the stabilization for 30 min. Also, the permeabilities of DI water were measured before and after the rejection tests to verify that there were no irreversible changes in permeabilities due to dextran fouling. 0.02 N $NaNO_3$ was used as the eluents for the dextran solutions and the eluent flow rate was fixed at 0.8 mL/min at 30°C. Each retention time for various dextran molecular weights was obtained as a standard. Dextran rejections of the membranes were determined as a function of molecular weight by fitting the chromatograms for the individual, narrow molecular weight dextran fractions to the curves for the feed and permeate samples and utilizing calibration data relating peak areas to the concentrations of the dextran fractions in the sample.

Pore size of outer-wall VA CNT membrane was estimated by fitting to the hindered pore-flow solute transport model. This method is commonly used to determine molecular weight cut-off (MWCO) of the membrane for water treatment [103-105] The Stokes radius of a dextran can be obtained by its diffusivity from Stokes-Einstein Eq.:

$$D_{AB} = \frac{kT}{6\pi\eta a} \qquad \text{(Eq. 4-7)}$$

where D_{AB} is the diffusivity, k is Boltzmann's constant, η is the solvent viscosity and a is the Stokes radius.

The Stokes radii of dextran molecules can be obtained from their molecular weight with empirical Eqs. ($a=0.488 \times M^{0.437}$) [106]. From the results of rejection rate, pore size was calculated by Ferry-Renkin Eq. Note that >90% rejection was used for pore size estimation because typical method for molecular weight cut-off (MWCO) measurement is calculated by the 90% rejection of dextran solute [107-109].

$$R = \{1 - 2(1 - \frac{a}{r})^2 + \left(1 - \frac{a}{r}\right)^4\} \times 100\% \qquad \text{(Eq. 4-8)}$$

where R is the rejection rate, a is the radius of solute and r is the radius of pore.

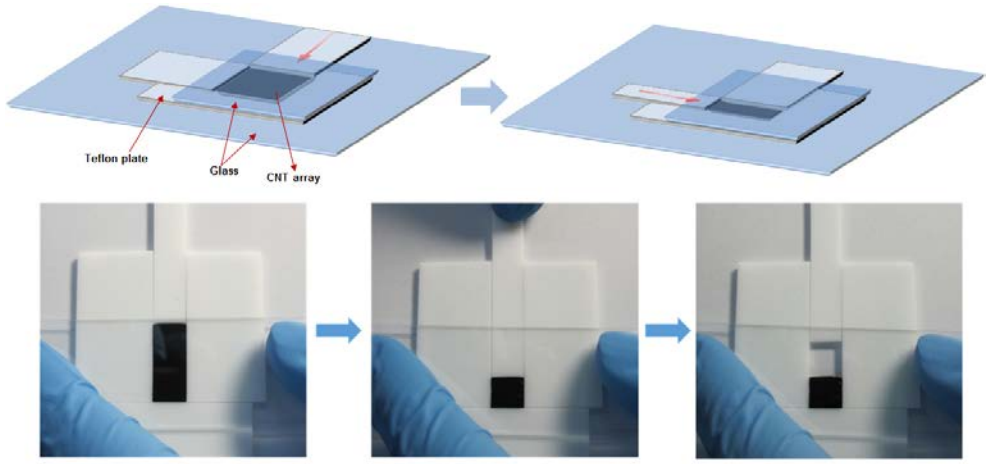

Figure 4-1. Schematics for mechanical densification of the CNT array. Evenly press all sides of the CNT array in reducing to desired area.

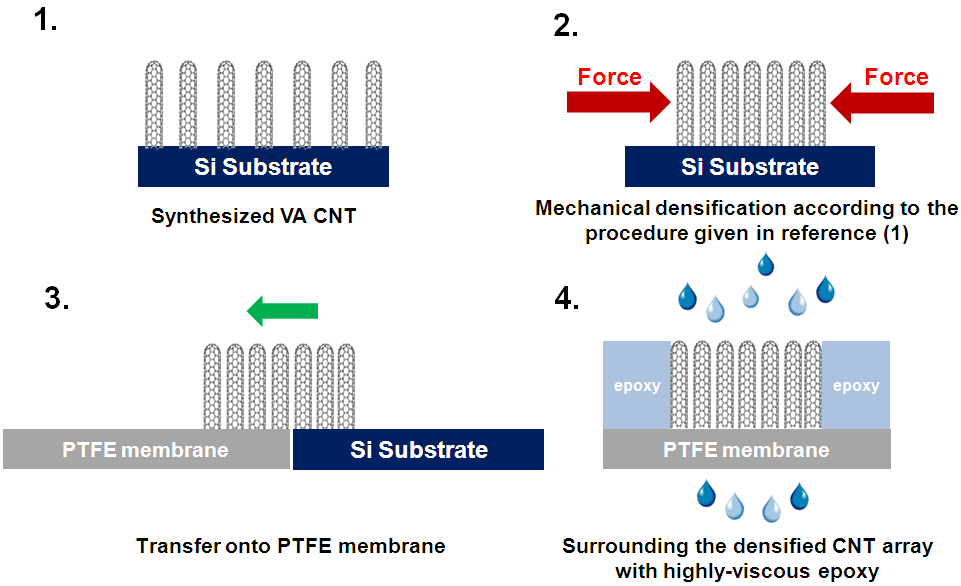

Figure 4-2. Schematics for dense-array outer-wall CNT membrane fabrication. Step 1: Vertically aligned CNT growth on silicon substrate (chemical vapor deposition). Step 2: Mechanical densification according to the procedure given in reference (1). Step 3: Transfer of densified CNT onto PTFE membrane (average pore size: 3 μm) from the substrate. Step 4: Surrounding the periphery of the densified CNT array with highly-viscous epoxy (The epoxy does not permeate into the space between the densified CNT and PTFE membrane because of very high viscosity).

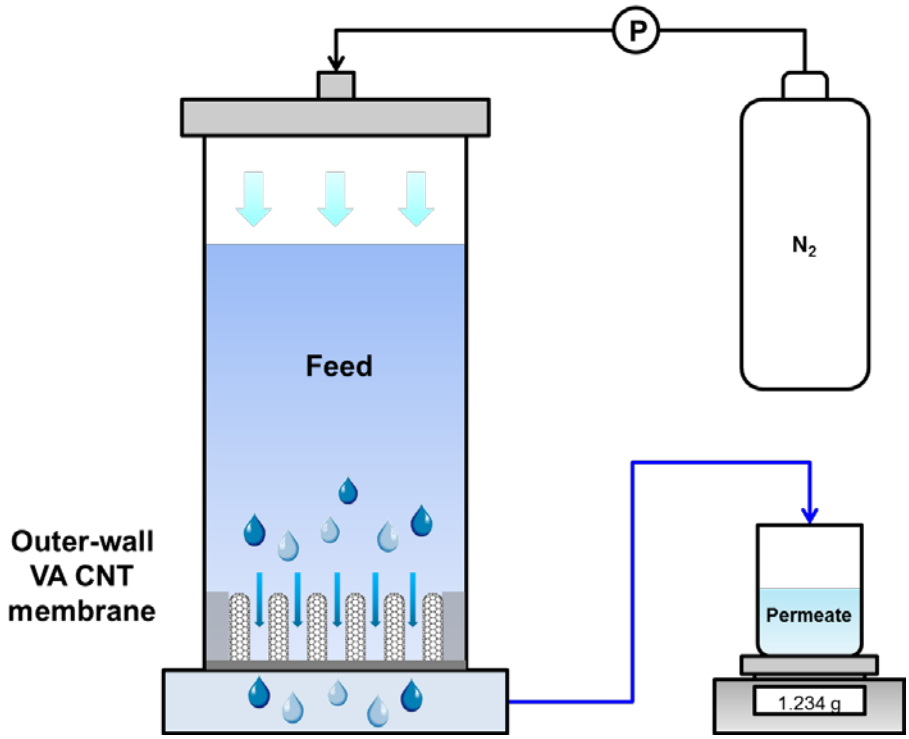

Figure 4-3. Schematic of dead-end membrane filtration system. Water permeability and rejection tests were performed with N_2 gas at 1 bar. Permeate was collected and weighed. Water permeability was calculated from the information on permeate volume (mL), time (5 min) and total membrane area (~1 cm^2).

Table 4-1. Permeability of dextran solution (100 mg/L) and DI water of dense-array outer-wall CNT membranes.

(LMH/bar)	D_f 1	D_f 3	D_f 6	D_f 10	D_f 10 thermal	D_f 10 thermal + plasma	Commercial UF
DI water	5848.9	4798.5	4112.2	6302.5	14073.3	31942.4	282.9
100 mg/L dextran solution	4798.5	4044.1	1260.5	880.9	2416.0	24583.5	78.8

4.1.4. Anti-microbial tests

The outer-wall CNT membrane (D_f 10), the CNT wall membrane and the commercial PSf UF membrane were immersed into the feed solution with *P. aeruginosa* PAO1 GFP in six well plates with 50 rpm of stirring at 25°C for 72 h. The feed solution was replaced with 10 mL of 1/300 TSB solution every 24 h. Each sample was taken out at 24 h, 48 h and 72 h and then stained with a BacLight Live/Dead Bacterial viability kit (Molecular Probes, USA). After the staining, the bacterial adhesion and the biofilm formation were observed by confocal laser scanning microscopy (CLSM; Eclipse 90i, Nikon, Japan) [88].

4.2. Results and Discussion

4.2.1. Densified CNT array and outer-wall CNT membrane

Vertically grown CNT forest and densified CNTs that can be used as outer-wall membranes are shown in Figure 4-4(a) and 4-4(b), respectively. The vertical CNTs were super-grown by water assisted chemical vapor deposition (CVD), which extends catalyst lifetime with the use of moderate oxidant, and yields high-density and high-aspect ratio CNTs (length/CNT inner diameter) [79]. The CNT forest in Fig. 4-4(a) is 1.3 mm high and vertically aligned on silicon substrate (Figure 4-5(a)). A 'skin layer' covering the surface which can block the fluid flow is not observed from the image of top surface of CNT forest (Figure 4-5(b)). Average inner diameter and wall number of the CNT, statistically measured from high-resolution tunneling electron microscopy (HR-TEM) images, were 4.8 nm and 2.7, respectively, and they were generally Gaussian-distributed (Figure 4-6) with aspect ratio of 2.7×10^{5} (length (1.3 mm)/inner diameter (4.8×10^{-6} mm)). As shown in HR-TEM images (Figure 4-7), the vertical CNT has bamboo-free structure without the inner wall crossing the inner space of the CNT, and there are no catalyst nanoparticles blocking the inner space [110]. The as-grown vertical CNTs are, on the average, approximately several tens of nanometers apart from one another and thus the interstices created by the vertical CNTs can be utilized as membrane pores, i.e., outer-wall CNT membrane.

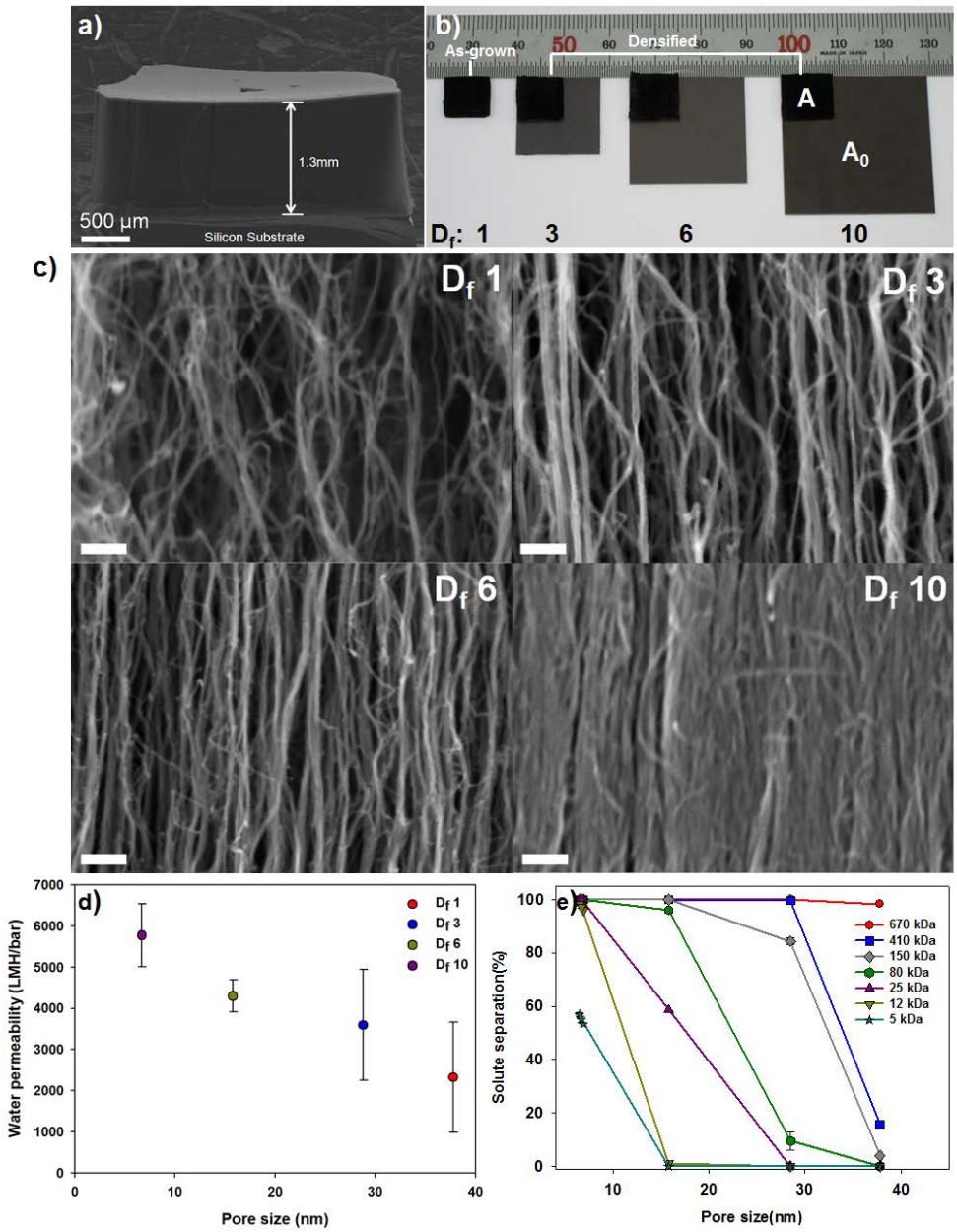

Figure 4-4. Densified CNT array and performance of outer-wall membrane. a) SEM image of super-grown CNT forest. (b) optical photographs of densified CNT

arrays that were used as outer-wall CNT membranes. Densification factor (D_f) is the ratio of CNT area before densification to that after densification. The area A is the same at 1 cm^2 for all cases whereas the area occupied by as-grown CNT (A_0) varies depending on D_f value. In the case of D_f of 10, 10 cm^2 of as-grown CNTs are densified into 1 cm^2 of compressed CNTs. c) cross-sectional SEM images (× 300,000 magnification, scale bar:100nm) of densified CNT. The higher the D_f was, the more closely packed and the more straightened the CNT was. The figures give the fracture plane images of the CNT array. The large pore in the image would correspond to the area where a bundle of CNTs was pulled out in the course of fracturing. d) water permeability as affected by densification factor D_f for outer-wall CNT membrane. e) rate of rejection by densified outer-wall CNT membranes obtained with seven kinds of dextran (5 kDa – 670 kDa). 100 mg/L of dextran solutions were filtered by the densified outer-wall CNT membrane under 1 bar of pressure at 20°C.

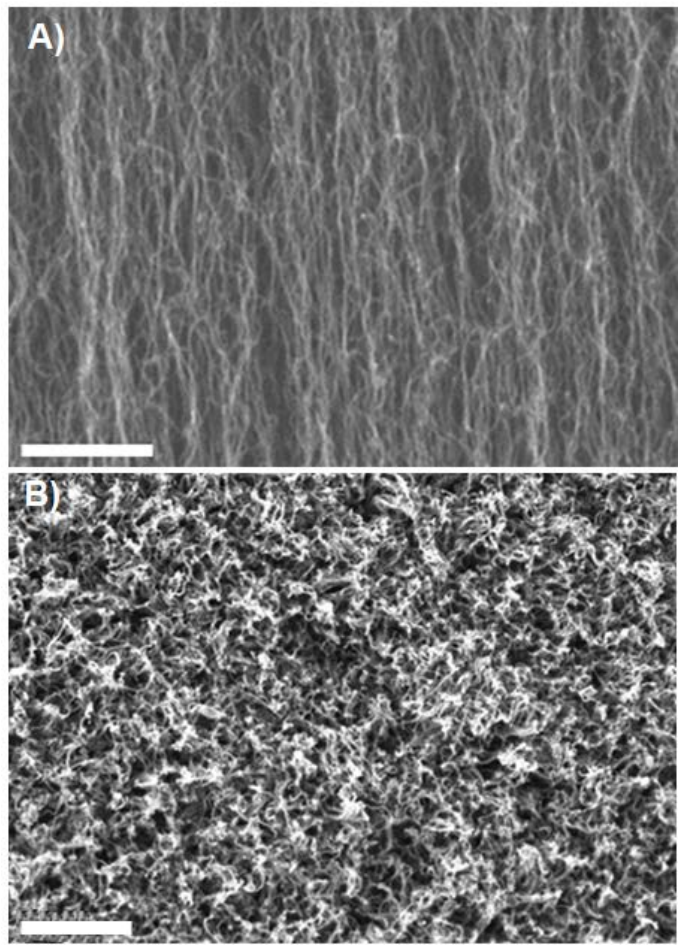

Figure 4-5. SEM image of the carbon nanotube (CNT) forest. A) cross-section (scale bar: 500 nm) and B) top surface (scale bar: 500 nm).

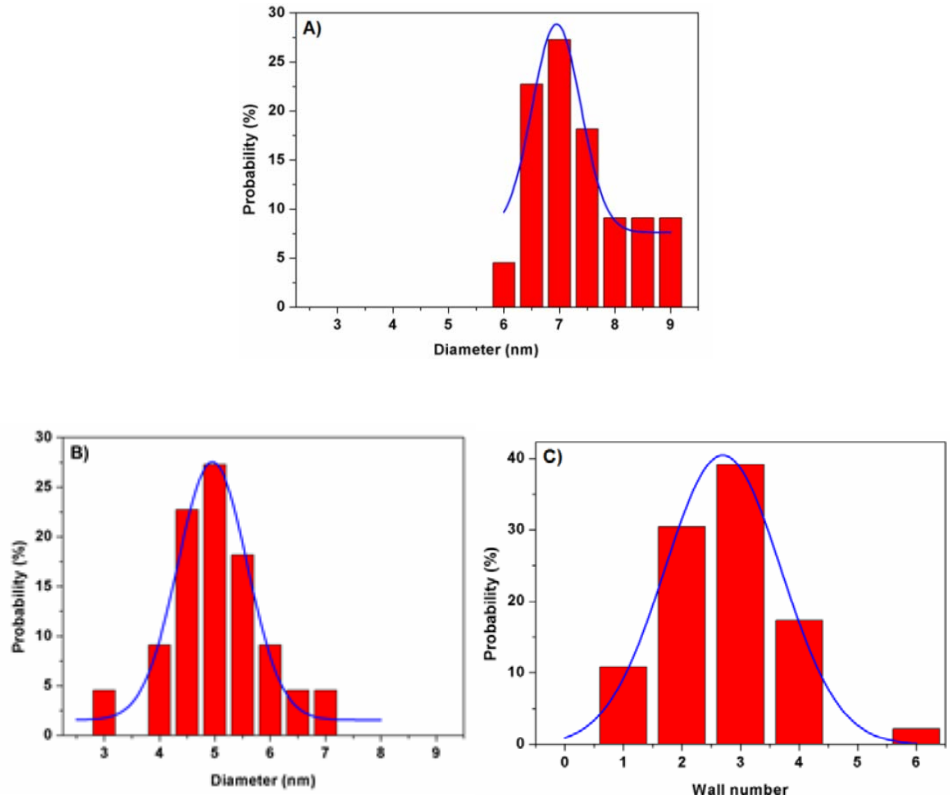

Figure 4-6. Diameter and wall number distributions of CNT: A) outer diameter, B) inner diameter, and C) wall number distribution. Average outer diameter, inner diameter, and wall number of the CNT, respectively, are 7.1 nm, 4.8 nm, and 2.7. The distributions were obtained from high-resolution tunneling electron microscopy (HR-TEM) measurements of 100 individual CNTs, which generally are Gaussian-distributed (measured by Gatan Digital Micrograph program with the HR TEM images)

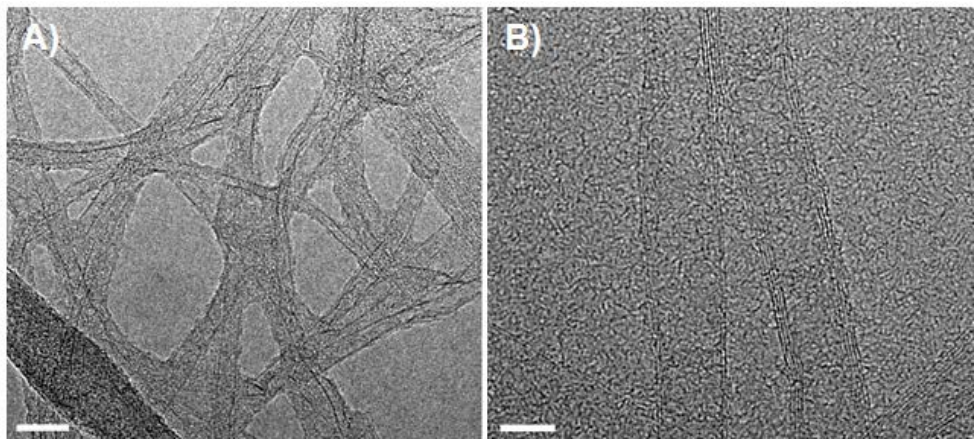

Figure 4-7. HR-TEM images of the carbon nanotubes: A) and B) CNTs have bamboo-free structure with no catalysts in inner space. Therefore, the inner space of the CNT is a nanochannel for water molecules (scale bar: A) 40 nm and B) 5 nm).

The characteristics of pore structure of the outer-wall CNT membrane, such as pore dimension, pore density, and pore tortuosity, can be altered and manipulated for better membrane performance or for extensive applications by mechanical densification method [111]. Figure 4-4(b) shows optical images of densified CNT arrays (outer-wall CNT membranes) that were obtained by compressing the CNTs on the gray area to a lateral area of 1 cm^2 (black rectangular area in the figure). We define densification factor D_f as the ratio of area occupied by CNTs before compression or as-grown CNTs (A_0) to that occupied by compressed CNTs after densification (A) such that a D_f (A_0/A) value of 10 signifies a tenfold densification of the as-grown CNTs. Three densified outer-wall CNT membranes corresponding to D_f of 3, 6, and 10 (Figure 4-4(b)) and one as-grown outer-wall CNT membrane (D_f 1) were used in experiment. The cross-sectional scanning electron microscopy (SEM) images in Figure 4-4(c) show that the larger the densification factor is, the higher the density of CNTs becomes. The size of the interstitial space between neighboring CNTs, which is an average pore size in the outer-wall CNT membrane, was measured by Barrett-Joyner-Halenda (BJH) method [112-114] (Figure 4-8) and estimated by theoretical calculation [98] and pore-flow solute transport model with dextran. Falconer et al.[100] and Futaba et al.[101] reported values of interstitial pore size between CNTs, BET surface area, mesopores surface area, pore volume and micropore volume of vertically-aligned CNT array with N_2 adsorption/desorption. Figure 4-9 shows N_2 sorption isotherms of outer-wall

membranes (D_f 1 – 10). These isotherms are of type II physisorption isotherms [99], which means that nitrogen physisorbs on CNT walls. The characteristics of the outer-wall CNT membrane are summarized in Table 4-2. Note in the table that the pore size can be controlled from several tens of nanometer that corresponds to the membrane with D_f of 1 to 7 nm that is for the membrane with D_f of 10, the pore size of which is close to the inner diameter of CNT (4.8 nm). It is also noted in the table that the pore density can be increased by an order of magnitude from 8.14×10^{10} #/cm^2 (D_f 1) to 83.3×10^{10} #/cm^2 (D_f 10) by mechanical densification. Another characteristic of interest for membrane is tortuosity of pores, which was statistically measured with high-magnification SEM images. The tortuosity (Γ) was calculated from L_e/L where L is the straight CNT length, and L_e is the curved length of CNT. It is apparent from the table that the tortuosity approaches unity as the densification factor increases, which indicates that the CNTs or the pores in the outer-wall membrane can be straightened by the densification.

These results demonstrate that the mechanical densification is a simple and yet effective way of manipulating and altering the membrane characteristics for desired membrane performance. The fabrication process for the outer-wall CNT membrane is illustrated in Figure 4-2. The outer-wall membrane is 1 cm^2 in area and 1.3 mm thick.

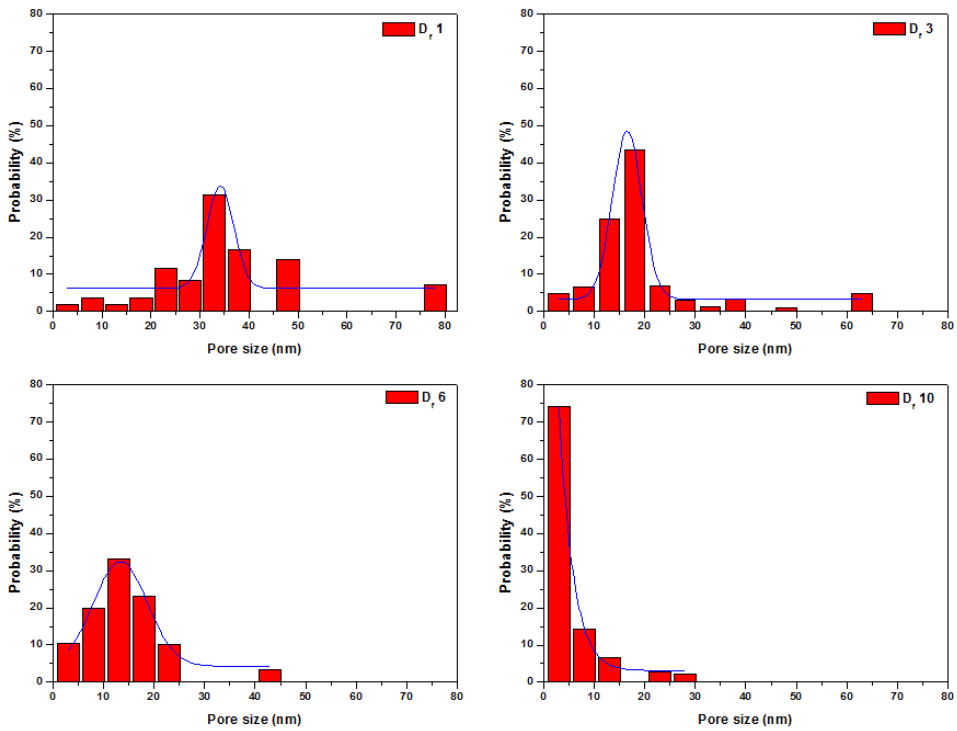

Figure 4-8. Pore size distributions of outer-wall membranes. The pore size distributions that can be obtained from the BJH data on pore areas and pore volumes corresponding to different pore sizes are given above. The pore size distribution becomes narrower with increasing densification.

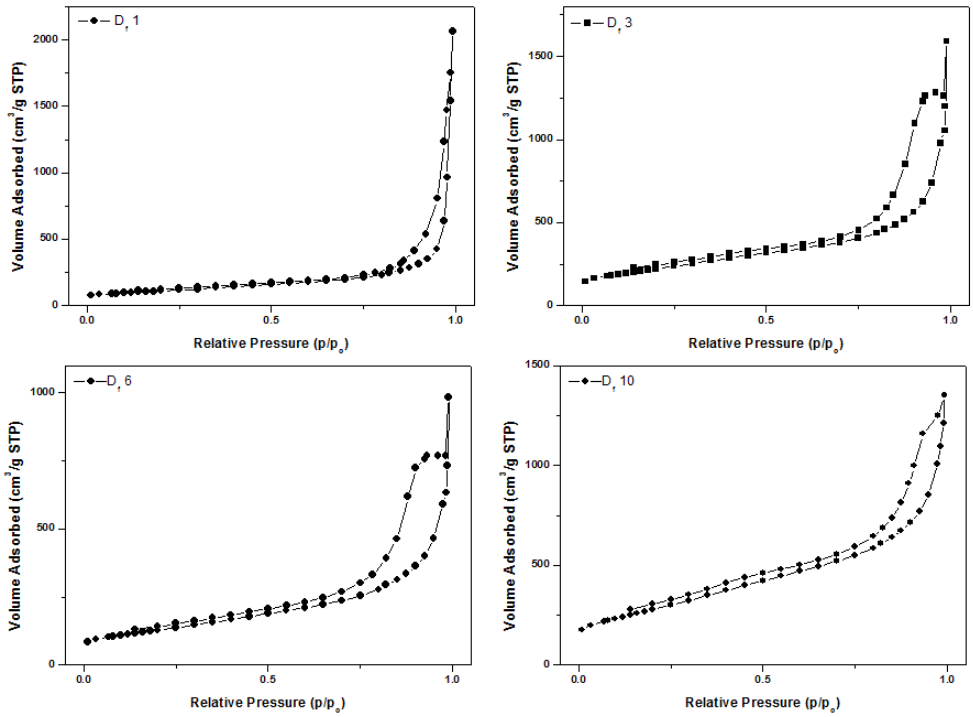

Figure 4-9. Sorption isotherms of outer-wall membranes. With regard to the gas interaction with CNT walls, it is noted that there are four different types of adsorption isotherms for physisorption. The adsorption isotherms shown above for outer-wall membrane is type II of physisorption isotherms [99], which means that nitrogen physisorbs on CNT walls.

It is well known that water permeability invariably decreases as the pore size of membrane is decreased to remove finer impurities. The fact that the outer-wall CNT membrane does not subscribe to the well-known behavior is revealed in the water permeability plotted in Fig. 4-4(d) that was determined by dead-end membrane filtration system (Figure 4-3). It is clear from the figure that the water permeability for the outer-wall CNT membrane rather increases with decreasing pore size or increasing densification of CNT array, increasing from 2,328 ± 1,333 LMH/bar for D_f of 1 (as-grown) to 5,774 ± 759 LMH/bar for D_f of 10, a more than twofold increase in the permeability due to the densification. As given in Table 4-2, the pore size of the membrane decreases with increasing densification, decreasing from 37.8 nm for D_f of 1 to 6.7 nm for D_f of 10. These experimental results, when taken together, clearly reveal the unique feature of the outer-wall membrane where a smaller membrane pore size leads to a larger water permeability, as shown in Fig. 4-4(d).

To verify the reason for the water permeability enhancement, we obtained independently determined pore area and calculated the flow velocity of water from experimentally obtained hourly volume of purified water. As shown in Table 4-2, the flow velocity increases with increasing densification, which is the reason for the increase in water permeability. It is well known that hydrophobic CNT walls leads to a frictionless flow and thus a high flow velocity due to weak interfacial force between water molecules and atomically smooth and

hydrophobic CNT wall [46-48]. Molecular ordering taking place in the inside of the tube was also proposed for the high flow velocity [90, 94, 115]. As the densification increases, more CNT wall surface becomes available for water flow and therefore higher velocity ensues.

For the unique feature of the outer-wall CNT membrane to be valuable, the ability of the membrane to reject finer impurities should still be retained as the pore size is decreased for higher water permeability. To demonstrae the ability, experiments were carried out for particle rejection behavior of the outer-wall membrane with dextran solutions (100 mg/L) of seven types of dextrans (5 kDa, 12 kDa, 25 kDa, 80 kDa, 150 kDa, 410 kDa, and 670 kDa) under 1 bar of pressure at 20°C. The rejection rate (R) was determined from $(C_f-C_p)/C_f \times 100$, where C_f and C_p are the feed concentration and the permeate concentration, respectively. Shown in Figure 4-4(e) are the rejection rates for various types of dextran solutions that were achieved by the outer-wall CNT membranes densified to various levels of D_f from 1 to 10. It is evident from the figure that a more densified membrane or membrane with a smaller pore size removes finer particles. This result clearly demonstrates experimentally that there is a membrane system for which a higher water permeability is achieved with a smaller pore size while retaining the ability to remove finer impurities, i.e., densified outer-wall CNT membrane system. In this regard, it is noted that the outer-wall CNT membranes with D_f 3, D_f 6, and D_f 10 all showed 100%

rejection of 670 kDa dextran, indicating that there were no micron-scale cracks. Ability of outer-wall memebranes with D_f 10 in particle rejection is comparable with that of commercial UF membrane (Table 4-3) though the outer-wall membrane is superior to that in water permeability.

There are some aspects of this CNT membrane that could be utilized for better membrane performance. For one, the CNT walls can be cleaned for higher water permeability. It is known that many amorphous carbon and defects are present on the outer-wall of CVD-grown CNT [116]. The Raman spectrum of as-grown CNT in Figure 4-10 indicates that the peak intensity ratio of G to D band (I_G/I_D) is relatively low at 0.93, indicating a high density of amorphous carbon and defects on the outer-wall. These amorphous carbon and defects could retard the flow, particularly for highly densified CNTs, due to a reduction in available area of smooth CNT surface that enhances the velocity. It is desirable, therefore, to remove the amorphous carbon to increase the velocity. For the purpose, a thermal treatment could be used, particularly in light of the fact that oxidation temperature of amorphous carbon is lower than that of sp^2 bonded carbon in oxygen atmosphere [117, 118]. To arrive at a systematic way of removing the carbon, thermogravimetric analyses (TGA) were carried out as shown in Figure 4-11. The figure shows that the weight loss is only 5% up to 600°C but then a precipitous loss occurs once it exceeds the temperature, reaching almost 100% loss at 720°C. To arrive at an optimal heating schedule, the heating time and the

final temperature were varied. The corresponding CNT purity was given by Raman peak intensity ratio of G to D (I_G/I_D) [119]. Heating to 500°C at the rate of 5°C /min (100 min) yielded the highest intensity ratio and therefore, this heat treatment was used to remove amorphous carbon in ambient air.

The water permeability through the outer-wall CNT membrane with D_f of 10 before and after the thermal purification of CNTs is shown in Figure 4-12 along with the water permeabilities reported in the literature for other CNT membranes [46, 48, 59, 100]. The water permeability of the outer-wall membrane is seen to have more than doubled as a result of the heat treatment due to the corresponding increase in water flow velocity (Table 4-2). To observe the effect of the smooth CNT surface by the thermal purification on the permeability enhancement, the thermally purified outer-wall membrane (D_f 10) was coated with a solution of 1-pyrenebutyric acid (PyBA) in methanol (10 mM) for hydrophilic CNT wall. The PyBA molecule is comprised of pyrene and carboxyl group and the pyrene group is non-covalently attached at the CNT wall [120]. The membrane was submerged into PyBA solution for 24 h and then rinsed with methanol and water. The water permeability of PyBA-treated membrane (I_D/I_G=1.00) was measured to be 5,378 LMH/bar, which is lower than that of the thermally-treated membrane (13,166 LMH/bar). The reduction in permeability could be attributed to hydrophilicity of CNT wall, which leads to an enhanced interaction between water molecules and the wall.

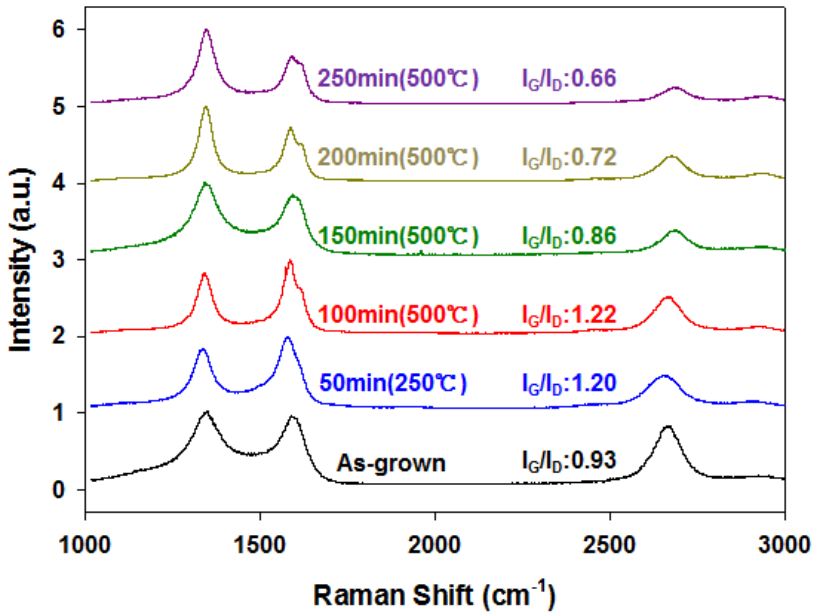

Figure 4-10. Raman spectrum of vertically aligned CNT as affected by heating condition. CNTs were heated to the final temperature shown in the figure at a constant heating rate such that a combination of 50 min and 250°C means heating at a constant rate of 5°C/min for 50 min to reach 250°C.

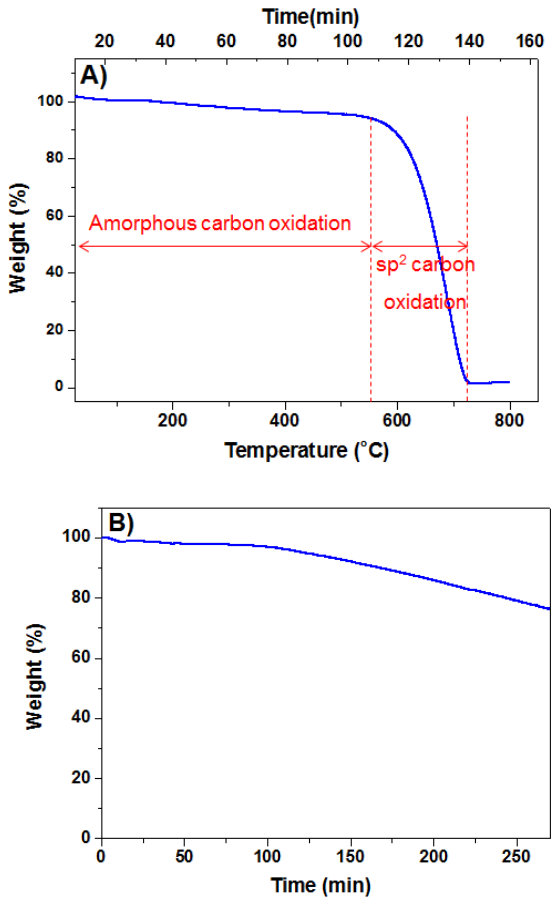

Figure 4-11. TGA profiles of CNT array. A) TGA curve as a function of temperature, which was raised from room temperature to 800°C at the rate of 5°C/min in air. Weight loss was about 5% up to 600°C and the CNT was completely oxidized when 720°C was reached. B) TGA curve as a function of annealing time. Note that it took 100 min to reach 500°C. The temperature was maintained at 500°C for 150 min (100 – 250 min) thereafter. The resulting weight loss was about 5 – 6%.

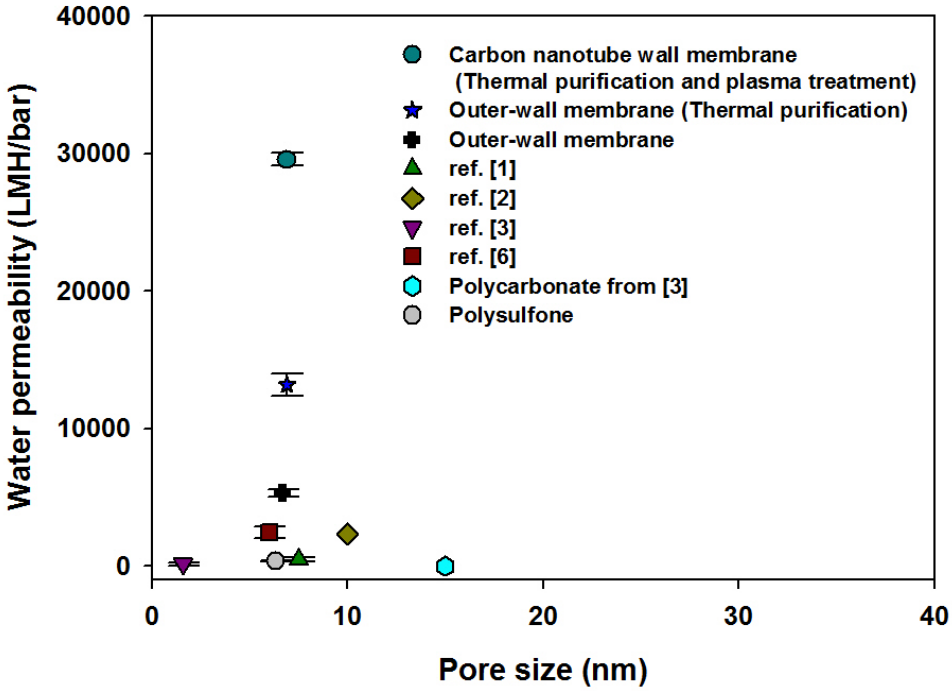

Figure 4-12. Water permeabilities obtained in this work and those by other researchers in the literature based on CNT membranes, polycarbonate membrane and polysulfone membrane (UE4040, Woongjin Chemical, Republic of Korea).

Table 4-2. Characteristics of the CNT wall membrane (dense-array outer-wall CNT membrane).

Sample	Densification factor (D_f)	Ratio of area (A/A_0)	Pore diameter (nm)[a]	Pore density (10^{10} #/cm^2)	Length (mm)	Tortuosity	Volume rate (L/hr)	Water permeability (LMH/bar)	Flow velocity (cm/s)	Pore area (cm^2)	Cap opening method
Outer-wall CNT membrane	1	1	37.8	8.14±0.2	1.3	1.2	0.117	2,328±1,333	0.034	0.968	-
	3	0.36	28.8	26.4±0.8	1.3	1.1	0.181	3,593±1,343	0.056	0.896	-
	6	0.16	15.8	50.8±1.5	1.3	1.1	0.216	4,298±390	0.075	0.799	-
	10	0.098	6.7	83.3±2.5	1.3	1.0	0.290	5,774±759	0.120	0.670	-
	thermal purification	0.098	6.9	83.3±2.5	1.3	1.0	0.662	13,166±806	0.274	0.670	-
CNT wall membrane	10 (thermal purification)	0.098	6.5	166.6±5	1.3	1.0	1.490	29,547±459	0.440	0.938	O_2-plasma
Open-ended	1	1	6.4	8.14±0.2	0.2	1.2	0.070	1,390	0.742	0.026	mechanical
	O_2-plasma - treated	1		8.14±0.2	0.2	1.2	0.096	1,903	1.015	0.026	mechanical
	O_2-plasma - open	1		7.76±0.2	1.3	1.2	0.091	1,816	1.016	0.025	O_2-plasma

*Note that D_f is the area ratio (A/A_0). Pore diameter of outer-wall CNT membrane was determined by BJH, PEG rejection test and calculation method (outer-wall CNT membrane). Pore density was calculated from areal density of vertically aligned CNTs with geometric shape (see Supplementary Information) taken into consideration. Length (=membrane thickness) and tortuosity were determined with high resolution SEM images ([a]: estimated by pore-flow solute model with dextran).

Table 4-3. Dextran rejection rate of CNT membrane compared to commercial UF membrane.

CNT membrane (estimated pore size from Dextran rejection rate)	Rejection rate of dextran (%)						
	5 kDa	12 kDa	25 kDa	80 kDa	150 kDa	410 kDa	670 kDa
	4.0 nm*	5.9 nm*	8.2 nm*	13.6 nm*	17.8 nm*	27.7 nm*	34.3 nm*
D_f10 thermal purification and plasma treatment (6.5 nm)	56.9	**98.4**	100	100	100	100	100
D_f10 thermal purification (6.9 nm)	53.3	**96.0**	100	100	100	100	100
D_f10 (6.7 nm)	55.1	**97.3**	100	100	100	100	100
D_f6 (15.8 nm)	-	1.2	58.6	**96.0**	100	100	100
D_f3 (28.5 nm)	-	-	-	10.4	84.3	**99.8**	100
D_f1 (37.8 nm)	-	-	-		3.9	15.6	**98.3**
Commercial UF (6.3 nm)	61.8	**99.1**	100	100	100	100	100

*: Stokes diameter of the dextran

4.2.2. CNT wall membrane

Another aspect of CNT membrane that could be exploited for better membrane performance is the effect the entrance resistance of CNT could have on the water permeability. An earlier study based on molecular dynamics simulation [94, 121] found that it requires a high external pressure (>120 bar at CNT entry, >1,000 bar at CNT exit) for water molecules to pass through the inner pore of pristine CNT with hydrophobic surface. These theoretical studies suggest that hydrophilic surface modification should decrease the resistance at the entrance and exit of the pores of hydrophobic CNT membrane. For the purpose, an oxygen plasma treatment in the form of oxygen reactive ion etching (RIE) was carried out on the surface of the outer-wall CNT membrane. Oxygen RIE was chosen to open up the CNT fullerene caps so as to make available the inner pores of CNTs for water passage in the process of making the entrances and exits of the pores hydrophilic [122]. Formation of hydrophilic functional groups was confirmed as shown in Figure 4-13 by X-ray photoelectron spectroscopy (XPS). We examined with micro Raman spectroscopy whether the RIE also makes the whole membrane surface hydrophilic. The graph for the CNT wall section shows that the I_G/I_D ratio for the wall section has not changed after the treatment (Figure 4-14(a)). The ratio for the CNT end-cap section, however, was decreased from 0.928 to 0.841 (Figure 4-14(b)). This decrease results due to introduction of some defects or oxygen-functional groups on the CNT end with the cap removal

(also refer to Figure Figure 4-13(b)).

The dual effects the oxygen RIE brought about, i.e., opening up of sealed CNT tubes and making the entrances hydrophilic, led to a significant increase in the water permeability as shown in Figure 4-12, resulting in a more than twofold increase in the water permeability over that obtained after thermal treatment. This water permeability of CNT wall membrane attained, which is close to 30,000 LMH/bar, is more than an order of magnitude larger than the highest water permeability reported for CNT membranes, which is around 2,400 LMH/bar.

To separate the effect of CNT cap opening from that of making the entrances hydrophilic, separate experiments were carried out with open-ended CNT membranes in which the CNT caps were removed by microtoming (noted ‘mechanical’ in Table 4-2). Pores of the open-ended membrane formed by the microtoming was observed by HR-TEM (Figure 4-15). The increase in water permeability due to oxygen plasma treatment for the same mechanically prepared CNT membranes (second and third rows from the bottom in the table) amounts to 37%, indicating that making the entrances and exits hydrophilic led to an increase of 37% for the CNT membrane. Noting that the factor by which the permeability increased due to the oxygen RIE is 2.33, the increase in the permeability in multiples that can be attributed to opening of capped CNT tubes

is 1.7. The permeance of the open-ended membrane prepared by O_2 plasma is 1,816 LMH/bar (first entry from the bottom in Table 4-2), and that of the open-ended membrane fabricated by microtoming is 1,903 LMH/bar (the second entry). From these experimental results, we determined the fraction of open-ended CNTs for the plasma treated membrane by dividing 1816 by 1903, which yields 95.4% for the fraction of the CNT tips opened by oxygen plasma relative to the microtomed open-ended CNT tips. The presumption here is that all CNT ends were opened by the microtoming. Based on the permeabilities given in the third entry from the bottom and the first from the top in the table, the multiple is 1.57 ((2328+0.954×1390)/2328), which compares well with the independent value of 1.7. The CNT wall membrane shows similar performance to that of the outer-wall membrane(D_f 10 and thermally purified D_f 10) in ability to reject the particles (Table 4-3) in spite of the significant permeability increase.

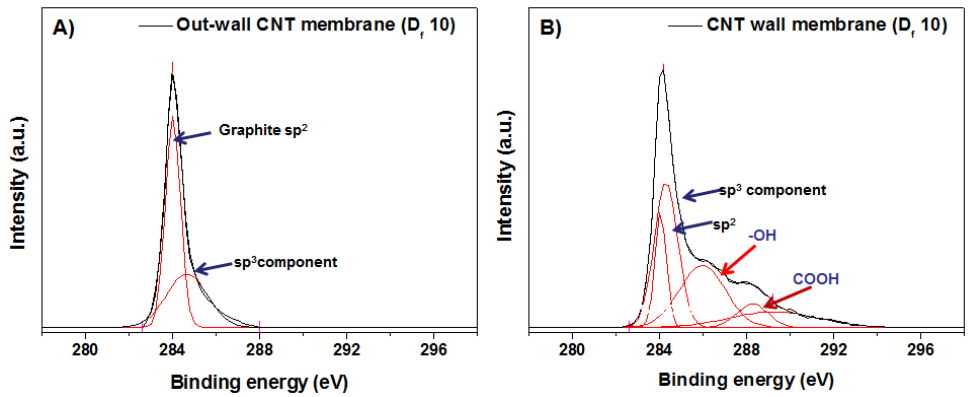

Figure 4-13. X-ray Photoelectron spectroscopy (XPS) of CNT membranes surface. A) outer-wall CNT membrane (D_f 10). B) O_2-RIE treated CNT wall membrane. The two peaks at 246, 246.8eV are attributed to the sp^2 and sp^3 component. CNT cap of CVD-grown CNTs generally has many defects. XPS of the O_2-RIE treated membrane (Figure 4-12(B)) shows two notable points. The sp^2 peak intensity at 246 eV is lower than the sp^3 peak intensity at 246.8eV because of many defects at CNT tips discovered by removing the CNT caps. Additional two peaks at about 286, 288 eV are assigned to the C-OH and OH-C=O group, respectively.

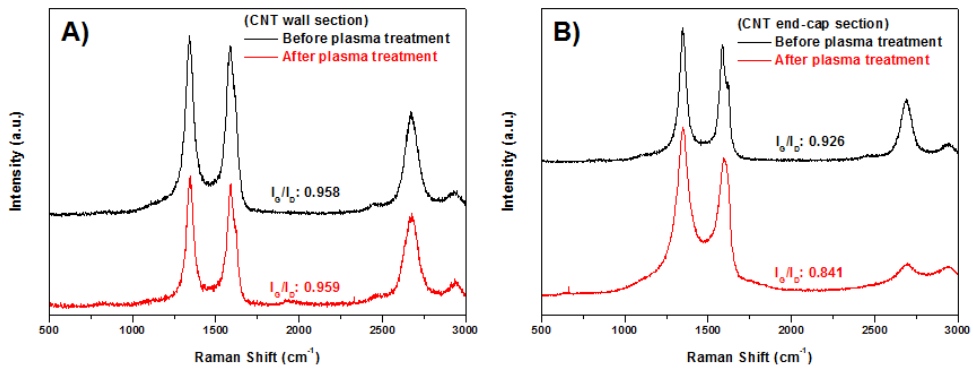

Figure 4-14. Raman spectra of Densified CNT array (D_f 10) before and after plasma treatment: A) CNT wall (cross-section) and B) end-cap section (top surface) of as-grown CNT array before and after plasma treatment. The graph for the CNT wall section shows that the I_G/I_D ratio for the wall section has not changed after the treatment. The ratio for the CNT end-cap section, however, was decreased from 0.928 to 0.841. This decrease results due to introduction of some defects or oxygen-functional groups on the CNT end with the cap removal (Figure 4-13(b)).

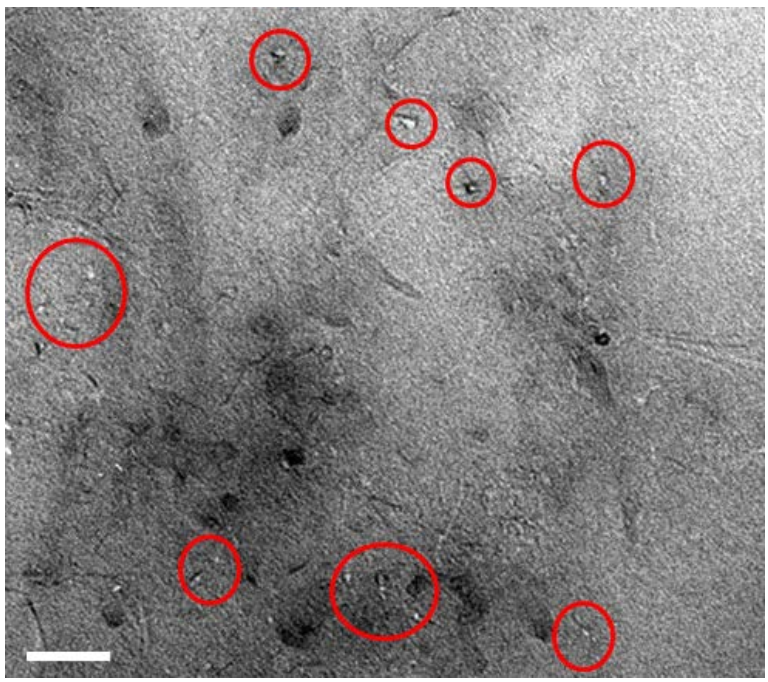

Figure 4-15. TEM image (top view) of open-ended membrane. White dots in the image are pores of CNTs (scale bar: 50 nm).

4.2.3. Biofouling characteristics

Carbon nanotube membranes are known to have anti-biofouling capability because of its ability to inactivate the bacteria. Not known, however, about CNT membrane is the other aspect of biofouling that has to do bacteria adhesion. To investigate the bio-fouling behavior of the outer-wall CNT membrane, bacterial adhesion tests were carried out for 72 h. *Pseudomonas aeruginosa* PA01 was selected in this study because this species is commonly found in wastewater and mainly responsible for membrane biofouling [123-125]. Two independent aspects of biofouling are of interest: bacterial adhesion and biofilm formation. For the adhesion, the images by confocal laser scanning microscopy (CLSM) can be examined and compared for various cases, as shown in Figure 4-16(a), (d) and (g), for outer-wall CNT membrane (D_f of 10), CNT wall membrane, and commercial polysulfone (PSf) ultrafiltration (UF) membrane, respectively. In the images, green color indicates live cells and red color represents dead cells. After 24 h of test, fewer cells are seen to have adhered onto both CNT membranes compared to commercial PSf UF membrane, which indicates that CNT membrane has an anti-adhesion property. Interestingly, dead cells were barely observed on the CNT membrane surface. This result shows that the CNT membrane impedes bacterial adhesion presumably due to its rough surface at nano-scale. This result reveals another aspect of anti-biofouling behavior not observed so far. The ability of CNT membrane to impede bacterial adhesion

contrasts the previously reported antimicrobial properties of CNT that is ascribed to sharp edges of CNT causing physically damaged cell membrane, eventually leading to inactivation of bacteria [74, 126, 127].

The behavior of *P. aeruginosa* PA01 biofilm formation that follows the cell adhesion can be examined from the CLSM images obtained after 48 h and 72 h of test, which are shown in Figure 4-16(b), (e) and (h), and (c), (f) and (i), respectively. A clear distinction can be made between biofilm formation on CNT membranes and that on commercial PSf UF membrane. It is evident from Fig. 3(i) that abundant bacteria adhered onto the PSf UF membrane resulted in the formation of well-mature biofilm. In contrast, the biofilm formation is seen to have progressed much less on the outer-wall CNT membranes (Figure 4-16(c)) and the CNT wall membrane (Figure 4-16(f)). In fact, the *P. aeruginosa* PA01 concentration on the CNT membranes after 72 h (Figure 4-16(c) and (f)) appears to be similar to that after 48 h (Figure 4-16(b) and (e)). Better resistance to biofilm formation exhibited by the CNT membranes is a distinct advantage.

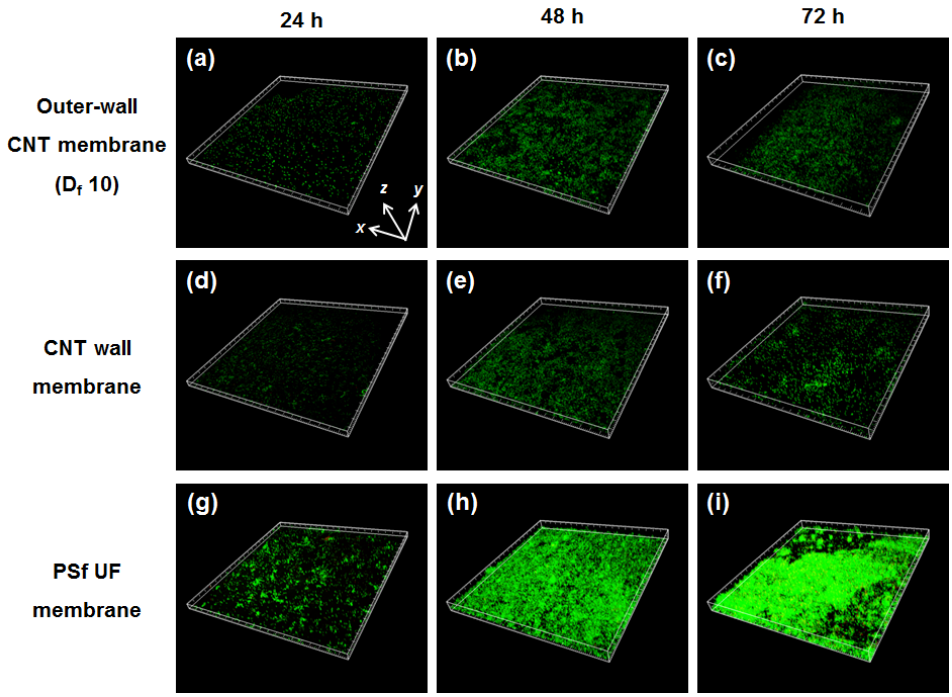

Figure 4-16. Biofouling characteristics as revealed by confocal laser scanning microscopy (CLSM) images as a function of time. The images in the first row ((a), (b), and (c)) are for outer-wall CNT membrane (D_f = 10), and those in the second row ((d), (e), and (f)) are for CNT wall membrane and those in the third row ((g), (h), and (i)) are for commercial polysulfone (PSf) ultrafiltration (UF) membrane (in the images, x axis: 512 μm, y axis: 512 μm, z axis: ((a), (d) & (g)) 12 – 14 μm after 24 h, ((b), (e) & (h)) 20 – 26 μm after 48 h, and ((c), (f) & (i)) 23 – 32 μm after 72 h. In the images, live bacteria cells are green and those dead are red.

4.3. Conclusion

The densified outer-wall CNT membrane is unique in that a decrease in the pore size of membrane results in an increase in the water permeability. Another unique feature of the densified outer-wall CNT membrane is that the pore diameter can readily be varied by simple mechanical compression in the range between 7 nm and 38 nm. This feature would be attractive when the membrane is used as a flexible, vertically aligned mesoporous material for possible applications in catalysis, sorption, gas sensing, optics, photovoltaics, and macromolecule separation, including protein separation. The CNT wall membrane that can be obtained by thermal and oxygen-plasma treatments of the densified outer-wall membrane signifies arrival of a different class of membrane. It can deliver a water purification capacity that is larger than any CNT membrane by more than an order of magnitude, reaching the level of 30,000 LMH at 1 bar, which is almost two orders of magnitude higher than that attainable with traditional polymer membrane. Its anti-biofouling capability is much enhanced by its ability to impede bacteria adhesion, in addition to its capability to resist biofilm formation.

5. Mixed Carbon Nanotube Membrane

5.1. Materials & Methods

5.1.1. Materials

Multi-walled carbon nanotubes used as carbon nanotube (CNT) materials were received from Nanocyl (Belgium). The supplied information of CNTs by the company is as follows; the average diameter and average length of CNT are 10 − 20 nm and 10 − 20 μm, respectively. Polysulfone (PSf) membranes were received from Woong-jin Chemicals (Republic of Korea) and used for a supporting part of the composite membrane. Sulfuric acid (H_2SO_4, 98%), nitric acid (HNO_3, 60%), and isopropyl alcohol (IPA) were supplied from Daejung Chemicals (Republic of Korea) and used without any treatment and purification. *m*-Phenylenediamine (MPD, 99%), trimesoyl chloride (TMC, 98 %), poly(vinylalcol) (13,000 g mol^{-1}, PVA), and sodium chloride (NaCl, 99%) were supplied from Aldrich and used without any purification. Deionized (DI) water was obtained from water purification system (Synergy, Millipore, USA), having a resistivity of 18.3 mΩ cm. *n*-Hexane (95%) was received from Samchun Chemicals (Republic of Korea).

The CNTs from Nanocyl were modified using the acid mixture of sulfuric acid and nitric acid (3:1 volume ratio) to impart the functional groups such as

carboxylic acid [128]. 0.2 g of pristine CNTs and 90 mL of the acid mixture solution were placed into 100 mL round-bottom flask equipped with a magnetic stirring bar and the mixture was sonicated for 30 min. Then the flask was placed into an oil bath thermostated at 75^{o}C with stirring. After 4.5 h of reaction, the solution was cooled to room temperature and diluted with 2.0 L of water. The diluted solution was filtered using anodic aluminium oxide (AAO) filter (Anodisc, Whatman Co. USA). The filtered solid was neutralized by pouring water until a neutral pH is attained. The resulting oxidized CNTs on filter were dried in the 35°C vacuum oven.

For the confirmation of attached acid groups on the CNT surface during the modification, analyses using Raman spectroscopy and XPS were carried out. In the Raman spectra of pristine CNT and oxidized CNT, distinct characteristic peaks of D band and G band of CNT were observed 1,308 cm^{-1} and 1,600 cm^{-1}, respectively. The D/G ratio, which is the peak intensity ratios of D band and G band, increased after the modification, indicating that acid treatment increases the defect on CNT surfaces. Similar results increasing the D band intensity by the functionalization of CNT surface were reported by others. Surface compositions of the CNTs prepared from the acid mixture were characterized by XPS analysis. The content of oxygen increases after the modification process. The increase of the atomic ratios of oxygen to carbon (O/C) indicates the introduction of acid groups on the CNT surface by the acid treatment. The acid

group formed on CNT can increase the dispersion of CNTs in the aqueous solution and in the polyamide and PVA layers by the H-bonding and/or dipole-dipole interactions. Therefore, acid groups were attached on the defective surfaces of CNT during the modification process according to the Raman spectroscopy and XPS analysis. Since CNT surfaces were chemically modified to functional groups having oxygens, the CNTs prepared from the acid mixture were named as the oxidized CNTs.

5.1.2. Preparation of PA-CNT-PVA membrane

Polysulfone (PSf) membrane was treated using IPA for 10 min to enlarge pores and washed several times with water. The alcohol pretreated PSf membrane was put into the water bath for 3 h to stabilize the pores. 2.0 wt% of MPD aqueous solution and 0.1 wt% of TMC solution in *n*-hexane were prepared for the interfacial polymerization. The pretreated PSf membrane was placed into the bath with 500 g of the MPD aqueous solution. After 3 h, membrane was taken out and air bubbles and droplets on the PSf membrane surface were removed by rolling a rubber roller. The membrane was fixed on the acryl flat board with rubber mold and aluminium tape. The TMC solution was poured on the PSf membrane saturated with the aqueous solution for the formation of the polyamide active layer by the interfacial polymerization. After 60 s, the excess

of TMC solution on the membrane was removed and the membrane was placed in the 100°C oven for 5 min to induce the further polymerization and crosslinking reactions. Then the resulting membrane, polyamide (PA) membrane, was washed with water several times. The 0.1, 0.2, or 0.4 g of oxidized CNTs were dispersed in 100 mL of water to prepare the 0.1, 0.2, or 0.4 wt% CNT-dispersed solutions, respectively. The polyamide membrane was placed between sintered glass filter and glass holder. Afterward, the CNT-dispersed solution was poured on the surface of the polyamide membrane. Then vacuum filtration was performed using high power vacuum pump to form uniformly deposited of CNTs on the polyamide membrane. The CNT-deposited polyamide membrane was fixed on the acryl flat board and placed into the bath with the aqueous solution containing 0.2, 0.5, or 1.0 wt% of PVA for 3 h, then membrane was taken out and placed in the 100°C oven for 10 min to remove residual water in the membrane. The polyamide membranes with only PVA were also prepared to study the effect of oxidized CNTs. The polyamide membrane was coated with 0.2, 0.5, or 1.0 wt% of PVA solution. The coating time and post treatment were same with the preparation of polyamide membrane with CNT and PVA. The prepared composite membranes without CNTs and PVA were named as PA membranes. The polyamide membranes with only PVA were abbreviated for PA-PVA membranes and those with CNT and PVA were PA-CNT-PVA membranes. The PA-PVA and PA-CNT-PVA membranes were further specified as PA-PVA##

and PA-CNT#-PVA##, where # and ## indicate the concentrations (wt%) of CNT-dispersed solutions and those of PVA coating solutions, respectively.

5.1.3. Characterizations

Raman spectroscope (LabRam ARAMIS, Horiba Jobin-Yvon, France) was used for the analysis of the modification of CNTs. Pristine and oxidized CNTs were dispersed in isopropyl alcohol in sonication bath. The dispersed solution was dropped on the glass plate and then dried in the 35℃ vacuum oven. The excitation source was a diode laser with an excitation wavelength of 785 nm and a power of 5 mW. The laser excitation was focused using a ×100 objective. The surface compositions of the CNTs and membranes were analysed by X-ray photoelectron microscopy (XPS, PHI-1600) using Mg Kα (1254.0 eV) as radiation source. Survey spectra were collected over a range of 0-1100 eV, followed by high resolution scan of the C 1s, O 1s and N 1s regions. Morphology of CNTs was observed by transmission electron microscopy (TEM, LIBRA 120, Carl Zeiss, Germany). 1.0 mg of CNT was dispersed in 1.0 mL of water using sonication bath and then the dispersed solution was dropped on the carbon grid. The grid was dried in the 35℃ vacuum oven over 8 h. For confirmation of the crosslinking reaction, FT-IR spectra of dried membranes were recorded in the attenuated total reflectance (ATR) mode in the frequency

range of 4000 – 650 cm^{-1} on a Nicolet 6700 instrument (Thermo Scientific, USA). The spectrum was recorded as the average of 32 scans with the resolution of 8 cm^{-1}. Each sample was put in equal physical contact with the sampling plate of the spectrometer accessory to avoid differences caused by pressure and penetration depth. Surface morphologies of the membranes were inspected by scanning electron microscopy (SEM, JSM-6701F, JEOL) using a field emission scanning electron microscope (FESEM). The mechanical properties of PA and PA-CNT-PVA membranes were measured by universal testing machine (UTM, LS1SC-150V) with a strain of 10 mm min^{-1} in air at 23°C under a 45% relative humidity. The dumbbell specimens were prepared using the ASTM standard D638 (Type V specimens dog-bone shaped samples). The mechanical properties were measured more than 4 times for each membrane. Surface roughness and morphology of the membrane were measured by atomic force microscope (AFM, Asylum Research, Santa Barbara, CA, USA). A silicon cantilever with a spring constant of 2 N m^{-1} was used for scanning. The root mean square (RMS) roughness was determined by the scan size of 5 µm by 5 µm of the sample and 600 nm depths.

5.1.4. Membrane filtration test

Filtration experiments were carried out by lab-scale cross-flow membrane test

unit with an effective filtration area of 3.3 × 6.8 cm^2 with the 0.3 cm of channel height. The pressure was maintained at about 15.5 bar (225 psi) and the feed solution was 2,000 mg L^{-1} of NaCl solution. These membrane operating conditions have been generally used in BWRO membrane researches by others. Cross-flow velocity at the membrane surface was 500 mL min^{-1} in the filtration system. Water flux was measured by weighing the permeate solution after the membranes were compressed for 1 h at 15.5 bar and permeated water was collected for 2 h. Membrane flux, J, was calculated using Eq. 5-1:

$$J = \Delta V / (A \times \Delta t) \qquad \text{(Eq. 5-1)}$$

where ΔV is the volume of permeate collected between two weight measurements, A is the membrane surface area, and Δt is the time between two weight measurements.

Salt rejection was calculated using the following Eq. 5-2:

$$R = (1 - C_p / C_f) \times 100\ \% \qquad \text{(Eq. 5-2)}$$

where R is the salt rejection parameter, C_p is the salt concentration in permeate, and C_f is the salt concentration in feed. The salt concentrations were measured using conductivity meter (InoLab Cond 730P, WTW 82362, Weilheim). All membrane performance results shown in Table 5-2 are the average values obtained by more than three measurements from the three membrane samples

prepared at different times.

5.1.5. Biofouling experiments

The antibiofouling property of the membranes was evaluated by a lab-scale cross-flow membrane system using the feed solution containing *Pseudomonas aeruginosa* (*P. aeruginosa*) PAO1 tagged with GFP (150 μg mL^{-1}) as a model bacterial strain. Nutrients in the feed solution were composed of 0.1 wt% of tryptic soy broth (TSB; Bacto, Franklin Lakes, NJ), 10 mM of sodium chloride, and 10 mM of sodium citrate in 6 L of water. The initial flux, cross-flow velocity, and temperature values used in the lab-scale cross-flow RO experiment were 40 L m^{-2} h^{-1} (LMH), 270 mL min^{-1}, and 25°C, respectively. The membrane was compacted by filtering distilled water for 18 h, conditioned by filtering the feed solution for 6 h for the biofilm formation through the bacterial adhesion, and then the flux changes were monitored to estimate the biofouling progress by filtering the feed solution for 24 h. It is well-known that the biofilms can be easily formed after 6 h contact with the bacterial solutions and the major flux reduction was known to be resulted from the biofilm formation through the bacterial adhesion [129]. Microscopic images were taken by confocal laser scanning microscopy (CLSM, Eclipse 90i, Nikon, Japan) to observe biofouling morphology on the membrane surface after staining with a BacLight Live/Dead

bacterial viability kit (Molecular Probes, USA). More details of biofouling test for the adhesion of bacteria on the membranes are described in the previous report [129].

5.2. Results and Discussion

5.2.1. Characteristics of oxidized CNTs

The pristine CNTs were chemically modified by the strong acid mixture of sulfuric acid and nitric acid solutions (3:1 volume ratios) to prepare CNTs with acid functional groups. We could conclude that the acid groups such as carboxylic acid were incorporated on the surface of the CNT through this modification step from the Raman spectroscopy, XPS, and TEM results as shown in the Figure 5-1, 5-2 and 5-3. In fact, it has been reported previously that such acid treatment can functionalize CNT surface to carboxylic acid groups [130, 131]. Since the CNTs were deposited on the surface of the polyamide membrane by the vacuum filtration process using the CNT-dispersed aqueous solution, the dispersion of CNTs in the aqueous solution is crucial to obtain the uniform CNT layers on the polyamide membrane. Figure 5-3 shows the TEM images of the 0.1 wt% of CNT dispersed solution, the lowest concentration of CNTs in the aqueous solution used for the formation of CNT layer on the polyamide membrane. If CNTs are well dispersed in this aqueous solution, CNTs where deposited on the polyamide layer can be also well-dispersed and they can have the large surface area to give the maximum antibiofouling properties to the membrane. TEM image of pristine CNTs shows the bundle morphology with long tube length about 15 μm, while shortened single strands without any

entanglements were observed from the oxidized CNTs. Since the oxidized CNTs are well-dispersed in water, we could have prepared the uniform CNT layer on the polyamide membrane. Although the CNTs were functionalized by the carboxylic acid to produce the aqueous solution having well-dispersed CNTs, the PA-CNT-PVA membrane prepared by the deposition of CNTs in the aqueous solution was found to have some CNT bundles on the membrane surfaces. Still the PA-CNT-PVA membrane with the small CNT bundles on the surfaces showed improved membrane stability and biocidal properties as discussed in the next part of this paper.

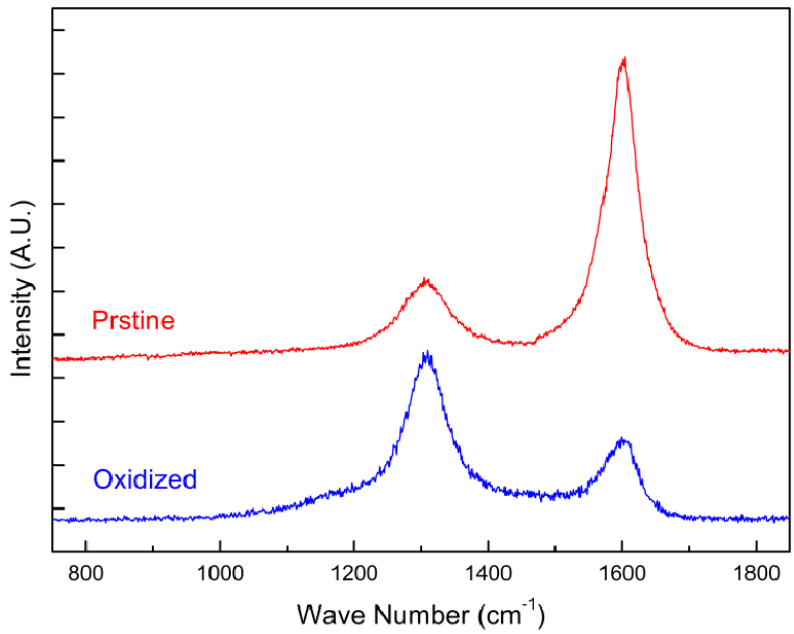

Figure 5-1. Raman spectra of pristine and oxidized CNT.

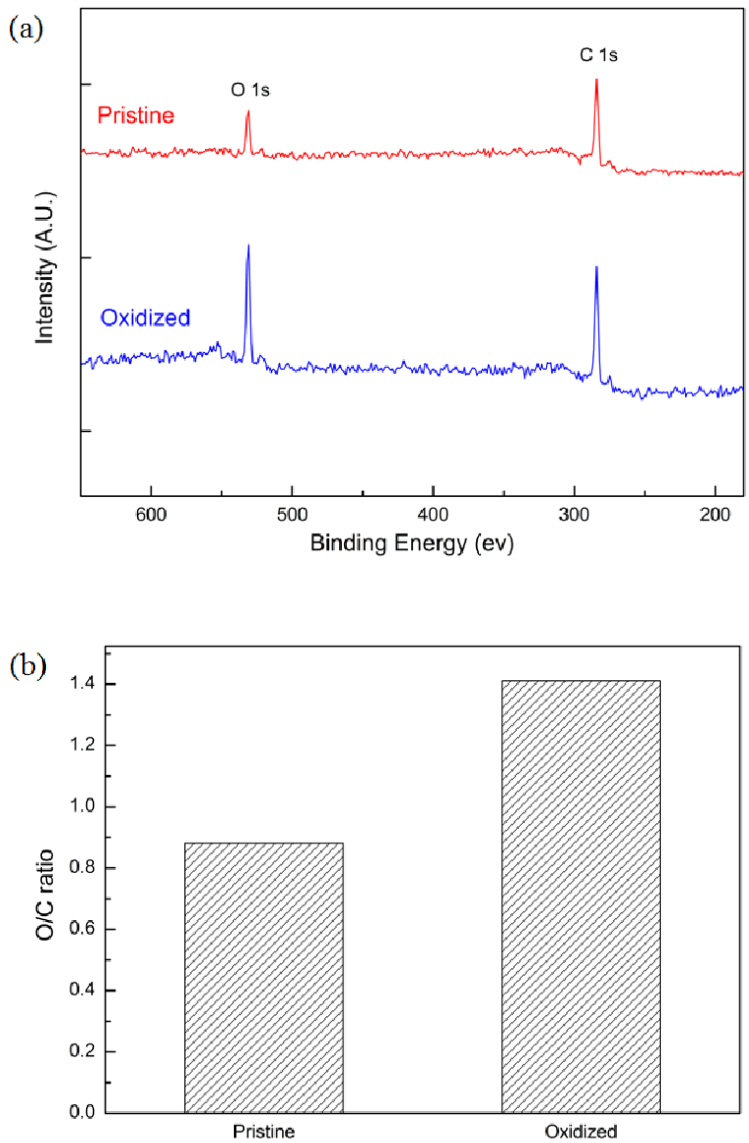

Figure 5-2. (a) XPS spectra and (b) O/C ratios of pristine and oxidized CNT.

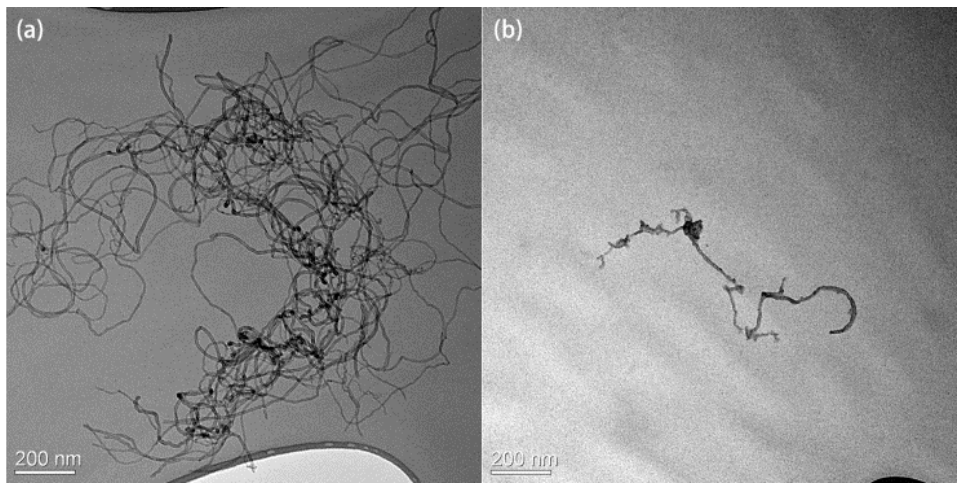

Figure 5-3. TEM micrographs of (a) pristine and (b) oxidized CNTs.

5.2.2. Characteristics of PA-CNT-PVA membrane

Since CNTs are deposited on the membrane surface using filtration method, only the physical interactions are possible between the CNTs with the polyamide layers, then they could be easily detached and flowed out of the membrane during the filtration, then this would result in the decrease of the antibiofouling ability and also the environmental problems in practical applications. To immobilize the CNTs on the membrane, PVA was coated on the CNT-deposited polyamide membrane and heated at 100°C for the crosslinking reactions of the hydroxyl groups of the PVA with the carboxylic acid groups on CNTs and some of the unreacted carboxylic groups of TMC. It is also possible that the unreacted amine groups in MPD could react with the carboxylic groups to form further cross-linked structures. Figure 5-4 shows the FT-IR spectra of the PA membrane and the PA-CNT-PVA membranes with/without heating at 100°C. The crosslinking reaction could be confirmed by the disappearance and/or the intensity decrease of the peaks from carboxylic acid (C=O stretch at 1,670 cm^{-1}, O-H stretch at 3,350 cm^{-1}), hydroxyl group (O-H stretch at 3,350 cm^{-1}), and amine group (N-H bend at 1,538 cm^{-1}). The peaks of amine group and carboxylic acid in the spectrum of the PA membrane indicate the presence of the monomeric structures (MPD and TMC) in the membrane. The peak intensities for carboxylic acid and hydroxyl group in the PA-CNT-PVA membrane without heating were found to be larger than those for the PA membrane because the

oxidized CNTs and PVA have the carboxylic acid and hydroxyl groups, respectively. Additionally, the increase of the intensity for alkane peaks (sp^3 C-H stretch at 2,976 and 2,850 cm^{-1}) was observed after the PVA coating, originating from the ethylene backbone structures of PVA. After the heating process for the crosslinking reaction, the decrease in intensity (and/or disappearance) of carboxylic acid, hydroxyl, and amine group peaks was observed, while the peaks from polysulfone (doublet asymmetric O=S=O stretch at 1,298 and 1,325 cm^{-1}, and symmetric O=S=O stretch at 1,024 cm^{-1}) were observed in all the membranes with very similar intensities.

To confirm the crosslinking mediated immobilization of CNTs on the membrane, the cross-flow membrane test for the PA-CNT-PVA membrane was performed using only pure water, to observe any possible detachment of CNTs. After 3 days of filtration, 30 mL of the feed and permeate water were taken in a 50 mL vial and dropped on the TEM grid to observe any CNT detachment. Any CNTs were not observed in either the feed or permeate water, indicating that CNTs were chemically bonded stably with the polymers in the PA-CNT-PVA membrane. However, when the same pure water filtration test was performed using the PA-CNT-PVA membrane without the crosslinking, a few bundles of CNTs were observed in the feed water. The stability of PA-CNT-PVA membrane after the 3 days of filtration test was further confirmed by the XPS analysis of the membranes. The surface composition of the PA-CNT-PVA membrane after 3

days test was found to be almost identical with those of the membrane before the test. Our TEM and XPS results might not have sensitivity in detection of a few CNTs detached from the top surface of the membrane due to their resolution limitations. The CNT detachment from the membrane is an important issue for the practical application of PA-CNT-PVA membranes and should be addressed in depth. Such study was beyond the scope of this research but is required in future by various instrumental and experimental approaches. Still we strongly believe that the CNT detachment should be minimal because CNTs are covalently bonded with PVA and polyamide on the top layer of the membrane, and more importantly CNTs cannot go through the membrane because the pore size of the RO membranes are much smaller than the sizes of the CNTs used in this study, then the permeated water or the purified water should not contain any CNTs. When we tried to prepare the PA-CNT-PVA membrane using the pristine CNTs without the oxidation, CNTs were not deposited uniformly on the polyamide layer because the pristine CNTs were not dispersed in water. In addition, since pristine CNTs do not have any functional groups such as hydroxyl and carboxylic acid, they could not react with hydroxyl groups of PVA and/or unreacted amine groups of MPD, then such CNTs could be easily detached from the membrane during the filtration test.

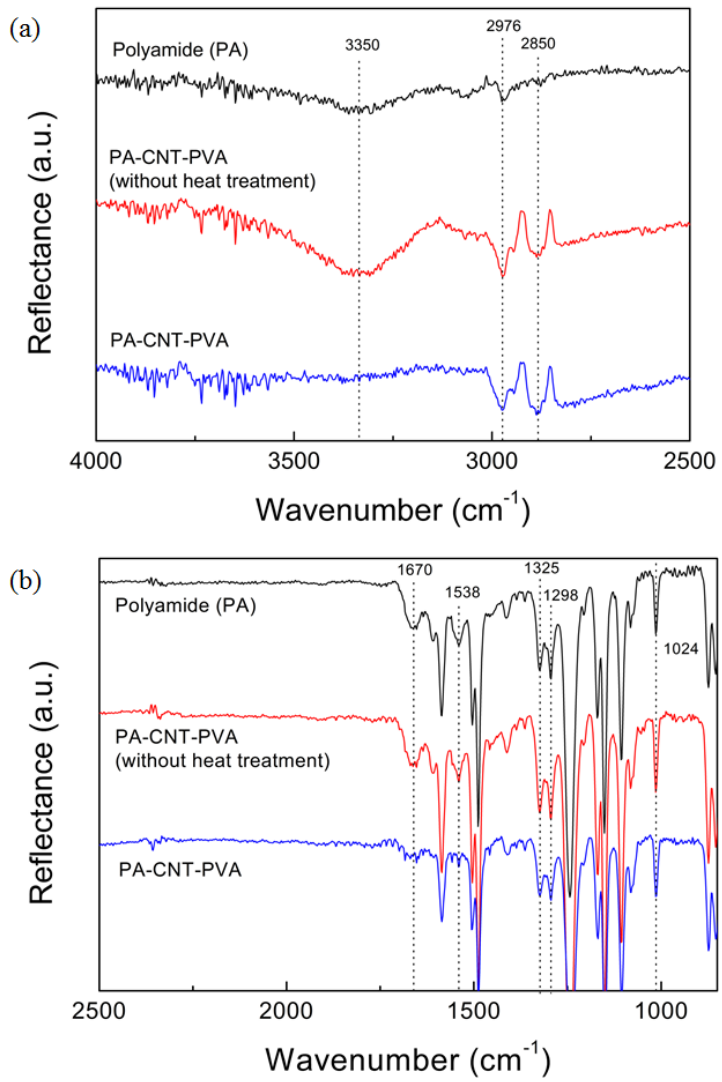

Figure 5-4. FT-IR spectra of PA membrane, PA-CNT0.2-PVA0.2 membrane without heat treatment, and PA-CNT0.2-PVA0.2 membrane; (a) at 4,000 – 2,500 cm^{-1} and (b) at 2,500 – 850 cm^{-1}.

SEM images in Figure 5-5 shows the surface morphology of the PA and PA-CNT-PVA membranes. Typical noodle or ridge-and-valley structures originated from polyamide layers (Figure 5-5(a) and (b)) were observed on the surfaces of the PA membrane, as previously reported by others [132, 133]. Although the similar noodle structures were observed on ×10,000 SEM image of PA-CNT-PVA membrane (Figure 5-5(c)), on higher magnification (the ×30,000) images of the PA and PA-CNT-PVA membranes were found to be quite different. Obviously the CNT deposition by the vacuum process and the PVA coating followed by the heat treatment changed the noodle structure of the PA membrane to a somewhat coagulated noodle structure of the PA-CNT-PVA membrane. In addition to the coagulated noodle structure, bundle structures were also observed in the PA-CNT-PVA membranes. We believe that the bundle structures originated from the oxidized CNT bundles covered by PVA. Similar coagulated images of planer structures were observed from the polyamide membrane deposited by the graphene oxide, as reported by others [134]. The existence of the CNT bundles on the PA-CNT-PVA membrane could also be observed from the optical images (Figure 5-6). Transparent polyamide layers were observed from the PA membrane, while somewhat hazy images originating from CNT bundles were observed from the PA-CNT-PVA membrane.

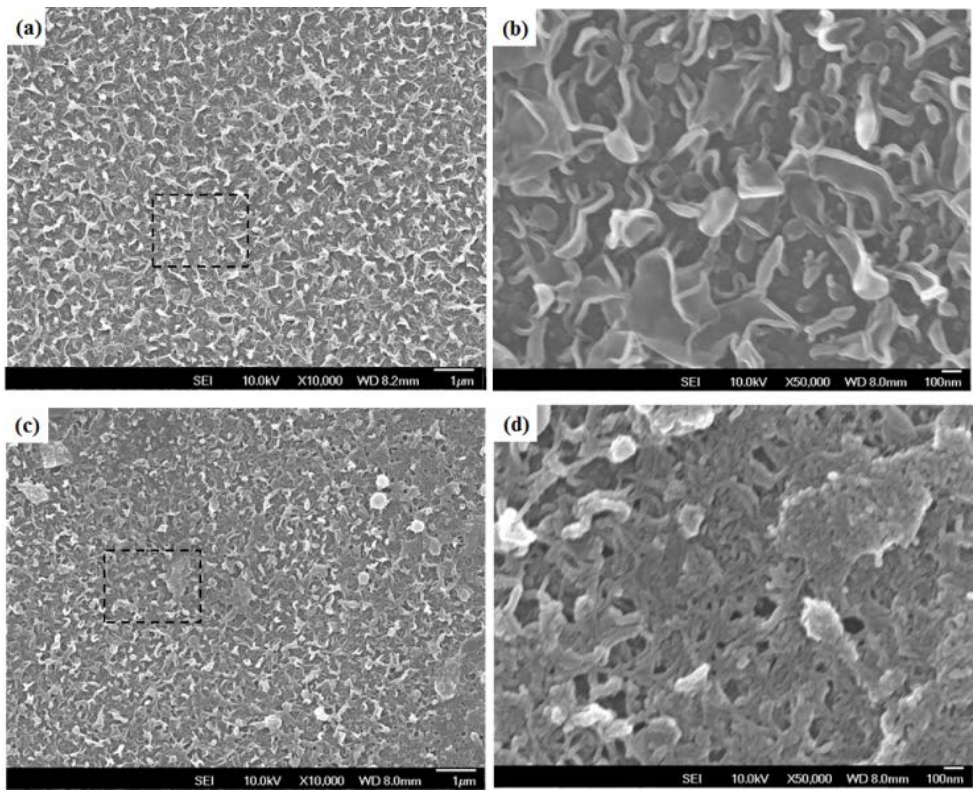

Figure 5-5. SEM images of (a) PA membrane, (b) magnified image of square lined region in (a), (c) PA-CNT0.2-PVA0.2 membrane, and (d) magnified image of square lined region in (c).

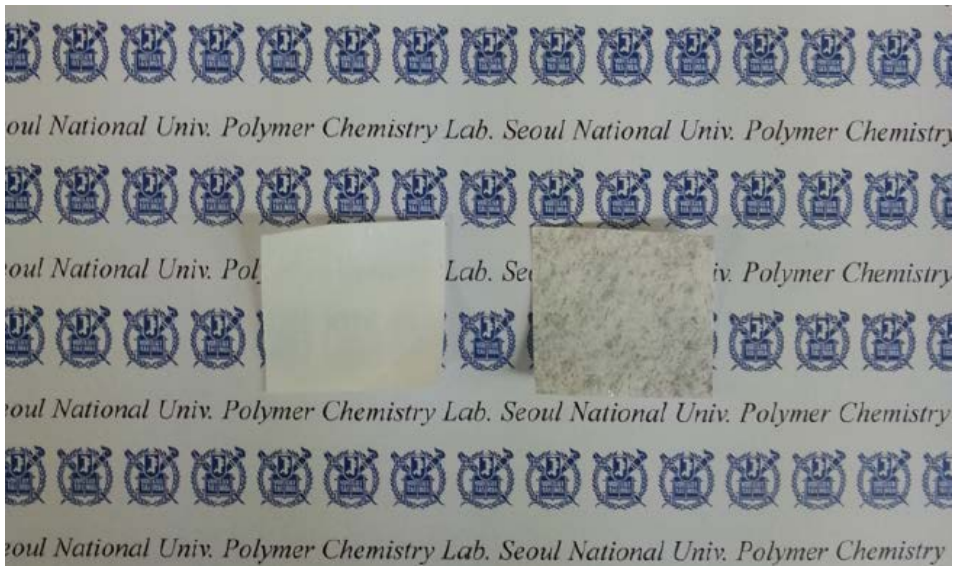

Figure 5-6. Photographs of PA membrane (left) and PA-CNT-PVA membrane prepared by 0.2 wt% of CNT-dispersed solution and 0.2 wt% of PVA solution (right).

Since RO systems are operated under the high pressure (from 15 to 55 bar), the compaction of membranes, causing the decrease of the water flux is commonly observed from most of the RO membranes, as reported by others [128, 135]. Therefore, it is very desirable to have RO membranes with high enough mechanical stability to endure the high operating pressure. CNT has been widely used as a filler to improve the mechanical property of the nanocomposites [135]. We also found that the PA-CNT-PVA membrane had improved mechanical properties compared with PA membranes. For example the Young's modulus, tensile strength, and stress at break values of PA-CNT0.2-PVA0.2 membrane, where 0.2's indicate the weight percent of CNT and PVA respectively in the aqueous solution used for the membrane preparations, were found to be 85.5, 48.0, and 21.4% larger than those of the PA membrane (Table 5-1). These improved mechanical properties of PA-CNT-PVA membrane were larger than those of PA-PVA membranes, indicating that the main factor increasing mechanical stabilities is CNT layer. We also measured the mechanical property values of the commercial RO membrane (LFC-1, received form Hydranautics) for comparison. The mechanical properties of the LFC-1 membrane were found to be even smaller than those of PA membrane possibly because non-woven polyester and polysulfone support used for LFC-1 are different from those used in this study.

Table 5-1. Mechanical strength of PA, PA-PVA0.2, PA-CNT0.2-PVA0.2, and LFC-1 membranes.

	Young's Modulus [MPa]	Tensile Strength [MPa]	Stress at Break [MPa]
PA	1197 ± 268	18.4 ± 0.2	14.4 ± 0.4
PA-PVA	1217 ± 218	18.8 ± 0.7	15.1 ± 0.8
PA-CNT-PVA	2221 ± 118	27.3 ± 0.9	17.4 ± 1.9
LFC-1	937 ± 73	17.8 ± 0.6	13.3 ± 2.2

5.2.3. Water flux and salt rejection of PA-CNT-PVA membrane

The water flux and salt rejection values of PA, PA-PVA and PA-CNT-PVA membranes were obtained using the cross-flow filtration system. LFC-1 membrane, the commercialized RO membrane for the filtration of brackish water, was also tested for the comparison. Table 5-2 shows the water flux and salt rejection values of all the membranes. We also tried to observe the effect of the concentrations of the CNT and PVA in aqueous solutions, on the membrane performances. When the concentration of the PVA solution was larger than 1.0 wt%, the water flux value was found to be too small to be used as a RO membrane because thick and dense active layers can be formed on the top of the membrane from the quite concentrated PVA solutions. Therefore, the water flux of PA-PVA1 and PA-CNT0.2-PVA1 membranes were only 5.4 ± 2.7 LMH and 4.2 ± 1.0 LMH after 5 h of the operation, respectively. We could not obtain the flux value after 2 h because the amount of permeate water was too small to be measured using our equipment. When the concentration of the PVA solution was smaller than 0.05 wt%, we observed the detachment of the CNT from the membrane surfaces, which was confirmed from SEM images of the membrane surfaces and also from the TEM studies of the feed and permeate water after the pure water filtration test. Therefore, 0.05 wt% of PVA solution was not enough to make chemically and physically stable cross-linked structures, while 1.0 wt% of PVA solution makes too thick PVA coated layers to decrease the water flux

although quite large salt rejection value could be obtained (salt rejection value of PA-CNT0.2-PVA1 was 98.4 ± 0.5%). It was also found that the PVA coating layers decrease the water flux and increase the salt rejection value. Comparing with the PA membrane without any CNT and PVA, all the PA-PVA membranes showed smaller water flux and larger salt rejection values. The PVA coating can obviously fill some of the possible water channels in the PA layer, which decreased the water flux values, while it can increase the salt rejection efficiency. However, the changes of water flux and salt rejection values of PA-PVA membranes prepared with 0.2 or 0.5 wt% of PVA solution were not much. Thus, the PVA coating with from 0.2 to 0.5 wt% solution were practical to use RO membrane application. When the concentrations of CNT were changed from 0.1 to 0.4 wt%, any obvious trends in the water flux and salt rejection values were not observed because CNTs were just deposited on the polyamide layer and do not affect transport of water molecules and ions. When 1.0 wt% of CNT-dispersed solution was used, CNTs were found to be aggregated on the membrane surface forming a chunky structure and the effective PVA coating was not possible because the surface of the membrane become too rough. Furthermore, when the membrane was used for the pure water filtration, CNT detachment was observed. CNTs in the polymeric membrane have been reported to increase the water flux because CNT could provide the hydrophobic water flow channel and/or due to the oxygen functional groups. However, all the PA-

CNT-PVA membranes showed slightly smaller water flux values than the PA membrane in this study because CNTs were not incorporated within, but just coated on the surface of the polyamide layers. Furthermore, CNTs are cross-linked with the PVA and polyamide on the surface for the stabilization which even can decrease the water flux. Still, PVA is an imperatively necessary component for the preparation of the PA-CNT-PVA membranes because it can prevent the detachment of the CNTs.

Table 5-2. Water flux and salt rejection of the PA, LFC-1, PA-PVA and PA-CNT-PVA membranes tested by cross-flow filtration (2,000 ppm of NaCl solution, 15.5 bar of pressure and 500 ml min^{-1} of cross-flow rate).

	CNT[a]	PVA[a]	Water flux [LMH]	Salt rejection [%]
PA	-	-	35.4 ± 2.4	94.6 ± 1.5
LFC-1	-	-	37.8 ± 1.6	97.1 ± 0.9
PA-PVA0.2	-	0.2	34.4 ± 3.8	95.8 ± 2.2
PA-PVA0.5	-	0.5	28.9 ± 3.7	96.9 ± 1.7
PA-PVA1.0	-	1.0	(5.4 ± 2.7)[b]	(98.6 ± 1.4)[b]
PA-CNT0.1-PVA0.2	0.1	0.2	33.8 ± 2.1	96.5 ± 1.9
PA-CNT0.2-PVA0.2	0.2	0.2	32.4 ± 2.1	96.1 ± 1.1
PA-CNT0.4-PVA0.2	0.4	0.2	34.1 ± 2.5	95.6 ± 1.2
PA-CNT0.2-PVA0.2	0.2	0.2	32.4 ± 2.1	96.1 ± 1.1
PA-CNT0.2-PVA0.5	0.2	0.5	29.8 ± 2.0	96.8 ± 1.3
PA-CNT0.4-PVA1	0.2	1.0	(4.2 ± 1.0)[b]	(98.4 ± 0.5)[b]

[a]concentration of solution for preparation of membranes.

[b]obtained after 5h of the filtration test.

It was also noted that the water flux and salt rejection values of the PA membrane were smaller than those of LFC-1, the commercial RO membrane. Since the LFC-1 membrane was known to be prepared using several ingredients to increase the water flux and salt rejection, direct comparison of the PA membrane and LFC-1 might not be fair. The water flux values of most of the PA-CNT-PVA membrane are also smaller than that of the LFC-1 membrane, while the salt rejection values of the PA-CNT-PVA membrane were quite similar to that of LFC-1. Although the water filtration performances of the PA-CNT-PVA membranes are not better than that of the LFC-1 membrane, antibiofouling properties and long term stability for the feed solutions containing microorganisms were found to be much superior to those of the LFC-1 membrane, as shown in the next part of this manuscript.

5.2.4. Antibiofouling properties of PA-CNT-PVA membrane

The biofouling resistance of the membranes was evaluated from cross-flow membrane filtration using the feed solution containing *P. aeruginosa* PAO1 as a model biofoulant. The initial water flux values of all the membranes were controlled with 40 LMH by adjusting the feed pressure because one of the major driving forces inducing the biofouling is the water flow velocity passing on/through the membranes [88, 136]. Normalized water permeation flux

variations of the PA, PA-PVA, PA-CNT-PVA, and LFC-1 membranes are shown in Figure 5-7. The PA, PA-PVA membranes showed a significant flux decline after 15 h from the initial filtration, and a further flux-decline was observed after the 24 h of the filtration test. Similar flux-decline behaviour was observed for the LFC-1 membrane. The large flux decline of PA, PA-PVA, and LFC-1 membranes could originate from the interactions between the membrane surface and microorganisms as well as active biofilm formation by the *P. aeruginosa* PAO1 fouled on the membrane surfaces. In contrast, such large flux decline was not observed from all the PA-CNT-PVA membranes prepared using different CNT and PVA solutions. Therefore, the incorporation of CNTs on the surface of polyamide active layer can impart superior antibiofouling properties to the PA membrane.

It was also found that 0.2 wt% of CNT-dispersed solution was found to be the optimum concentration for the smallest flux-decline, as shown in the Figure 5-7(a). 0.1 wt% of CNT-dispersed solution might not be enough amount of CNT on the polyamide layers to impart the effective antibiofouling properties. The CNT-dispersed solution concentration larger than 0.2 wt% was also not as effective as 0.2 wt%. For example, when the 0.4 wt% solution was used, the flux decline was larger than when the 0.2 wt% solution was used. This could be ascribed to the formation of aggregated CNT clusters. Since CNTs are aggregated in a size larger than 1 μm, the effective antibiofouling properties of

each CNT are not possible. The effect of CNT-dispersed solution concentration on the antibiofouling properties was observed from the PA-CNT-PVA membranes prepared using 0.2 wt% of PVA solutions because the effective antibiofouling property was observed when the PVA solution concentration is smaller than 0.5 wt%, as shown in Figure 5-7(b). When the PVA concentration is larger than 0.5 wt% such as 1.0 wt%, larger flux decline was observed because thicker and denser PVA coating layer could be formed on the top of the CNT-deposited polyamide layers (Table 5-2). Then the effective antibiofouling properties by the CNTs are not possible because they are mostly covered by PVA materials. The PA-PVA1 and PA-CNT-PVA membranes prepared using 1.0 wt% of PVA solution also showed a little water flux value although the salt rejection value was the highest, due to the formation of thick PVA coating layers. As mentioned previously, if the PVA solution concentration is smaller than 0.2 wt% such as 0.05 wt%, the amount of PVA is not enough to stabilize the CNTs on the polyamide layers by the crosslinking reaction. Therefore, the maximum antibiofouling property of the PA-CNT-PVA membranes could be obtained when sufficient amount of CNTs were more or less uniformly dispersed on the polyamide layer and when they were cross-linked using a proper amount PVA (0.2 to 0.5 wt% of PVA solution). In addition, it was found that the PVA concentration did not affect much, if any, the antibiofouling properties of the PA-PVA membranes.

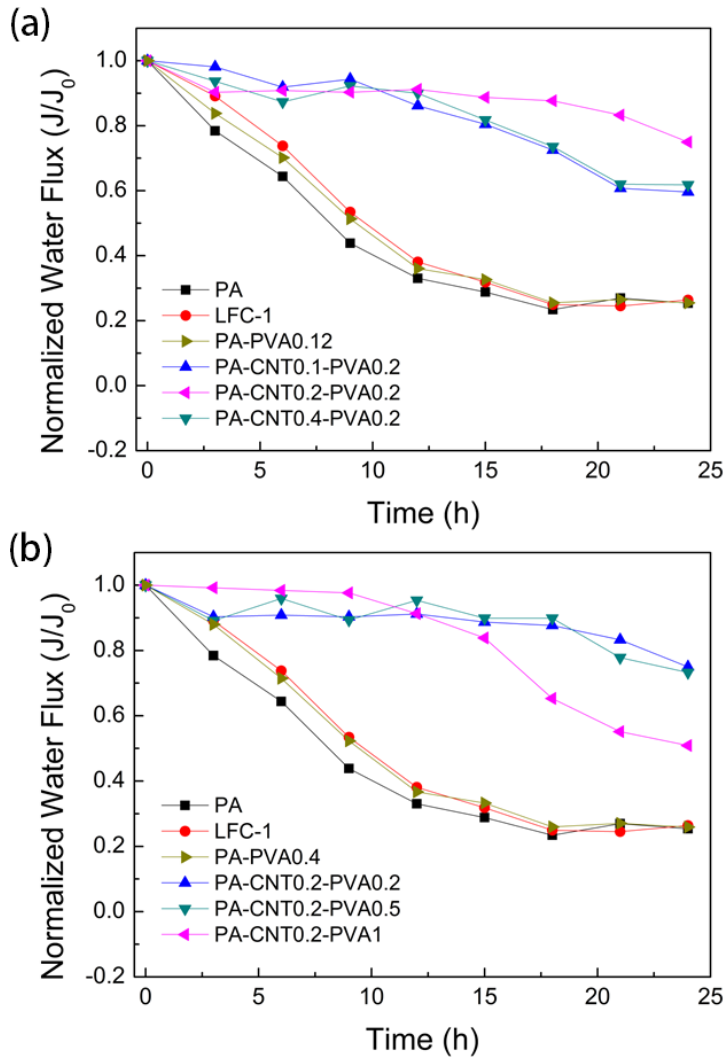

Figure 5-7. Water flux variations of PA, PA-CNT-PVA, and LFC-1 membranes with time obtained by cross-flow filtration using the feed solutions containing *P. aeruginosa* PAO1 at 15.5 bar of pressure and 270 mL min^{-1} of cross-flow rate.

Antibiofouling morphology of the PA, PA-PVA, PA-CNT-PVA, LFC-1 membranes could be confirmed by CLSM after the biofouling experiment, as shown in Figure 5-8. In the CLSM images, green and red spots represent live and dead cells attached on the membrane surfaces, respectively. The PA, PA-PVA and LFC-1 membranes show dense and thick biofouled layers with large numbers of live *P. aeruginosa* PAO1 cells and with few red spots from the dead cells formed during the filtration, while the PA-CNT-PVA membrane shows a thin biofouling layer with small numbers of the live cells. The dead cells (red spots) are not easily observed possibly because dead cells do not have enough active forces and/or vitality to be attached on the membrane surfaces, then they could be easily detached by the water flow of feed solute ion with the high pressure applied during the water filtration test. The CNTs exposed on the membrane surfaces inactivate microorganisms, and eventually they are detached by the water flow during the filtration test.

The antimicrobial properties of the PA-CNT-PVA membrane were further studied by the cell viability test (Figure 5-9). The cell viability of the PA-CNT-PVA membrane was found to be less than 1%, while those of PA, PA-PVA and LFC-1 membranes were larger than 80%. CNTs have been known to have the antimicrobial properties by damaging the membrane of microorganisms, disrupting the metabolic pathway, applying oxidative stresses, and/or changing surface roughness [130, 134, 137]. In addition to these possible biocidal or

antibiofouling mechanisms by the CNTs, the increase of the hydrophilicity might increase the antibiofouling property of the PA-CNT-PVA membrane compared with PA and PA-PVA membranes. The contact angle value measured by the captive bubble method of the PA-CNT-PVA membrane was found to be smaller than that of PA membrane. The smaller contact angle indicates the increased hydrophilicity in the captive bubble method as shown in Figure 5-10 [81]. Although the contact angle value of PA-CNT-PVA membrane was smaller than that of PA membrane, it is close to or even slightly larger than that of PA-PVA membrane. Since PA and PA-PVA membranes do not have any antibiofouling property, the increase of hydrophilicity on PA-CNT-PVA membrane should not affect to the antibiofouling properties in this experiments, as previously reported [88]. Since there have been reports that surface roughness could change the antifouling properties of the membranes [126, 138], the surface roughness of the membranes were measured by AFM and the results are shown in Table 5-3 and Figure 5-11. All the membranes showed a nano-scale surface roughness, a well-known surface morphology of conventional PA membranes from the interfacial polymerization [126, 139], and their root mean square (RMS) roughness were in the range from 43 to 80 nm. Although the coating processes increases the surface roughness, it is not enough to affect the antibiofouling properties as reported by others [140, 141]. Although we do not have a very clear explanation for the excellent biocidal properties of the PA-CNT-PVA membranes in this study, it is

clear that the effective biocidal properties of CNTs can improve the membrane performance during the water treatment.

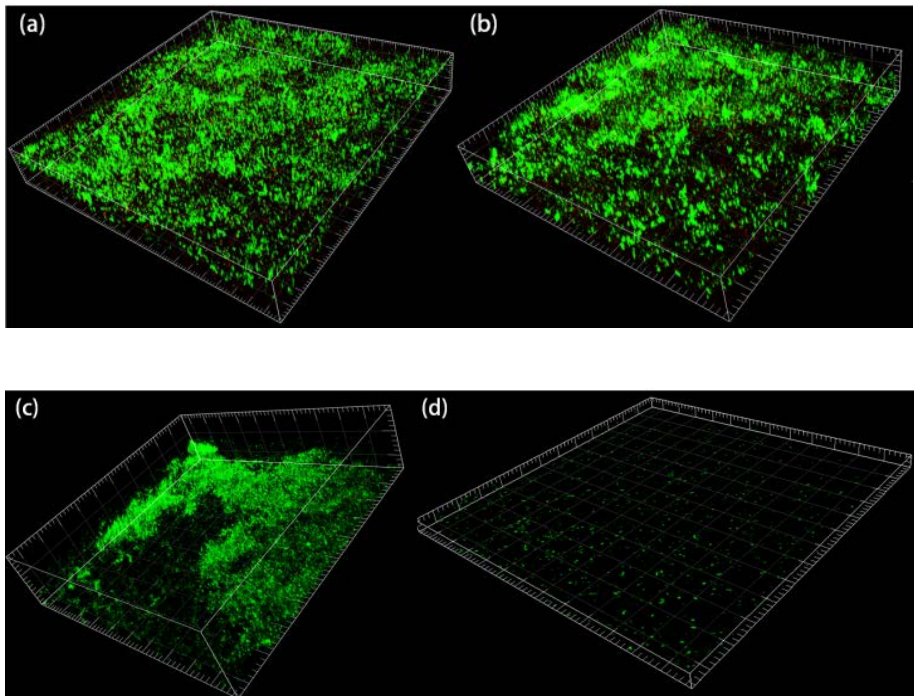

Figure 5-8. CLSM images of (a) PA, (b) LFC-1, (c) PA-PVA0.4, and (d) PA-CNT0.2-PVA0.2 membranes obtained after 24 h cross-flow test using the feed solutions containing *P. aeruginosa* PAO1.

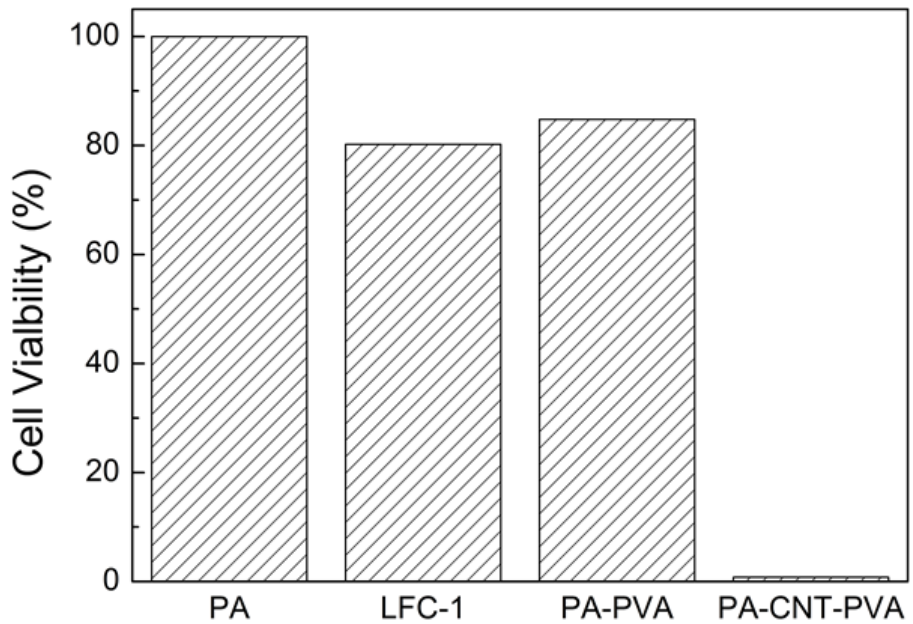

Figure 5-9. Cell viability tests for PA, LFC-1, PA-PVA0.4 and PA-CNT0.2-PVA0.2 membranes, where PA membrane is used as the control standard.

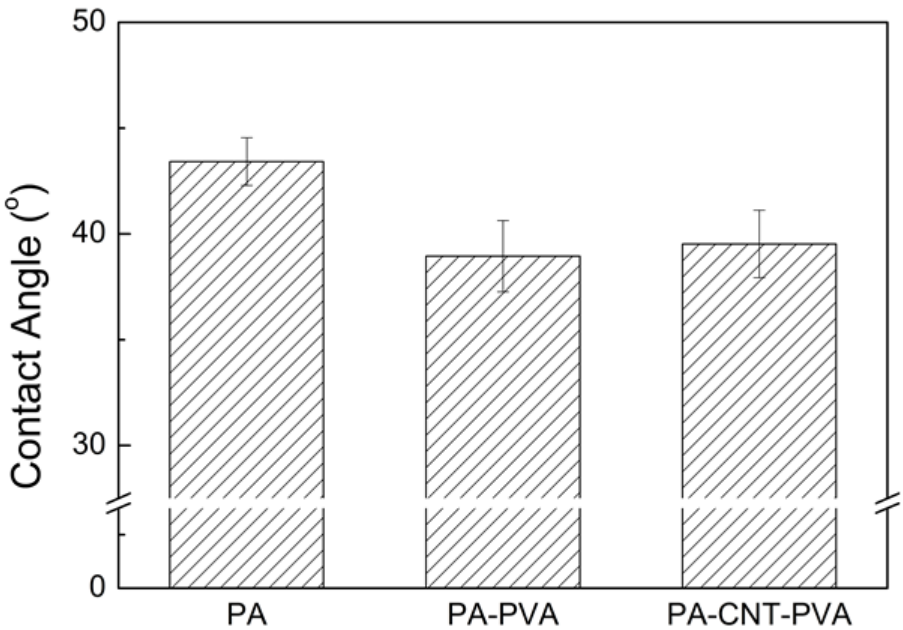

Figure 5-10. Contact angles of PA, PA-PVA0.4, and PA-CNT0.2-PVA0.2 membranes measured by captive bubble method.

Table 5-3. The root mean square (RMS) roughness of PA, PA-PVA0.4, LFC-1, and PA-CNT0.2-PVA0.2 membranes.

	RMS (nm)
PA	43.7 ± 2.2
PA-PVA0.4	57.9 ± 2.9
PA-CNT0.2-PVA0.2	64.65 ± 1.5
LFC-1	80.4 ± 0.70

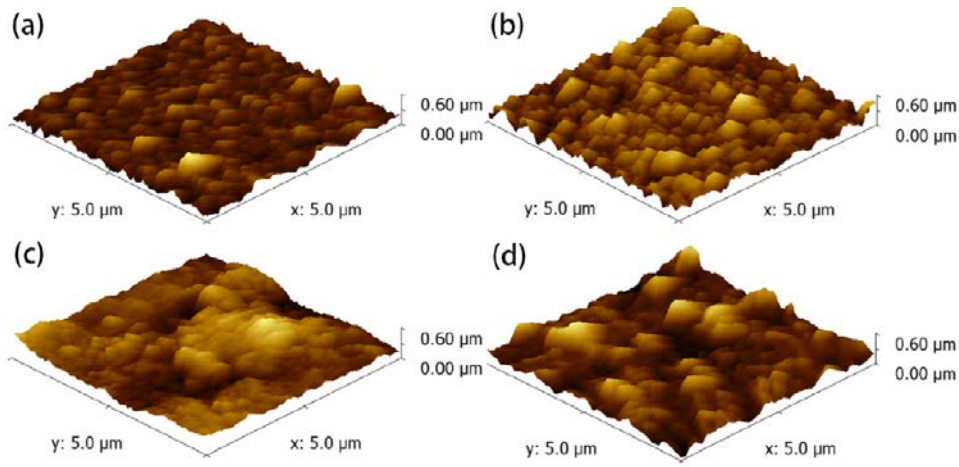

Figure 5-11. AFM images of (a) PA, (b) PA-PVA0.4, (c) PA-CNT0.2-PVA0.2, and (d) LFC-1 membranes.

5.3. Conclusion

Polyamide membranes with CNTs and PVA coating (PA-CNT-PVA membrane) exhibited the excellent antibiofouling properties in a real filtration system. It was also found that there are optimum amounts of CNTs and PVA that give the reasonably high water flux and salt rejection values with accompanying high antibiofouling properties and durability. When large amounts of CNT were used, the antibiofouling property of the PA-CNT-PVA membrane decreased because of the formation of aggregated CNT clusters. When a large amount of PVA was used, the antibiofouling property was diminished due to a very dense and thick PVA layer, while CNT detachment was readily observed when very small amounts of PVA were used. The high antibiofouling properties of PA-CNT-PVA membrane were ascribed to the antimicrobial properties of the CNTs, confirmed by the CLSM images of biofouling membrane and cell viability test. Our results clearly show that properly prepared PA-CNT-PVA membranes can manifest the antibiofouling properties for real filtration system with microorganisms without scarifying the water flux and salt rejection properties much if at all. This work will undoubtedly contribute to the latest efforts to develop the RO membranes with the antibiofouling properties and also shows the new antibiofouling test method for the water treatment membranes.

6. Evaluation of CNT embedded RO Membrane: Surface Properties, Performance Characteristics and Fouling Behaviors

6.1. Theory

6.1.1. Water flux and salt rejection

Water flux (J_w) was calculated using Eq. 6-1 and salt rejection (R) was calculated using the following Eq. 6-2:

$$J_w = \Delta V / (a \times \Delta t) \quad \text{(Eq. 6-1)}$$

where ΔV is the volume of the collected permeate, a is the effective area of membrane surface, and Δt is the time between two weight measurements.

$$R = (1 - C_p / C_f) \times 100\ \% \quad \text{(Eq. 6-2)}$$

where C_p is the salt concentration in permeate and C_f is the salt concentration in feed. The salt concentrations were measured using conductivity meter (Horiba, F-54 BW, Japan).

6.1.2. Specific energy consumption

An specific energy consumption (SEC) of both the CNT embedded RO membrane and the polyamide RO membrane were calculated from membrane performance such as water flux and salt rejection. The energy consumption for CNT embedded RO membrane was evaluated from the SEC which defined as the electrical energy required to produce a cubic meter of permeate. It was assumed that pump efficiency was 100% and only the pump work was used for the electrical energy in this study. Then, the SEC can be described as follows.

$$SEC = W_{pump} / Q_p \quad \text{(Eq. 6-3)}$$

where W_{pump} is the rate of work done by pump and Q_p is the permeate flow rate.

$$W_{pump} = \Delta P \times Q_f \quad \text{(Eq. 6-4)}$$

where ΔP is the difference between hydraulic pressure and osmotic pressure and Q_f is the volumetric feed flow rate. Because Q_f / Q_p in lab-scale cross-flow system is very lower than the pratical RO system, Q_f / Q_p was assumed to 50% as usual. Therefore, SEC can be described in Eq. 6-5.

$$SEC = 2 \times \Delta P \quad \text{(Eq. 6-5)}$$

In this study, water permeability (A) and salt permeability (B) were attained by solution-diffusion model and then, ΔP was calculated with assuming that

constant water flux was producted based on the A value (see Appendix).

6.1.3. Resistance-in-series model

The resistance-in-series model (Eq. 6-6) was applied to evaluate fouling tendency of the CNT embedded RO membrane [142, 143].

$$J_0 = \Delta P / \mu \times (R_m + R_r + R_{ir}) \quad \text{(Eq. 6-6)}$$

where J_0 is a pure water flux, μ is the dynamic viscosity, R_m is the membrane resistance, R_r is the reversible fouling resistance, and R_{ir} is the irreversible fouling resistance.

6.1.4. Solution-diffusion model

The water permeability constant (A; LMH/bar) and salt permeability constant (B; LMH) were calculated using Eq. 6-7 and Eq. 6-8, respectively from solution-diffusion model [144].

$$A = J_w / \Delta P \quad \text{(Eq. 6-7)}$$

where J_w is water flux and ΔP is the difference between hydraulic pressure and osmotic pressure (π).

$$B = J_s / (C_p - C_f) \quad \text{(Eq. 6-8)}$$

where J_s is salt flux attained by $J_w \times C_f$.

6.1.5. Total Production

A total production was obtained by the integration of the water flux as functions of time (Eq. 6-9). It was assumed that the initial permeate flux was fixed as 15 LMH in condition of 35,000 mg L^{-1} of artificial sea water.

$$Q_{total} = \int_0^t \frac{dQ_p}{dt} \quad \text{(Eq. 6-9)}$$

6.2. Materials & Methods

6.2.1. Materials

Multi-walled carbon nanotubes were purchased from Nanocyl (Belgium). The average diameter and average length of CNT are 10 − 20 nm and 10 − 20 μm, respectively as provided by the manufacturer. Sulfuric acid (H_2SO_4, 98%), nitric acid (HNO_3, 60%), and isopropyl alcohol (IPA) were supplied from Daejung Chemicals (Republic of Korea). *m*-phenylenediamine (MPD, 99%), trimesoyl chloride (TMC, 98%), sodium chloride (NaCl, 99.5%), sodium citrate (99%), artificial sea salt, and ethylenediaminetetraacetic acid (EDTA, 99.4%) were supplied from Sigma Aldrich (U.S.A.). *n*-Hexane (95%) was received from Samchun Chemicals (Republic of Korea). Deionized (DI) water was obtained from water purification system (Mili-Q, Millipore, U.S.A.), having a resistivity of 18.3 mΩ cm. Polysulfone (Psf) membranes as a supporting membrane for RO membrane were kindly received from Woongjin Chemicals (Republic of Korea). LFC-1 (Hydranautics a Nitto Denko, Japan) was used as a commercial RO membrane. A carbenicillin-resistant derivate of *Pseudomonas aeruginosa* PAO1 tagged with the green fluorescent protein (GFP) (Center for Biofilm Engineering, Montana State University, Bozeman, U.S.A.) and tryptic soy broth (Bacto, Franklin Lakes, U.S.A) were used as a model bacterial strain and a nutrient of bacteria, respectively for biofouling experiment.

6.2.2. Preparation of CNT embedded RO membrane

The CNTs were modified using acid mixture of sulfuric acid and nitric acid (3:1 volume ratio) with sonication and heat treatment for dispersion [128]. CNT embedded RO membrane was fabricated by following steps; 1) IPA treatment of Psf membrane for 10 min, 2) stabilization of Psf membrane by DI water for 3 h, 3) soaking Psf membrane into 3.0 wt% MPD and 0.001 wt% CNT solution in DI water for 3 h, 4) removal excess MPD solution onto the surface of Psf membrane by rolling a rubber roller, 5) reaction with 0.1 wt% TMC solution in *n*-hexane for 1 min, 6) washing excess TMC solution by hexane solution, and 7) heat treatment in 100°C oven for 5 min. These conditions were optimized and more details are described in our previous study [145].

6.2.3. Membrane characterizations

Surface properties such as hydrophilicity, charge and roughness of the membranes were analyzed by contact angle analyzer (KRÜSS, DSA100, Germany), electrophoretic light scattering spectrometer (ELS-Z2,Ostuka Electronic, Tokyo, Japan), and atomic force microscopy (AFM; SIS, Pucostation, Germany), respectively. Captive bubble method for measuring contact angles was chosen for better accuracy as reported in our previous study [81]. Zeta

potential measurement for membrane surface charge was performed in 1 mM KCl solution with polystyrene latex particles of which surface charge is defined as 0. Membrane characterizations were performed with at least three samples and the average values were reported in this study.

Cross-sectional images of both the CNT embedded RO membrane and the polyamide RO membrane were observed by TEM (LIBRA 120, Carl Zeiss, Germany). The membrane samples were prepared by embedding in in Spur resin, cutting to approximately 60 – 70 nm thick sections by an ultramicrotome (MTX, RMC) and then, placing on TEM grids. The sections were observed at an accelerating voltage of 120 kV. In addition, surface morphologies of the membranes were observed by a field emission scanning electron microscopy (FE-SEM, JSM-6701F, JEOL).

6.2.4. Performance measurement

Membrane performances such as water flux and salt rejection were obtained by lab-scale cross-flow RO membrane test unit [88]. The effective membrane areas were 3.3 × 6.8 cm^2 with the 0.3 cm of channel height. The pressure was maintained at the ranges from 15.5 bar (225 psi) to 55 bar (809 psi) with the ranges of the feed solution from 2,000 mg L^{-1} to 35,000 mg L^{-1} of NaCl solution.

Cross-flow velocity at the membrane surface was 700 mL min^{-1} at 25°C. Water flux was measured by weighing the permeate after the membranes were compressed for 1 h at each pressure for the various concentration of the feed solution.

6.2.5. Fouling experiments

Two kinds of fouling experiment were performed to evaluate fouling behaviors of the CNT embedded RO membrane in a lab-scale cross-flow membrane system. Biofouling occurrence was performed with *P.aeruginosa* PAO1 GFP for 24 h. Each membranes was conditioned with 10 mM NaCl, 10 mM sodium citrate and 0.1% tryptic soy broth solution for 6 h and then, biofouled with *P.aeruginosa* PAO1 (initial concentration: ~1×10^7 CFU mL^{-1}) for 24 h. The initial flux, cross-flow rate, and temperature were fixed at 40 LMH, 250 mL min^{-1}, and 25°C, respectively. The decrease of water flux and confocal laser scanning microscopy (CLSM; Nikon 90i, Japan) with staining by the BacLight live/dead kit (Molecular Probes, Eugene, U.S.A) were used as criteria of biofouling occurrence.

Another fouling was performed with 35,000 mg L^{-1} of artificial sea water for 138 h. The conditions for the initial flux, cross-flow rate, and temperature were

fixed at 15 LMH, 700 mL min^{-1}, and 25°C, respectively. Membrane fouling proceeded with 96 h of membrane fouling, cleaning with DI water for 1 h, 18 h of membrane fouling, cleaning with 5 mM EDTA solution at pH 11 for 1 h, and 22 h of membrane fouling. Membrane compaction with DI water for 18 h was run before both the fouling experiments. Based on the result of this experiment, the resistances for the membranes, reversible fouling and irreversible fouling were calculated by the resistance-in-series model and the total productivity (Q_{total}) were attained.

6.3. Results and Discussion

6.3.1. Membrane characteristics and surface properties.

Schematics of the CNT embedded RO membrane and the polyamide RO membrane are illustrated in Figure 6-1. The difference between the CNT embedded RO membrane and the polyamide RO membrane is the presence of CNTs in polyamide layer, which can be made by interfacial polymerization process. In the CNT embedded RO membrane, CNTs are located in polyamide layer to add modified CNTs into MPD solution during interfacial polymerization process, observed by cross-section TEM images (Figure 6-2). These CNTs can be attributed to enhance the water flux by fast water transport through CNTs and/or shortening the pathway of water transport. Two pathways for water transport through CNTs in the polyamide layer were experimentally explained such as a diffusion through continuous polyamide layer and a fast diffusion through the inner wall of CNTs [146].

Table 6-1 shows the characteristics of the CNT embedded RO membrane in comparison with the polyamide RO membrane and the commercial RO membrane. In membrane composition, 3.0 wt% of MPD solution with 0.001 wt% of modified CNTs were used for CNT embedded RO membrane, while the best performance of the polyamide RO membrane was obtained with 2.0 wt% of MPD solution. The concentration of MPD and CNTs were optimized in our

previous study [145]. In terms of surface properties, the CNT embedded RO membrane has similar hydrophilicity and surface charges, compared to the polyamide RO membrane and the commercial RO membrane. These results are different from the literature which reported that adding modified CNTs in polymer makes the surface more hydrophilic [96]. Because CNTs were barely located on the top surface in this study (Figure 6-3), surface hydrophilicity and surface charges of the CNT embedded RO membrane were changed little. On the other hand, the surface roughness of the CNT embedded RO membrane became much smoother (18.5 nm) than that of the polyamide RO membrane (54.1 nm) and that of the commercial RO membrane (80.4 nm). This smoother surface of the CNT embedded RO membrane implies that the CNT embedded RO membrane has lower fouling potential than others [11].

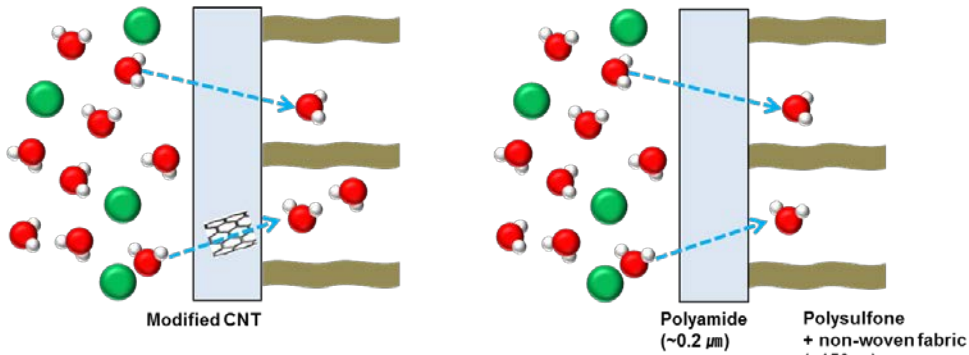

(a) (b)

Figure 6-1. Schematics of (a) CNT embedded RO membrane and (b) polyamide RO membrane.

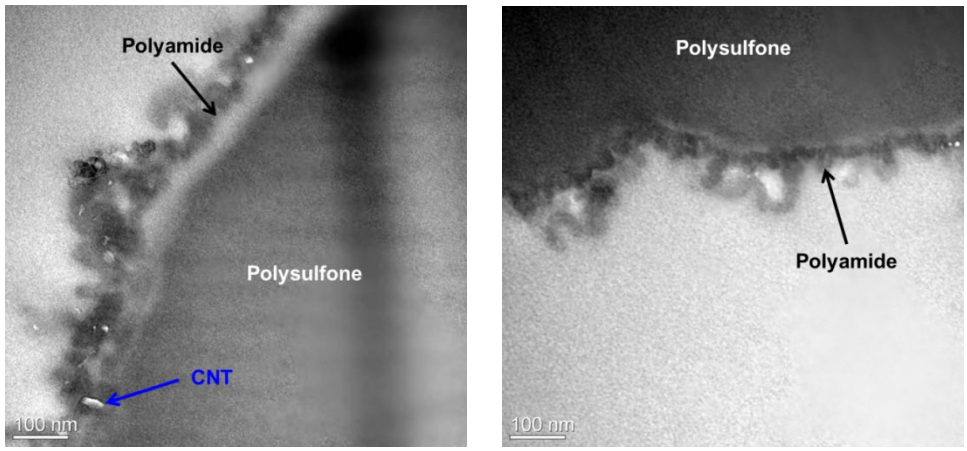

(a) (b)

Figure 6-2. Cross-section TEM images of (a) CNT embedded RO membrane and (b) polyamide RO membrane.

Table 6-1. Membrane composition and surface properties of the CNT embedded RO membrane compared to the polyamide RO membrane and commercial RO membrane.

		CNT embedded RO	Polyamide RO	Commercial RO (LFC-1)
Membrane composition	% of MPD and TMC	3.0 wt% and 0.1 wt%	2.0 wt% and 0.1 wt%	unknown
	% of CNT	0.001 wt%	-	-
Surface properties	Contact angle (°)[a]	45.7 ± 0.6	47.2 ± 0.8	45.6 ± 1.4
	Zeta potential (mV)[b]	-18.5 ± 3.6	-17.2 ± 0.9	-16.8 ± 1.4
	Roughness (nm)[c]	18.5 ± 6.4	54.1 ± 3.7	80.4 ± 0.7

[a]: measured by captive bubble method [81].

[b]: measured at the condition of pH 7.

[c]: root mean square (RMS) roughness.

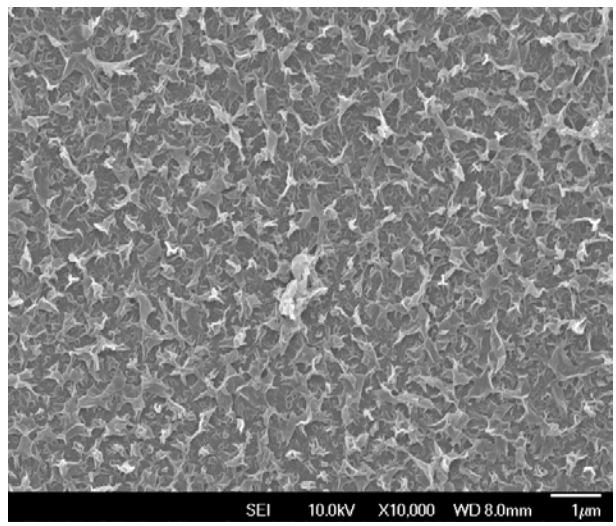

(a)

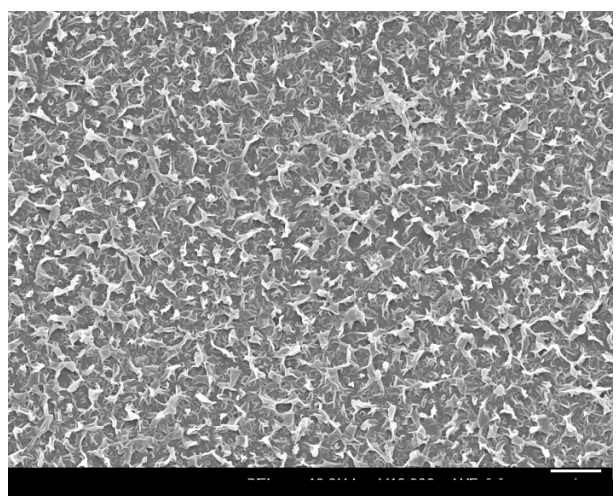

(b)

Figure 6-3. SEM images of top surface on (a) CNT embedded RO membrane and (b) polyamide RO membrane.

6.3.2. Performance characteristics

The performance of the CNT embedded RO membrane was evaluated in conditions with various concentration of NaCl solution and different applied pressures. Figure 6-4 the effects of (a) NaCl concentration on water flux and NaCl passage and (b) applied pressures on pure water flux of CNT embedded RO membrane compared to polyamide RO membrane and commercial RO membrane (LFC-1). As shown in Figure 6-4(a), water fluxes were decreased as NaCl concentration was increased because the concentration polarization was also increased at higher concentration of NaCl solution [147]. Interestingly, as NaCl concentration was increased, the flux enhancement of CNT embedded RO membrane was decreased. It might be explained by the adsorption ability of CNTs. Ions which were passing through CNTs can be adsorbed onto the walls of CNTs and eventually disturb the water passage. Additionally, water permeability (A value) and salt permeability (B value) were calculated to obtain the specific energy consumption (SEC) as shown in Table 6-2.

Figure 6-4(b) shows the effect of applied pressure on water flux through the CNT embedded RO membrane compared to the polyamide RO membrane and the commercial RO membrane. As the applied pressure increased, water fluxes of both the polyamide RO membrane and the commercial RO membrane were decreased while the CNT embedded RO membrane maintained the water flux. In

general, water flux of RO membrane tends to decrease with increasing applied pressure because of a membrane compaction effect [148]. On the other hand, two possibilities for maintaining the water flux in the CNT embedded RO membrane are available as follows. One is accelerated water transport through CNTs at higher pressure which is over the resistance for the entrance at the ends of CNTs. Another possibility is an improved mechanical strength to reduce the membrane compaction effect. It is well-known that adding CNTs in polymer composite enhances the mechanical property [149] and the mechanical strength of CNT embedded RO membrane was reported that is stronger than polyamide RO membrane and commercial RO membrane (LFC-1) in our previous study [145].

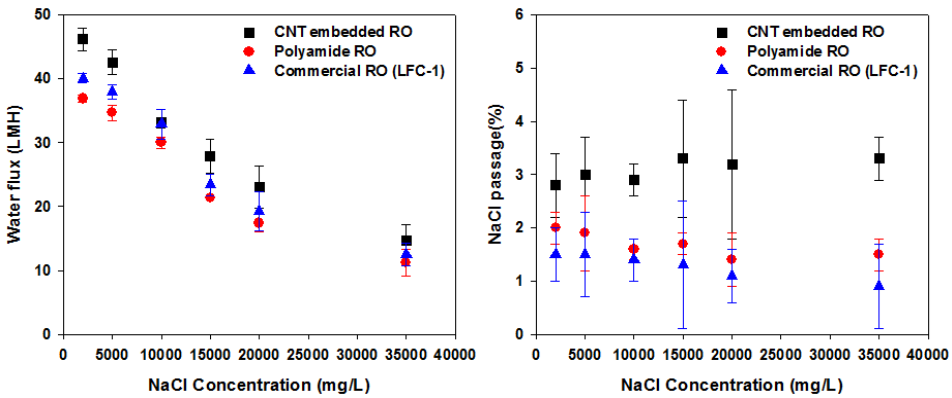

(a)

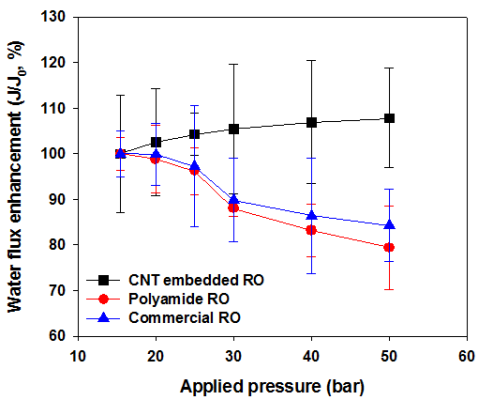

(b)

Figure 6-4. Effects of (a) NaCl concentration on water flux and NaCl passage and (b) applied pressures on pure water flux of the CNT embedded RO membrane compared to the polyamide RO membrane and the commercial RO membrane (LFC-1).

Table 6-2. Water permeability (A) and salt permeability (B) in various NaCl concentration for the CNT embedded RO membrane compared to the polyamide RO membrane and the commercial RO membrane.

NaCl conc. ($mg\ L^{-1}$)	Osmotic pressure (bar)	Applied pressure (bar)	CNT embedded RO membrane		Polyamide RO membrane		Commercial RO membrane	
			A (LMH/bar)	B (LMH)	A (LMH/bar)	B (LMH)	A (LMH/bar)	B (LMH)
2,000	1.5	15.5	3.31 ± 0.13	1.33 ± 0.28	2.64 ± 0.04	0.75 ± 0.11	2.87 ± 0.04	0.61 ± 0.20
5,000	3.9	20.0	2.64 ± 0.12	1.32 ± 0.30	2.15 ± 0.07	0.67 ± 0.24	2.35 ± 0.05	0.58 ± 0.31
10,000	7.7	25.0	1.92 ± 0.05	0.99 ± 0.10	1.74 ± 0.05	0.49 ± 0.06	1.91 ± 0.02	0.47 ± 0.13
15,000	11.6	30.0	1.52 ± 1.41	0.95 ± 0.31	1.16 ± 0.02	0.37 ± 0.04	1.28 ± 0.07	0.30 ± 1.28
20,000	15.5	35.0	0.94 ± 0.13	0.76 ± 0.33	0.71 ± 0.06	0.25 ± 0.09	0.79 ± 0.02	0.21 ± 0.10
35,000	27.1	55.0	0.64 ± 0.11	0.50 ± 0.06	0.49 ± 0.09	0.17 ± 0.03	0.55 ± 0.03	0.11 ± 0.13

Figure 6-5 shows a comparison of the specific energy consumption (SEC) among the CNT embedded RO membrane, the polyamide RO membrane and the commercial RO membrane as a function of various concentration of NaCl solution, which assumed that a permeate flux was fixed at 30, 40, 50 LMH. Note that the SEC in this study is a little low because only pump work was considered. As shown in Figure 6-5, the SEC was increased with higher concentration of NaCl solution. The CNT embedded RO membrane showed lower SEC than the polyamide RO membrane due to its higher water flux. For example, the SEC for 30 LMH and 40 LMH of the permeate flux in the polyamide membrane was similar to that for 40 LMH and 50 LMH of the permeate flux in the CNT embedded RO membrane. This result indicates that lower energy is consumed for the CNT embedded RO membrane when the same amounts of the product is required.

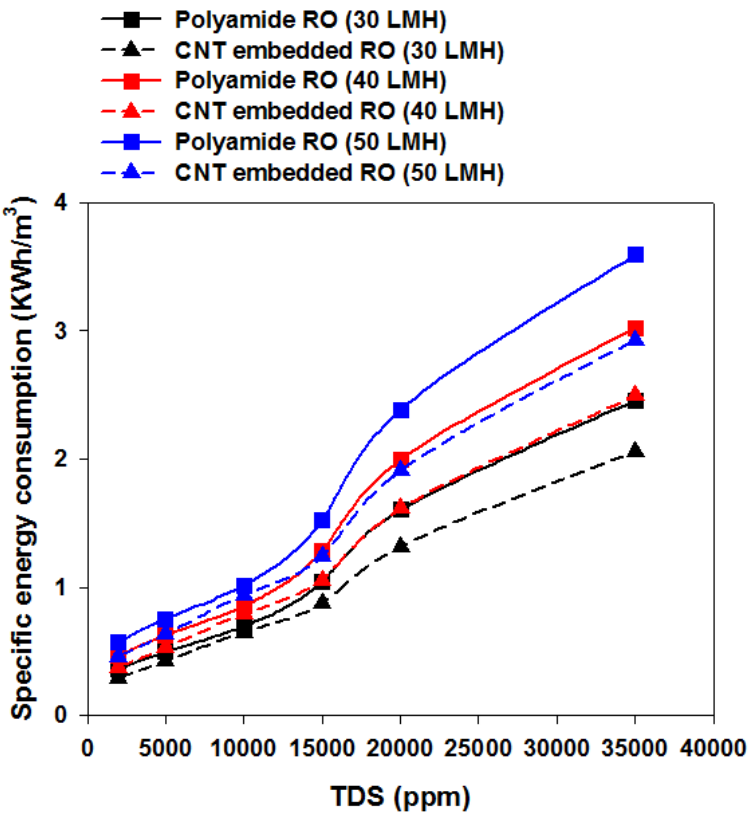

Figure 6-5. A comparison of the specific energy consumption (SEC) among the CNT embedded RO membrane, the polyamide RO membrane and the commercial RO membrane as a function of various concentration of NaCl solution. (Assumption: permeate flux was fixed at 30, 40, and 50 LMH).

6.3.3. Fouling behaviors

Figure 6-6 illustrates a biofouling behaviors of the CNT embedded RO membrane; (a) permeate flux decline and (b) CLSM images of *P.aeruginosa* PA01 GFP biofilms formed on the membrane surfaces after 24 h of biofouling occurrence (left: CNT embedded RO membrane, middle: polyamide RO membrane, and right: commercial RO membrane (LFC-1)). As shown in Figure 6-6(a), the permeate flux decline of the CNT embedded RO membrane was 8 – 11% less than that of the polyamide RO membrane and that of the commercial RO membrane. This negligible effect was unexpected because CNTs are known to have a relatively strong anti-microbial property [61, 70]. Biofilm formation on the CNT embedded RO membrane, observed by CLSM with staining, was also similar to the polyamide RO membrane and commercial RO membrane (Figure 6-6(b)). These results can be explained by little changes of the surface property (Table 6-1) and by the location of CNTs in polyamide layer (Figure 6-3). Only the smoother surface might be attributed to resist biofouling occurrence a little and CNTs, barely located in the top surface of the polyamide layer, were not affected to the biofouling occurrence. To maximize the anti-biofouling property for the CNT embedded RO membrane, CNTs should be exposed to the surface to possibly contact with the microorganisms. For example, deposition of the oxidized CNTs on the polyamide layer [128] and covalently bonded CNTs on the

polyamide layer [130] showed a better anti-biofouling property in the literatures.

Figure 6-7 the changes of water flux for the CNT embedded RO membrane compared to the polyamide RO membrane by 35,000 mg L^{-1} of artificial sea water for 138 h. The water flux of the CNT embedded RO membrane was less decreased than the polyamide RO membrane due to the smoother surface. During the two times of cleaning by DI water and 5 mM EDTA solution at pH 11, the water fluxes of the CNT embedded RO membrane were recovered to 67.4% and 80.0% while the polyamide RO membrane recovered to 62.5% and 75.4%, respectively. Furthermore, the resistances were calculated by resistance-in-series model as shown in Table 6-3. It appears that the CNT embedded RO membrane has less resistances than the polyamide RO membrane. Especially, irreversible fouling resistance of the CNT embedded RO membrane was about 40% less than polyamide RO membrane while others were 20% less. This low fouling resistance of the CNT embedded RO membrane enhances the recovery efficiency for the cleaning process.

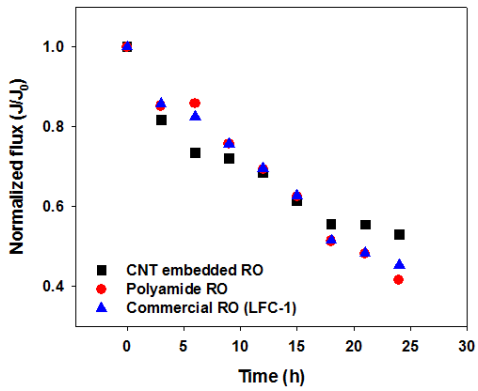

(a)

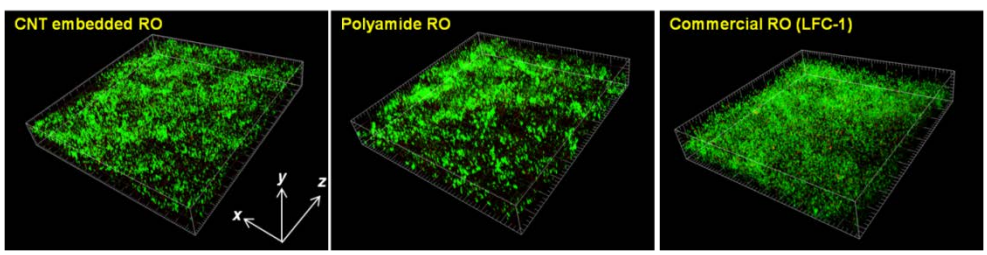

(b)

Figure 6-6. Biofouling behaviors of CNT embedded RO membrane; (a) permeate flux decline (feed solution: 10 mM NaCl, 10 mM sodium citrate, 0.1% TSB solution with ~1 × 10^7 CFU/mL of *P.aeruginosa* PA01 GFP, initial permeate flux: 40 LMH, cross-flow rate: 240 mL min^{-1}, temperature: 25°C)and (b) CLSM images of *P.aeruginosa* PA01 GFP biofilms formed on the membrane surfaces after 24 h of biofouling occurrence (left: CNT embedded RO membrane, middle: polyamide RO membrane, and right: commercial RO membrane (LFC-1)).

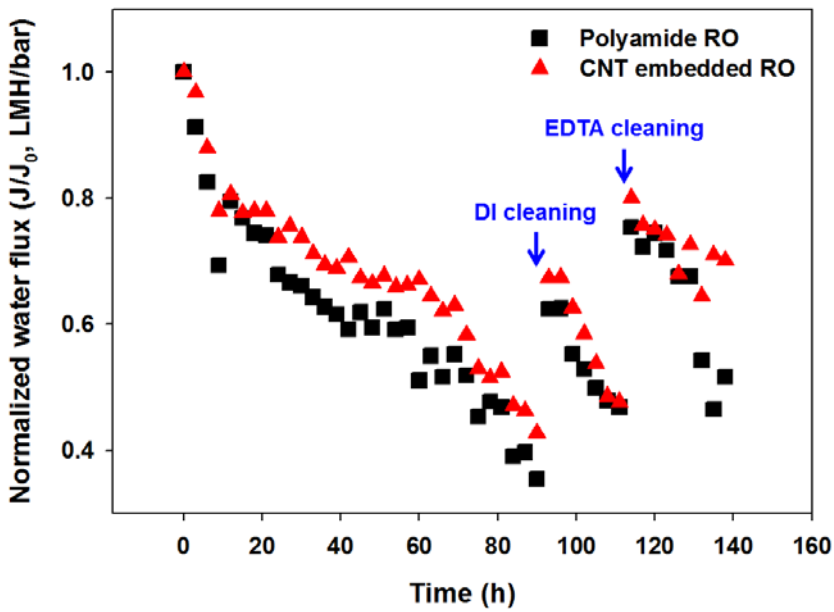

Figure 6-7. The changes of water flux for the CNT embedded RO membrane compared to the polyamide RO membrane by 35,000 mg L^{-1} of artificial sea water for 138 h. Initial permeate flux, cross-flow rate, and temperature were fixed at 15 LMH, 700 mL min^{-1}, and 25°C, respectively. Cleanings were performed two times by deionized water after 96 h and 5 mM EDTA solution at pH 11 after 120 h.

Table 6-3. Resistances calculated by resistance-in-series model.

	Membrane resistance (R_m)	Reversible fouling resistance (R_r)	Irreversible fouling resistance (R_{ir})
CNT embedded RO	1.4×10^{13} cm^{-1}	1.7×10^{13} cm^{-1}	6.6×10^{12} cm^{-1}
Polyamide RO	1.8×10^{13} cm^{-1}	2.2×10^{13} cm^{-1}	1.1×10^{13} cm^{-1}

6.4. Conclusion

We compared the CNT embedded RO membrane with the polyamide RO membrane and the commercial RO membrane in terms of the surface properties, performance characteristics, and fouling behaviors. The role of CNTs in the CNT embedded RO membrane is increasing water flux with slightly low salt rejection and making a smooth surface. Therefore, the CNT embedded RO membrane shows less fouling potential as well as better flux recovery by cleaning process in conditions of 35,000 mg L^{-1} of artificial sea water for 138 h although biofouling occurrence is similar with others because of little exposure of CNTs onto the surface.

By the integration of water flux until 96 h in Figure 6-7, the total product (Q_{total}) was obtained with an assumption that the effective membrane area is 10,000 m^2. As a result, the Q_{total} of the CNT embedded RO membrane (6,562m^3) is about 10% more than that of the polyamide RO membrane (5,943 m^3). In this case, the CNT embedded RO membrane can produce approximately 10% more clean water than the polyamide RO membrane. It can be improved more when the flux recovery is considered. These results suggest that the CNT embedded RO membrane is feasible to apply for high performance and fouling resistant RO membrane for brackish water. Although this study gives the fundamental information, further studies should be required for commercialization such as the

durability of CNTs in polyamide layer for water safety.

7. Conclusions

Three types of CNT membranes such as open-ended VA CNT membrane, dense-array outer-wall CNT membrane, and mixed CNT membrane were investigated in terms of water permeability, rejection property and biofouling property. CNT membranes are known to have high performance and anti-biofouling property due to fast water transport through CNT and antimicrobial property, respectively.

Open-ended VA CNT membrane was evaluated with commercial UF membrane. As a result, the open-ended VA CNT membrane showed better water permeability, showing about three times higher than the commercial UF membrane based on approximately 70,000 times faster water flow than the conventional flow under the no-slip condition. This result can occur in only hydrophilic solvent (i.e. water) while hydrophobic solvent is inversely related to the viscosity of solvent as same as the conventional flow. Also, pore size of open-ended VA CNT membrane was similar to the commercial UF membrane, which was analyzed by SEM, TEM and MWCO measurement. Due to the antimicrobial property of CNTs, open-ended VA CNT membrane has a better biofouling resistance, represented by approximately 15% less permeate flux reduction and 2 log of less bacterial attachment than UF membrane.

Dense-array outer-wall CNT membrane was developed by densification of CNT forest and post treatment such as thermal and plasma treatment. The pore diameter of dense-array outer-wall CNT membrane can readily be varied by simple mechanical compression in the range between 7 nm and 38 nm, which is attractive for various membrane applications such as sorption, sensing, optics, photovoltaics, and protein separation and so on. As a result, a decrease in the pore size of membrane results in an increase in the water permeability. The CNT wall membrane, obtained by thermal and oxygen-plasma treatments of the dense-array outer-wall CNT membrane, showed the level of 30,000 LMH at 1 bar, which is almost two orders of magnitude higher than that attainable with traditional polymer membrane. Additionally, its anti-biofouling capability is much enhanced by its ability to impede bacteria adhesion and to resist biofilm formation in order.

Mixed CNT membrane were synthesized by two ways; 1) deposition of CNTs on polyamide layer covering with PVA (PA-CNT-PVA membrane) and 2) embedding CNTs in polyamide layer (mixed CNT RO membrane). The former one is objected to fabricate a biofouling-resistant membrane. Optimum amounts of CNTs and PVA give the reasonably high water flux and salt rejection values with accompanying high antibiofouling properties and durability. PA-CNT-PVA membrane showed 30 – 40% of less flux decline for biofouling experiment than

the fabricated polyamide membrane and the commercial RO membrane. The latter one is objected to fabricate a high performance membrane. Due to about 30% enhanced water flux, mixed CNT RO membrane showed better energy efficiency than polyamide RO membrane. It also showed a less fouling potential for 140 h of artificial sea salt experiment (concentration of 35,000 mg L^{-1}) and a better flux recovery for the cleaning process. These results indicate that mixed CNT RO membrane can be applicable for high performance RO membrane.

References

[1] R.F. Service, Desalination freshens up, Science(Washington, D. C.), 313 (2006) 1088-1090.

[2] M. Elimelech, W.A. Phillip, The future of seawater desalination: Energy, technology, and the environment, Science, 333 (2011) 712-717.

[3] R. Semiat, Energy issues in desalination processes, Environmental science & technology, 42 (2008) 8193-8201.

[4] O.M. Al-Hawaj, The design aspects of rotary work exchanger for SWRO, Desalination and Water Treatment, 8 (2009) 131-138.

[5] M. Elimelech, W.A. Phillip, The future of seawater desalination: Energy, technology, and the environment, Science, 333 (2011) 712.

[6] D. Potts, R. Ahlert, S. Wang, A critical review of fouling of reverse osmosis membranes, Desalination, 36 (1981) 235-264.

[7] S.P. Nunes, K.V. Peinemann, Membrane technology, Wiley Online Library, 2001.

[8] R. Sheikholeslami, Fouling in membranes and thermal units, Balaban Desalinations, 2007.

[9] G.M. Geise, H.B. Park, A.C. Sagle, B.D. Freeman, J.E. McGrath, Water permeability and water/salt selectivity tradeoff in polymers for desalination, Journal of Membrane Science, 369 (2011) 130-138.

[10] L.F. Greenlee, D.F. Lawler, B.D. Freeman, B. Marrot, P. Moulin, Reverse osmosis desalination: Water sources, technology, and today's challenges, Water Research, 43 (2009) 2317-2348.

[11] D. Rana, T. Matsuura, Surface Modifications for Antifouling Membranes, Chem. Rev, 110 (2010) 2448-2471.

[12] Q. Li, S. Mahendra, D.Y. Lyon, L. Brunet, M.V. Liga, D. Li, P.J.J. Alvarez,

Antimicrobial nanomaterials for water disinfection and microbial control: potential applications and implications, Water Research, 42 (2008) 4591-4602.
[13] H.L. Yang, J.C.T. Lin, C. Huang, Application of nanosilver surface modification to RO membrane and spacer for mitigating biofouling in seawater desalination, Water Research, 43 (2009) 3777-3786.
[14] D. Mamadou, J.S. Duncan, N. Savage, A. Street, R.C. Sustich, Nanotechnology applications for clean water, William Andrew Publishing, 2008.
[15] M.T.M. Pendergast, E.M.V. Hoek, A review of water treatment membrane nanotechnologies, Energy & Environmental Science, 4 (2011) 1946-1971.
[16] M.A. Shannon, P.W. Bohn, M. Elimelech, J.G. Georgiadis, B.J. Mariñas, A.M. Mayes, Science and technology for water purification in the coming decades, Nature, 452 (2008) 301-310.
[17] C.H. Ahn, Y. Baek, C. Lee, S.O. Kim, S. Kim, S. Lee, S.H. Kim, S.S. Bae, J. Park, J. Yoon, Carbon nanotube-based membranes: Fabrication and application to desalination, Journal of Industrial and Engineering Chemistry, (2012).
[18] S. Kar, R. Bindal, P. Tewari, Carbon nanotube membranes for desalination and water purification: Challenges and opportunities, Nano Today, (2012).
[19] M. Majumder, P. Ajayan, Carbon nanotube membranes: a new frontier in membrane science, Comprehensive membrane science and engineering, 1 (2010) 291-310.
[20] S. Iijima, Helical microtubules of graphitic carbon, Nature, 354 (1991) 56-58.
[21] A.M. Popov, Y.E. Lozovik, S. Fiorito, L.H. Yahia, Biocompatibility and applications of carbon nanotubes in medical nanorobots, International Journal of Nanomedicine, 2 (2007) 361.
[22] J. Wang, Carbon nanotube based electrochemical biosensors: A review, Electroanalysis, 17 (2005) 7-14.
[23] M.S. Mauter, M. Elimelech, Environmental applications of carbon-based

nanomaterials, Environmental science & technology, 42 (2008) 5843-5859.
[24] T. Ebbesen, P. Ajayan, Large-scale synthesis of carbon nanotubes, Nature, 358 (1992) 220-222.
[25] T. Guo, P. Nikolaev, A.G. Rinzler, D. Tomanek, D.T. Colbert, R.E. Smalley, Self-assembly of tubular fullerenes, The Journal of Physical Chemistry, 99 (1995) 10694-10697.
[26] M. Jose Yacaman, M. Miki Yoshida, L. Rendon, J. Santiesteban, Catalytic growth of carbon microtubules with fullerene structure, Applied physics letters, 62 (1993) 202-204.
[27] A. Thess, R. Lee, P. Nikolaev, H. Dai, P. Petit, J. Robert, C. Xu, Y.H. Lee, S.G. Kim, A.G. Rinzler, Crystalline ropes of metallic carbon nanotubes, Science, 273 (1996) 483.
[28] en.wikipedia.org/wiki/File:CNTnames.png
[29] B. Corry, Designing carbon nanotube membranes for efficient water desalination, The Journal of Physical Chemistry B, 112 (2008) 1427-1434.
[30] G. Hummer, J.C. Rasaiah, J.P. Noworyta, Water conduction through the hydrophobic channel of a carbon nanotube, Nature, 414 (2001).
[31] J. Köfinger, G. Hummer, C. Dellago, Macroscopically ordered water in nanopores, Proceedings of the National Academy of Sciences, 105 (2008) 13218.
[32] T.A. Hilder, D. Gordon, S.H. Chung, Salt rejection and water transport through boron nitride nanotubes, Small, 5 (2009) 2183-2190.
[33] J.A. Thomas, A.J.H. McGaughey, Reassessing fast water transport through carbon nanotubes, Nano letters, 8 (2008) 2788-2793.
[34] J.K. Holt, Carbon nanotubes and nanofluidic transport, Advanced Materials, 21 (2009) 3542-3550.
[35] A. Striolo, The mechanism of water diffusion in narrow carbon nanotubes, Nano letters, 6 (2006) 633-639.

[36] A. Ismail, P.S. Goh, S. Sanip, M. Aziz, Transport and separation properties of carbon nanotube-mixed matrix membrane, Separation and Purification Technology, 70 (2009) 12-26.
[37] C. Lee, S. Baik, Vertically-aligned carbon nano-tube membrane filters with superhydrophobicity and superoleophilicity, Carbon, 48 (2010) 2192-2197.
[38] K. Sears, L. Dumée, J. Schütz, M. She, C. Huynh, S. Hawkins, M. Duke, S. Gray, Recent developments in carbon nanotube membranes for water purification and gas separation, Materials, 3 (2010) 127-149.
[39] B.J. Hinds, N. Chopra, T. Rantell, R. Andrews, V. Gavalas, L.G. Bachas, Aligned multiwalled carbon nanotube membranes, Science, 303 (2004) 62.
[40] J.K. Holt, H.G. Park, Y. Wang, M. Stadermann, A.B. Artyukhin, C.P. Grigoropoulos, A. Noy, O. Bakajin, Fast mass transport through sub-2-nanometer carbon nanotubes, Science, 312 (2006) 1034.
[41] A. Srivastava, O. Srivastava, S. Talapatra, R. Vajtai, P. Ajayan, Carbon nanotube filters, Nature materials, 3 (2004) 610-614.
[42] J.H. Choi, J. Jegal, W.N. Kim, Fabrication and characterization of multi-walled carbon nanotubes/polymer blend membranes, Journal of Membrane Science, 284 (2006) 406-415.
[43] M.F. De Volder, S.H. Tawfick, R.H. Baughman, A.J. Hart, Carbon nanotubes: present and future commercial applications, Science, 339 (2013) 535-539.
[44] A. Noy, H.G. Park, F. Fornasiero, J.K. Holt, C.P. Grigoropoulos, O. Bakajin, Nanofluidics in carbon nanotubes, Nano Today, 2 (2007) 22-29.
[45] G.K. Batchelor, An introduction to fluid dynamics, Cambridge university press, 2000.
[46] B.J. Hinds, N. Chopra, T. Rantell, R. Andrews, V. Gavalas, L.G. Bachas, Aligned multiwalled carbon nanotube membranes, Science, 303 (2004) 62-65.
[47] M. Majumder, N. Chopra, R. Andrews, B.J. Hinds, Nanoscale hydrodynamics:

Enhanced flow in carbon nanotubes, Nature, 438 (2005) 44-44.
[48] J.K. Holt, H.G. Park, Y. Wang, M. Stadermann, A.B. Artyukhin, C.P. Grigoropoulos, A. Noy, O. Bakajin, Fast mass transport through sub-2-nanometer carbon nanotubes, Science, 312 (2006) 1034-1037.
[49] B. Corry, Water and ion transport through functionalised carbon nanotubes: implications for desalination technology, Energy & Environmental Science, 4 (2011) 751-759.
[50] B.S. Gourary, F.J. Adrian, Wave functions for electron-excess color centers in alkali halide crystals, Solid State Physics, 10 (1960) 127-247.
[51] B.E. Conway, B. Conway, Ionic hydration in chemistry and biophysics, Elsevier Amsterdam, 1981.
[52] A.G. Volkov, Liquid-liquid interfaces: theory and methods, CRC PressI Llc, 1996.
[53] M. Majumder, N. Chopra, B.J. Hinds, Mass Transport through Carbon Nanotube Membranes in Three Different Regimes: Ionic Diffusion, Gas, and Liquid Flow, ACS nano, (2011).
[54] S. Qiu, L. Wu, X. Pan, L. Zhang, H. Chen, C. Gao, Preparation and properties of functionalized carbon nanotube/PSF blend ultrafiltration membranes, Journal of Membrane Science, 342 (2009) 165-172.
[55] T.V. Ratto, J.K. Holt, A.W. Szmodis, Membranes with embedded nanotubes for selective permeability, in, Google Patents, 2011.
[56] W. Sparreboom, A. Van Den Berg, J. Eijkel, Principles and applications of nanofluidic transport, Nature Nanotechnology, 4 (2009) 713-720.
[57] M. Whitby, N. Quirke, Fluid flow in carbon nanotubes and nanopipes, Nature Nanotechnology, 2 (2007) 87-94.
[58] S. Supple, N. Quirke, Rapid imbibition of fluids in carbon nanotubes, PhRvL, 90 (2003) 214501.

[59] F. Du, L. Qu, Z. Xia, L. Feng, L. Dai, Membranes of vertically aligned superlong carbon nanotubes, Langmuir, 27 (2011) 8437-8443.
[60] Y. Baek, C. Kim, D.K. Seo, T. Kim, J.S. Lee, Y.H. Kim, K.H. Ahn, S.S. Bae, S.C. Lee, J. Lim, High performance and antifouling vertically aligned carbon nanotube membrane for water purification, Journal of Membrane Science, 460 (2014) 171-177.
[61] S. Kang, M. Herzberg, D.F. Rodrigues, M. Elimelech, Antibacterial effects of carbon nanotubes: size does matter!, Langmuir, 24 (2008) 6409-6413.
[62] S.K. Manna, S. Sarkar, J. Barr, K. Wise, E.V. Barrera, O. Jejelowo, A.C. Rice-Ficht, G.T. Ramesh, Single-walled carbon nanotube induces oxidative stress and activates nuclear transcription factor-κB in human keratinocytes, Nano letters, 5 (2005) 1676-1684.
[63] S. Liu, L. Wei, L. Hao, N. Fang, M.W. Chang, R. Xu, Y. Yang, Y. Chen, Sharper and faster “nano darts” kill more bacteria: a study of antibacterial activity of individually dispersed pristine single-walled carbon nanotube, Acs Nano, 3 (2009) 3891-3902.
[64] S. Liu, A.K. Ng, R. Xu, J. Wei, C.M. Tan, Y. Yang, Y. Chen, Antibacterial action of dispersed single-walled carbon nanotubes on Escherichia coli and Bacillus subtilis investigated by atomic force microscopy, Nanoscale, 2 (2010) 2744-2750.
[65] P.J. Pomposiello, M.H. Bennik, B. Demple, Genome-Wide Transcriptional Profiling of theEscherichia coli Responses to Superoxide Stress and Sodium Salicylate, Journal of bacteriology, 183 (2001) 3890-3902.
[66] M. Zheng, X. Wang, L.J. Templeton, D.R. Smulski, R.A. LaRossa, G. Storz, DNA microarray-mediated transcriptional profiling of the Escherichia coli response to hydrogen peroxide, Journal of bacteriology, 183 (2001) 4562-4570.
[67] V. Kagan, Y. Tyurina, V. Tyurin, N. Konduru, A. Potapovich, A. Osipov, E.

Kisin, D. Schwegler-Berry, R. Mercer, V. Castranova, Direct and indirect effects of single walled carbon nanotubes on RAW 264.7 macrophages: role of iron, Toxicology letters, 165 (2006) 88-100.

[68] L. Guo, D.G. Morris, X. Liu, C. Vaslet, R.H. Hurt, A.B. Kane, Iron bioavailability and redox activity in diverse carbon nanotube samples, Chemistry of materials, 19 (2007) 3472-3478.

[69] D. Voet, J. Voet, C. Pratt, Fundamentals of biochemistry: life at the molecular level, Edició traduïda, (2006).

[70] S. Kang, M.S. Mauter, M. Elimelech, Microbial cytotoxicity of carbon-based nanomaterials: implications for river water and wastewater effluent, Environmental science & technology, 43 (2009) 2648-2653.

[71] W. Vollmer, D. Blanot, M.A. De Pedro, Peptidoglycan structure and architecture, FEMS microbiology reviews, 32 (2008) 149-167.

[72] C. Yang, J. Mamouni, Y. Tang, L. Yang, Antimicrobial activity of single-walled carbon nanotubes: length effect, Langmuir, 26 (2010) 16013-16019.

[73] K. Pulskamp, S. Diabaté, H.F. Krug, Carbon nanotubes show no sign of acute toxicity but induce intracellular reactive oxygen species in dependence on contaminants, Toxicology letters, 168 (2007) 58-74.

[74] S. Kang, M.S. Mauter, M. Elimelech, Physicochemical determinants of multiwalled carbon nanotube bacterial cytotoxicity, Environmental science & technology, 42 (2008) 7528-7534.

[75] S. Kang, M. Pinault, L.D. Pfefferle, M. Elimelech, Single-walled carbon nanotubes exhibit strong antimicrobial activity, Langmuir, 23 (2007) 8670-8673.

[76] C.D. Vecitis, K.R. Zodrow, S. Kang, M. Elimelech, Electronic-structure-dependent bacterial cytotoxicity of single-walled carbon nanotubes, Acs Nano, 4 (2010) 5471-5479.

[77] S. Patole, P. Alegaonkar, H.C. Lee, J.B. Yoo, Optimization of water assisted

chemical vapor deposition parameters for super growth of carbon nanotubes, Carbon, 46 (2008) 1987-1993.
[78] S. Patole, P. Alegaonkar, H.C. Shin, J.B. Yoo, Alignment and wall control of ultra long carbon nanotubes in water assisted chemical vapour deposition, Journal of Physics D: Applied Physics, 41 (2008) 155311.
[79] K. Hata, D.N. Futaba, K. Mizuno, T. Namai, M. Yumura, S. Iijima, Water-assisted highly efficient synthesis of impurity-free single-walled carbon nanotubes, Science, 306 (2004) 1362-1364.
[80] W. Zhang, B. Hallström, Membrane characterization using the contact angle technique I. methodology of the captive bubble technique, Desalination, 79 (1990) 1-12.
[81] Y. Baek, J. Kang, P. Theato, J. Yoon, Measuring hydrophilicity of RO membranes by contact angles via sessile drop and captive bubble method: A comparative study, Desalination, (2012).
[82] J. Burke, Solubility parameters: theory and application, (1984).
[83] A.F.M. Barton, CRC handbook of solubility parameters and other cohesion parameters, CRC, 1991.
[84] E. Li-Chan, S. Nakai, D. Wood, Hydrophobicity and solubility of meat proteins and their relationship to emulsifying properties, Journal of food science, 49 (1984) 345-350.
[85] S. Ito, M. Hashimoto, B. Wadgaonkar, N. Svizero, R.M. Carvalho, C. Yiu, F.A. Rueggeberg, S. Foulger, T. Saito, Y. Nishitani, Effects of resin hydrophilicity on water sorption and changes in modulus of elasticity, Biomaterials, 26 (2005) 6449-6459.
[86] R.H. Perry, D.W. Green, Perry's chemical engineers' handbook, McGraw-Hill New York, 2008.
[87] R.W. Baker, Membrane technology, Wiley Online Library, 2000.

[88] Y. Baek, J. Yu, S.H. Kim, S. Lee, J. Yoon, Effect of surface properties of reverse osmosis membranes on biofouling occurrence under filtration conditions, Journal of Membrane Science, 382 (2011) 91-99.
[89] S. Mun, Y. Baek, C. Kim, Y.W. Lee, J. Yoon, Feasibility of supercritical CO2 treatment for controlling biofouling in the reverse osmosis process, Biofouling, 28 (2012) 627-633.
[90] G. Hummer, J.C. Rasaiah, J.P. Noworyta, Water conduction through the hydrophobic channel of a carbon nanotube, Nature, 414 (2001) 188-190.
[91] Y. Zhu, S. Granick, Rate-dependent slip of Newtonian liquid at smooth surfaces, Physical review letters, 87 (2001) 96105.
[92] J.C.T. Eijkel, A. Berg, Nanofluidics: what is it and what can we expect from it?, Microfluidics and Nanofluidics, 1 (2005) 249-267.
[93] S. Joseph, N. Aluru, Why are carbon nanotubes fast transporters of water?, Nano letters, 8 (2008) 452-458.
[94] A. Kalra, S. Garde, G. Hummer, Osmotic water transport through carbon nanotube membranes, Proceedings of the National Academy of Sciences, 100 (2003) 10175-10180.
[95] T.A. Pascal, W.A. Goddard, Y. Jung, Entropy and the driving force for the filling of carbon nanotubes with water, Proceedings of the National Academy of Sciences, 108 (2011) 11794-11798.
[96] E. Celik, H. Park, H. Choi, Carbon nanotube blended polyethersulfone membranes for fouling control in water treatment, Water Research, 45 (2011) 274-282.
[97] G.S. Ajmani, D. Goodwin, K. Marsh, D.H. Fairbrother, K.J. Schwab, J.G. Jacangelo, H. Huang, Modification of low pressure membranes with carbon nanotube layers for fouling control, Water Research, (2012).
[98] G.F. Zhong, T. Iwasaki, H. Kawarada, Semi-quantitative study on the

fabrication of densely packed and vertically aligned single-walled carbon nanotubes, Carbon, 44 (2006) 2009-2014.
[99] K.S. Sing, Reporting physisorption data for gas/solid systems with special reference to the determination of surface area and porosity (Recommendations 1984), Pure Appl. Chem., 57 (1985) 603-619.
[100] M. Yu, H.H. Funke, J.L. Falconer, R.D. Noble, High density, vertically-aligned carbon nanotube membranes, Nano Lett., 9 (2008) 225-229.
[101] D.N. Futaba, K. Hata, T. Yamada, T. Hiraoka, Y. Hayamizu, Y. Kakudate, O. Tanaike, H. Hatori, M. Yumura, S. Iijima, Shape-engineerable and highly densely packed single-walled carbon nanotubes and their application as super-capacitor electrodes, Nat. Mater., 5 (2006) 987-994.
[102] E. Lauga, M. Brenner, H. Stone, Microfluidics: the no-slip boundary condition, Springer handbook of experimental fluid mechanics, (2007) 1219-1240.
[103] S. Mochizuki, A.L. Zydney, Dextran transport through asymmetric ultrafiltration membranes: comparison with hydrodynamic models, Journal of membrane science, 68 (1992) 21-41.
[104] R. Nobrega, H. De Balmann, P. Aimar, V. Sanchez, Transfer of dextran through ultrafiltration membranes: a study of rejection data analysed by gel permeation chromatography, Journal of membrane science, 45 (1989) 17-36.
[105] S.R. Wickramasinghe, S.E. Bower, Z. Chen, A. Mukherjee, S.M. Husson, Relating the pore size distribution of ultrafiltration membranes to dextran rejection, Journal of Membrane Science, 340 (2009) 1-8.
[106] J. Oliver, S. Anderson, J.L. Troy, B.M. Brenner, W. Deen, Determination of glomerular size-selectivity in the normal rat with Ficoll, Journal of the American Society of Nephrology, 3 (1992) 214-228.
[107] P. Aimar, M. Meireles, V. Sanchez, A contribution to the translation of retention curves into pore size distributions for sieving membranes, Journal of

membrane science, 54 (1990) 321-338.
[108] B.N. Nair, T. Yamaguchi, T. Okubo, H. Suematsu, K. Keizer, S.-I. Nakao, Sol-gel synthesis of molecular sieving silica membranes, Journal of membrane science, 135 (1997) 237-243.
[109] S. Singh, K. Khulbe, T. Matsuura, P. Ramamurthy, Membrane characterization by solute transport and atomic force microscopy, Journal of Membrane Science, 142 (1998) 111-127.
[110] A.J. Hart, A.H. Slocum, Rapid growth and flow-mediated nucleation of millimeter-scale aligned carbon nanotube structures from a thin-film catalyst, J. Phys. Chem. B, 110 (2006) 8250-8257.
[111] B.L. Wardle, D.S. Saito, E.J. García, A.J. Hart, R.G. de Villoria, E.A. Verploegen, Fabrication and Characterization of Ultrahigh-Volume-Fraction Aligned Carbon Nanotube–Polymer Composites, Adv. Mater., 20 (2008) 2707-2714.
[112] M. Jaroniec, R. Madey, Physical adsorption on heterogeneous solids, StPTC, 59 (1988).
[113] S. Gregg, K.S. Sing, Adsorption, Surface Area, and Porosity, (1983).
[114] C.N. Satterfield, Heterogeneous catalysis in practice, McGraw-Hill New York, 1980.
[115] Y. Liu, Q. Wang, T. Wu, L. Zhang, Fluid structure and transport properties of water inside carbon nanotubes, The Journal of chemical physics, 123 (2005) 234701.
[116] C.-M. Seah, S.-P. Chai, A.R. Mohamed, Synthesis of aligned carbon nanotubes, Carbon, 49 (2011) 4613-4635.
[117] S.P. Patole, H.-I. Kim, J.-H. Jung, A.S. Patole, H.-J. Kim, I.-T. Han, V. Bhoraskar, J.-B. Yoo, The synthesis of vertically-aligned carbon nanotubes on an aluminum foil laminated on stainless steel, Carbon, 49 (2011) 3522-3528.

[118] V. Shanov, Y.-H. Yun, M.J. Schulz, Synthesis and characterization of carbon nanotube materials, J. Chem. Technol. Metall., 41 (2006) 377-390.
[119] M.S. Dresselhaus, G. Dresselhaus, R. Saito, A. Jorio, Raman spectroscopy of carbon nanotubes, Phys. Rep., 409 (2005) 47-99.
[120] S. Krishnan, F.A. Armstrong, Order-of-magnitude enhancement of an enzymatic hydrogen-air fuel cell based on pyrenyl carbon nanostructures, Chemical Science, 3 (2012) 1015-1023.
[121] J.H. Walther, K. Ritos, E.R. Cruz-Chu, C.M. Megaridis, P. Koumoutsakos, Barriers to superfast water transport in carbon nanotube membranes, Nano Lett., 13 (2013) 1910-1914.
[122] P. Li, X. Lim, Y. Zhu, T. Yu, C.-K. Ong, Z. Shen, A.T.-S. Wee, C.-H. Sow, Tailoring wettability change on aligned and patterned carbon nanotube films for selective assembly, J. Phys. Chem. B, 111 (2007) 1672-1678.
[123] M. Herzberg, M. Elimelech, Biofouling of reverse osmosis membranes: role of biofilm-enhanced osmotic pressure, Journal of Membrane Science, 295 (2007) 11-20.
[124] H.-C. Flemming, Reverse osmosis membrane biofouling, Experimental thermal and fluid science, 14 (1997) 382-391.
[125] Y. Baek, J. Yu, S.-H. Kim, S. Lee, J. Yoon, Effect of surface properties of reverse osmosis membranes on biofouling occurrence under filtration conditions, J. Membr. Sci., 382 (2011) 91-99.
[126] E. Celik, H. Park, H. Choi, H. Choi, Carbon nanotube blended polyethersulfone membranes for fouling control in water treatment, Water research, 45 (2011) 274-282.
[127] G.S. Ajmani, D. Goodwin, K. Marsh, D.H. Fairbrother, K.J. Schwab, J.G. Jacangelo, H. Huang, Modification of low pressure membranes with carbon nanotube layers for fouling control, Water Res., 46 (2012) 5645-5654.

[128] H.J. Kim, Y. Baek, K. Choi, D.-G. Kim, H. Kang, Y.-S. Choi, J. Yoon, J.-C. Lee, The improvement of antibiofouling properties of a reverse osmosis membrane by oxidized CNTs, RSC Advances, 4 (2014) 32802-32810.
[129] W. Lee, C.H. Ahn, S. Hong, S. Kim, S. Lee, Y. Baek, J. Yoon, Evaluation of surface properties of reverse osmosis membranes on the initial biofouling stages under no filtration condition, Journal of Membrane Science, 351 (2010) 112-122.
[130] A. Tiraferri, C.D. Vecitis, M. Elimelech, Covalent binding of single-walled carbon nanotubes to polyamide membranes for antimicrobial surface properties, ACS applied materials & interfaces, 3 (2011) 2869-2877.
[131] J.L. Bahr, J.M. Tour, Covalent chemistry of single-wall carbon nanotubes, Journal of Materials Chemistry, 12 (2002) 1952-1958.
[132] C. Kong, M. Kanezashi, T. Yamomoto, T. Shintani, T. Tsuru, Controlled synthesis of high performance polyamide membrane with thin dense layer for water desalination, Journal of Membrane Science, 362 (2010) 76-80.
[133] A.K. Ghosh, B.-H. Jeong, X. Huang, E. Hoek, Impacts of reaction and curing conditions on polyamide composite reverse osmosis membrane properties, Journal of Membrane Science, 311 (2008) 34-45.
[134] F. Perreault, M.E. Tousley, M. Elimelech, Thin-Film Composite Polyamide Membranes Functionalized with Biocidal Graphene Oxide Nanosheets, Environmental Science & Technology Letters, 1 (2013) 71-76.
[135] H.A. Shawky, S.-R. Chae, S. Lin, M.R. Wiesner, Synthesis and characterization of a carbon nanotube/polymer nanocomposite membrane for water treatment, Desalination, 272 (2011) 46-50.
[136] T.H. Chong, F.S. Wong, A.G. Fane, The effect of imposed flux on biofouling in reverse osmosis: Role of concentration polarisation and biofilm enhanced osmotic pressure phenomena, Journal of Membrane Science, 325 (2008) 840-850.
[137] A.S. Brady-Estévez, S. Kang, M. Elimelech, A single-walled-carbon-

nanotube filter for removal of viral and bacterial pathogens, Small, 4 (2008) 481-484.
[138] Q. Li, M. Elimelech, Organic fouling and chemical cleaning of nanofiltration membranes: measurements and mechanisms, Environmental Science & Technology, 38 (2004) 4683-4693.
[139] E.-S. Kim, G. Hwang, M. Gamal El-Din, Y. Liu, Development of nanosilver and multi-walled carbon nanotubes thin-film nanocomposite membrane for enhanced water treatment, Journal of Membrane Science, 394 (2012) 37-48.
[140] Q. Li, Z. Xu, I. Pinnau, Fouling of reverse osmosis membranes by biopolymers in wastewater secondary effluent: Role of membrane surface properties and initial permeate flux, Journal of Membrane Science, 290 (2007) 173-181.
[141] K. Boussu, B. Van der Bruggen, A. Volodin, J. Snauwaert, C. Van Haesendonck, C. Vandecasteele, Roughness and hydrophobicity studies of nanofiltration membranes using different modes of AFM, Journal of colloid and interface science, 286 (2005) 632-638.
[142] J.-S. Choi, T.-M. Hwang, S. Lee, S. Hong, A systematic approach to determine the fouling index for a RO/NF membrane process, Desalination, 238 (2009) 117-127.
[143] S.-M. Park, J. Jung, S. Lee, Y. Baek, J. Yoon, D.K. Seo, Y.H. Kim, Fouling and rejection behavior of carbon nanotube membranes, Desalination, 343 (2014) 180-186.
[144] J. Wijmans, R. Baker, The solution-diffusion model: a review, Journal of membrane science, 107 (1995) 1-21.
[145] H.J. Kim, K. Choi, Y. Baek, D.-G. Kim, J. Shim, J. Yoon, J.-C. Lee, High-Performance Reverse Osmosis CNT/Polyamide Nanocomposite Membrane by Controlled Interfacial Interactions, ACS applied materials & interfaces, 6 (2014)

2819-2829.
[146] H.D. Lee, H.W. Kim, Y.H. Cho, H.B. Park, Experimental Evidence of Rapid Water Transport through Carbon Nanotubes Embedded in Polymeric Desalination Membranes, Small, (2014).
[147] J.M. Dickson, Fundamental aspects of reverse osmosis, Reverse osmosis technology, 35 (1988) 1-51.
[148] T. Matsuura, S. Sourirajan, Reverse osmosis transport through capillary pores under the influence of surface forces, Industrial & Engineering Chemistry Process Design and Development, 20 (1981) 273-282.
[149] J.N. Coleman, U. Khan, W.J. Blau, Y.K. Gun'ko, Small but strong: a review of the mechanical properties of carbon nanotube–polymer composites, Carbon, 44 (2006) 1624-1652.

요약(국문초록)

탄소나노튜브(Carbon nanotube; CNT) 막은 물 부족 문제를 해결해 줄 차세대 수처리 막으로 주목 받고 있다. 이러한 CNT 막은 CNT를 통한 빠른 물 분자의 흐름과 항균성을 이용하여 고성능 및 내오염성 막으로 개발할 수 있는 것으로 기대된다. 본 연구에서는 세 종류 (말단 개방형 수직배열 CNT 막, 밀집화 외벽이용 CNT 막과 혼합 CNT 막)의 CNT 막의 투수율, 제거 성능 및 바이오파울링 특성에 대해 평가하여 수처리 막으로서 CNT막의 특성을 연구하였다.

말단 개방형 수직배열 CNT 막을 상용 한외여과막(Ultrafiltration; UF)과 비교 평가하였다. 말단 개방형 수직배열 CNT 막은 상용 UF막보다 3배 정도 빠른 투수율 (~1,100 LMH/bar)을 보이면서 비슷한 제거 성능을 보였다. 이러한 빠른 흐름은 친수성 용매인 물에서만 특별히 보였으며, 소수성 용매의 흐름은 일반 유체와 같이 점도가 증가함에 따라 투수율이 감소하였다. 바이오파울링 측면에서는 말단 개방형 수직배열 CNT막이 상용 UF막에 비해 1/100 정도 적은 미생물이 부착되어 15% 정도 적은 투

수 감소율을 보이며 저감되었다는 것을 알 수 있었다.

밀집화 외벽이용 CNT 막도 상용 UF막과 비교하여 성능 및 미생물 부착 특성에 대하여 평가하였다. 기존 말단 개방형 수직배열 CNT 막이 수천 LMH/bar의 투수율을 보인 것에 비해, 밀집화 외벽이용 CNT 막은 밀집화를 통한 공극밀도를 10배 정도 향상시키고 CNT 내/외벽을 모두 공극으로 이용함으로써 약 30,000 LMH/bar의 훨씬 빠른 투수율을 보였다. 제거 성능 측면에서는 CNT 내부직경 (5 nm)과 외벽으로 구성된 공극직경 (7 nm)으로 상용 UF 막에 비하여 조금 낮은 수준이었다. 또한 밀집화 외벽이용 CNT 막 표면의 나노 패턴화 되어있어 미생물 부착을 현저히 저감시키고 나아가 생물막 형성도 저해하는 것을 관찰하였다.

마지막으로 두 종류의 혼합 CNT 막을 역삼투막과 비교하여 평가하였다. 폴리아마이드 (Polyamide; PA) 층위에 기능기가 부착된 CNT를 증착시키고 폴리비닐알코올 (PVA)로 코팅한 PA-CNT-PVA 막을 제조하였다. 이 막은 PA 막과 비슷한 투수율 및 염 제거율을 보이지만, 보다 강한 기계적 강도를 보이며 뛰어난 바이오파울링 저감 효과를 보였다. 그리고 계면중합법을 이용한 PA 합성 시, 기능기가 부착된 CNT를 혼합하여 만든 복합 CNT 역삼투막은 PA

역삼투막에 비해 약 30% 빠른 투수율과 비슷한 염 제거율을 보였다. 이러한 빠른 투수율은 다양한 압력과 원수 농도 조건에서도 유지되며 PA 막에 비해 동일한 물을 생산한다고 가정하였을 때 보다 적은 에너지가 소모되었다. 막 오염 측면에서 복합 CNT 역삼투막은 표면에 CNT의 부재로 인해 바이오파울링에는 큰 영향을 보이지는 않았지만, 보다 낮은 표면 거칠기로 인해 35,000 mg/L 인공해수 실험에서는 PA 막에 비해 적은 유량감소와 세척 시 보다 효율적인 유량 회복 현상을 보였다. 본 연구 결과들을 종합해보면 고성능 및 내오염성을 지닌 CNT 막이 실제 수처리 막 공정에 적용 가능하다는 것을 보여준다.

주요어: 탄소나노튜브 막; 투수율; 제거 성능; 바이오파울링; 수처리

학 번: 2009-20996